Mechanochemical pattern formation in the cellular actomyosin cortex

by

Melis Tekant

B.S., Stanford University (2014)

Submitted to the Department of Physics
in partial fulfillment of the requirements for the degree of

Doctor of Philosophy in Physics

at the

MASSACHUSETTS INSTITUTE OF TECHNOLOGY

June 2021

Author . . . .
Department of Physics
May 7, 2021

Certified by . . . .
Nikta Fakhri
Thomas D. and Virgina W. Cabot Career Development Associate
Professor of Physics
Thesis Supervisor

Accepted by . . . .
Deepto Chakraborty
Associate Department Head, Physics

Mechanochemical pattern formation in the cellular actomyosin cortex

by

Melis Tekant

Submitted to the Department of Physics
on May 7, 2021, in partial fulfillment of the
requirements for the degree of
Doctor of Philosophy in Physics

Abstract

Protein patterning is essential for cellular function. From cell division to cell migration, specific positional and temporal arrangement of proteins are requisite to triggering and executing vital cell processes. In the aforementioned examples and many other fundamental cellular activities, biochemical patterns drive or are accompanied by dramatic shape transformations. As mechanical conditions, such as cortical stress and membrane curvature, change in response to spatially arranged and temporally varying forces, the biochemical patterns, too, must evolve with this dynamic environment to enact complex cell movements. While the intricate interplay between protein patterning and cell deformations is important to any cellular function, it is especially paramount to carrying out processes that require large transformations of cell geometry. Yet, how cells rapidly and reliably communicate information between their chemical and mechanical fields is still not fully understood.

In this thesis, I explore the mechanisms of coupling between cell mechanics and biochemical patterns in the actomyosin cortex of *Patiria miniata* sea star oocytes. This is an ideal biological model system for exploring the interactions between biochemical patterning and mechanical deformations in evolving mechanochemical systems *in vivo* due to their experimental accessibility and wealth of attainable biochemical patterns. In Chapter 2, I utilize endogenous fluorescent markers embedded in the actomyosin mesh to probe the spatiotemporal surface strain patterns induced by the activity of Rho proteins, a highly conserved regulator of cell contractility, on the oocyte membrane. In Chapter 3, I show how these Rho patterns can be tuned *in vivo* using dynamic, external geometrical deformations by combining micropipette aspiration with live fluorescence imaging. In Chapter 4, I describe the infrared spectroscopy setup built in the pursuit of uncovering the properties of fluorescent markers. Taken together, the work in this thesis outlines a quantitative approach towards uncovering the coupling between contractility regulating biochemical patterns and cellular deformations in dynamically evolving geometries.

Thesis Supervisor: Nikta Fakhri
Title: Thomas D. and Virgina W. Cabot Career Development Associate Professor of Physics

Acknowledgements

So long, and thanks for all the (star)fish.

This thesis would not have been possible without the help of countless incredibly kind and talented people whom I have been lucky to have met. Firstly I'd like to thank my advisor Nikta Fakhri for her guidance and support throughout my PhD, as well as my thesis committee members Jörn Dunkel, Jeff Gore, Mehran Kardar, and Leonid Levitov for their insightful comments.

In the Fakhri Lab, I have been fortunate enough to work side-by-side and collaborate with wonderful scientists and friends. Thank you to Sebastian Coupe and Jinghui Liu for making room alpha (renamed to epsilon) such a fun office to be in. Sebastian, thank you for answering all my questions on anything biology related and the countless hours we have spent around the optical table, taking data. Jinghui, it was so much fun rooming with you at every conference. Tzer Han Tan has helped me tremendously in getting started in the lab, Alex Bacanu has been instrumental for the mechanochemical coupling project, and I cannot thank Yoon Jung enough for so freely volunteering his boundless knowledge in so many different areas, from his help in building the spectroscopy setup to teaching me about wavelets. To everyone mentioned here and other members of the Fakhri Lab whom I did not get a chance to work with, thank you for your friendships, lunch discussions, and birthday cakes.

The Physics of Living Systems at MIT is a highly collaborative environment and I have had the great fortune of working with brilliant colleagues. Peter Foster has not only taught me everything I know about micropipette aspiration, but brainstormed ideas, troubleshot issues, and collaborated in some crazy experiments with me. He is remarkably generous with his time, and I cannot thank him enough for his contributions to my work at MIT. Though I did not get the opportunity to work directly, Shreyas Gokhale has also been an incredible friend and mentor. His classical Indian music was instrumental (pun intended) in helping me shake off the pandemic stress. Thanks also to Iain Cheeseman and Zak Swartz for being such great mentors, collaborators, and teaching me everything I know about sea stars. Zak, without your help, I would have never been able to perform *any* of the experiments in this thesis.

Thank you to Cathy Modica, Sydney Miller, Monica Wolf, and Karen Sagna for your kindness, generosity, and willingness to help. The department would crumble in a day without you. Thanks also to the Graduate Women in Physics for the seminars, dinners, and overall camaraderie, as well as our mentor Anna Frebel, whose insights and advice have been pivotal to my time at MIT, for always making time for me in her unbelievably busy life.

Outside of work, friends have made PhD life much easier through great times and delicious food. A huge thank you to Jeremy Owen, Julia Steinberg, Dahlia Klein, Anne Hebert, Julian Leonard, Ian Tenney, Hart Goldman, Anton Mazurenko (and Chloe), Daniel Greif, Renate Landig, Adam Kaufman, Annalise Everett (and Maddie), Ahmed Omran, Johan Bonilla, Devi Lockwood and the Gould House. From board games to potlucks, from Zoom parties to picnics at the park, it has been an absolute joy to spend time with you and your furry friends. (A special thank you to those who have stayed in touch despite living halfway across the world!)

Of course, none of this would have been possible without the support of my fantastic family. *Anne, baba, Deniz, Nermin abla, başarılarımı benimle kutladınız, sıkıntılarımı hep dinlediniz. Tüm kararlarıma destek oldunuz. Anne, baba, bana en iyi eğitimi vermek için her şeyi yaptınız. Üzerimdeki emeğinizi yazıya dökebilmem mümkün değil. Her şey için çok teşekkürler; hepinizi çok seviyorum.*

I have also been fortunate to have gained a second family during my time at MIT. Val, Frank, Jeanine, and Stephen: thank you so much for welcoming me into your family. You have been so kind and supportive. I feel incredibly lucky to be a part of the Rispoli family.

Finally, the biggest thank you to Matthew, who has been the best partner I could have ever asked for. I am blown away by your selflessness, empathy, and brilliance everyday. Thank you for always being there for me, and for being a great dad to our furry baby Pepper. I can't wait to resume traveling the world with you. *Seni çok seviyorum.*

Contents

List of Figures

List of Tables

Chapter 1

Introduction: Mechanochemical coupling in biological systems

"Omne vivum ex ovo"

— William Harvey

Throughout embryogenesis, an organism starts out as a single spherical cell, and through intricately controlled, and remarkably coordinated events, develops into a geometrically complex biological system. Spatial patterning of biochemicals is crucial for initiating and guiding many vital cellular processes which enable this dramatic transformation [30, 44, 62]. As the embryo develops, cells and tissues are bent and stretched, necessitating the evolution of cellular protein patterns to reflect the changing geometry of the organism. This dynamic interplay between chemistry and shape suggests that biochemical patterning and geometrical deformations are intimately linked [1, 68].

Indeed, in his widely celebrated and influential paper *The Chemical Basis of Morphogenesis*, written in 1952, Alan Turing proposed that reaction-diffusion systems could create chemical patterns in developing organisms, and that the *"stresses as given by elasticities and motions"* could also play a role in such patterning and thus should be taken into account. He remarked that *"the interdependence of the chemical and mechanical data [added] enormously to the difficulty,"* compelling him to consider cases where mechanics and chemical patterning could be separated [64]. Nearly seventy years after his remarks, though the mechanisms underlying this coordination continue to be the focus of active research, they are still not fully understood.

So far, most research exploring mechanochemical coupling in biological systems has focused primarily on identifying the genes and signaling molecules that are associated with the various developmental processes of organisms [24, 10]. For example, *twist* and *snail* genes in the *Drosophila melanogaster* fruit fly embryo have been shown to be necessary for the complete and correct mesoderm invagination by initiating and directing collective cell deformation [41]. As for proteins, those associated with the Wnt pathway were found to be responsible for body axis determination and cell fate decisions in fruit fly embryos as well as those of mice [4, 43]. Various other genes and proteins have been implicated in the timely and successful completion of morphological events throughout the development of embryos in model systems [59].

However, only a small number of signaling pathway families are found to be central to cellular and embryonic development throughout the animal kingdom [35]. In many cases, a single pathway is responsible for the emergence of multiple distinct morphological structures across many species. For example, the hedgehog signaling pathway enables the establishment of anteroposterior polarity in invertebrates [34], the determination of digit identity in mammalians [63], and the development of the Cnidarian gut [45]. Therefore, the phenotypic output resulting from the activity of a certain signaling pathway must be entirely context dependent: where the cell is located in space and time and what the external cues acting on it are.

The local chemical environment undoubtedly plays a role in cell behavior. Morphogen concentration gradients have been shown to provide positional information to cells, eliciting spatially patterned, dose dependent cellular responses, such as polarity [25], transcription [23], and cell fate [22]. For example, in *Drosophila* larvae, the chemical gradient of the morphogen Decapentaplegic, expressed as a stripe, sets up the inverse gradient of the transcription factor Brinker, repressing gene expression and leading to the patterning of the wing veins [47].

Mechanical cues acting on the cell must also be considered as input in influencing the resulting individual or collective cellular behavior. For instance, shapes of individual or a collection of cells can dictate the range of responses of the biological system by determining the distribution of morphogenetic gradients [48]. Furthermore, cell generated forces and mechanical stresses induced by their environment may alter biochemical processes, leading to disparate behavioral outcomes. Such an affect has been observed in human mesenchymal stem cells, where stress gradients and substrate stiffness have been shown to influence stem cell lineage specification [19, 55].

The effect of the mechanical structure of the biological system on biochemical pattern formation has also been experimentally observed on the subcellular level. MinD and MinE pole-to-pole oscillations aid in locating the cell division site in rod shaped *Escherichia coli* bacteria [52, 46]. A rich set of patterns including oscillatory, standing, and traveling Min-protein waves have been observed in cells of varying sizes [66]. Furthermore, in growing cells, Min patterns were found to transition from one wave type to another [9]. Like in the case of Min oscillations, many morphogenetic chemical patterns arise at timescales comparable to those in which cells extend, bend, and divide. Thus, it is imperative to think of the cell as a dynamic system both when considering biochemical patterning and also when taking mechanical cell deformations into account. Yet, a complete quantitative understanding of the mechanisms with which protein patterns robustly affect cell mechanics, and the effect of dynamic geometrical constraints, forces, and stresses on such patterns is lacking.

1.1 Rho GTPases: master regulators of cell contractility

A family of biochemicals widely implicated in essential processes related to the survival of single cells as well as the development of embryos is the Rho family of guanosine triphosphatases (GTPases). A subfamily of the Ras superfamily of small GTPase

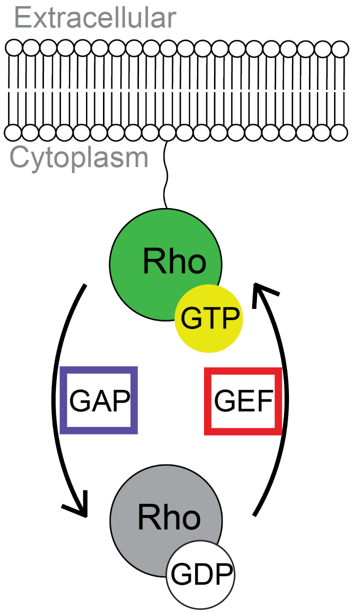

Figure 1-1: A simplified schematic representation of the Rho GTPase reaction network. Guanine nucleotide exchange factor (GEF) binds to inactive Rho (Rho-GDP) and converts it to its active form (Rho-GTP). GTPase-activating protein (GAP) reverses this process, binding to Rho-GTP and transforming it to Rho-GDP. Only Rho-GTP interacts with its downstream effectors, leading to the regulation of actin filamentous protein and myosin force generating molecular motor dynamics.

proteins, Rho proteins are highly conserved, and members of it are found across all eukaryotic cells. Often referred to as master regulators of cell contractility, Rho GTPases play a key role across a wide range of cellular processes that necessitate dramatic geometrical deformations, such as cell division, motility, adhesion, and polarization. They actuate such complex cellular activities by spatially and temporally patterning and regulating actomyosin dynamics [36, 50].

Rho GTPases are lipid-modified enzymes whose activity can be modulated through guanosine triphosphate (GTP) hydrolysis, acting as a binary molecular switch. When bound to GTP, Rho is in its active state, and is associated with the cellular plasma membrane, communicating with its downstream effectors in the actomyosin cortex. This interaction results in alterations in actin filamentous protein dynamics as well as myosin molecular motor activity. Guanosine diphosphate (GDP) bound Rho, on the other hand, is inactive. Transitions from one state to another are enabled by regulatory proteins such as guanine nucleotide exchange factors (GEFs) and GTPase-activating proteins (GAPs). Rho-GEFs exchange GDP for GTP, activating the GTPase, and Rho-GAPs act as inactivators by catalyzing the hydrolase activity of Rho. Lastly, guanosine nucleotide dissociation inhibitors (GDIs) bind to Rho-GDPs and maintain their inactive state, as well as protect them from proteolysis. These regulatory proteins act in concert to control local Rho activity, and have been shown to create spatiotemporal patterns of Rho even at the sub-cellular level, leading to dramatic and robust cell shape deformations [3].

Cell division is one of the most vital cellular functions, requiring a high level of temporal precision and spatial accuracy of biochemical patterns and mechanical deformations. Rho GTPases lie at the heart of this process [36]. Throughout cytokinesis, Rho activity localizes to a narrow zone at the equator of the cell, resulting in the formation of a contractile actomyosin ring. As the cell constricts, Rho activity and the cytokinetic machinery stay localized at the site until the two daughter cells are successfully separated. Intricate coordination between chemical patterning and cell deformations is paramount to reliably achieving the desired outcome of two detached daughter cells with equal cytoplasmic and genetic material.

While molecular players of cellular stress generation are established, the mechanism with which Rho GTPases regulate the mechanical properties of the actomyosin cortex and actuate large scale shape changes is unknown. Furthermore, the understanding of how spatio-temporal patterns of Rho GTPases are formed and evolve under dynamic geometrical deformations is still lacking. Since Rho GTPases are highly conserved across the metazoa and are involved in many events related to actomyosin contractility and cell shape change [36], studying these small GTPase proteins will not only help explain the dynamics behind the specific system, but will also shed light on the general principles of coupling between biochemical patterning and mechanical deformations in biological systems.

In this thesis, I focus on RhoA, a member of Rho GTPases conserved across the animal kingdom, a protein crucial for successful meiotic division of oocytes as well as embryonic cytokinesis in many organisms. The inactivation of RhoA in animal model systems including *Xenopus* frog [18], *Drosophila melanogaster* fruit fly [17],

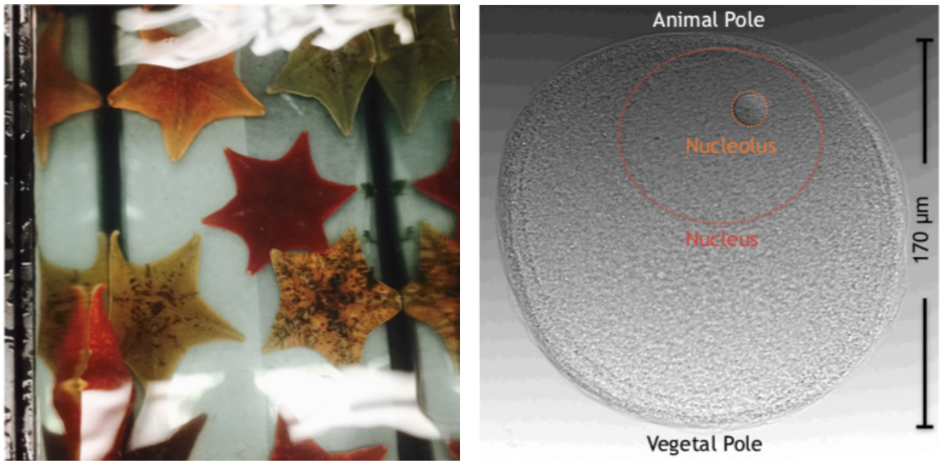

Figure 1-2: Wild isolates of *Patiria miniata* sea stars (left) and a *Patiria miniata* oocyte (right).The nuclei of these oocytes are off centered, creating the animal-vegetal pole axis. Upon maturation, the contraction waves preceding meiotic divisions travel along this axis.

and *Danio rerio* zebrafish embryos [40] result in an inability to perform successful cytokinesis. In these species as well as mammalian cultured cells, GEF epithelial cell transforming sequence 2 (Ect2) acts upstream of RhoA, as its primary activity regulator, during cell division [16].

In large oocytes, such as those of *Xenopus* [29], sea urchin [39], and sea stars [28], another widely observed large scale shape deformation event is the surface contraction wave. Coupled to cell cycle transitions, these waves are hypothesized to aid in successful chromosomal alignment during asymmetric meiotic divisions, but their exact role is still debated [28, 51]. In the oocytes of the sea star *Patiria miniata*, surface contraction waves manifest as a contractile actomyosin band traveling from one pole of the oocyte to the other during meiotic anaphase. This process is carried out by a cascade of protein patterns, starting out with the time-dependent cytosolic gradient of Cdk1-cyclinB, a cell cycle regulator [7, 67]. This gradient acts to localize a moving threshold, which guides the Ect2 front, separating regions of high and low Ect2 concentration. Downstream of this process, a band of active RhoA localizes to the Ect2 front on the membrane, activating an actomyosin contractile ring. As the Cdk1-cyclinB gradient evolves, the band of high RhoA activity, and thus the contrac-

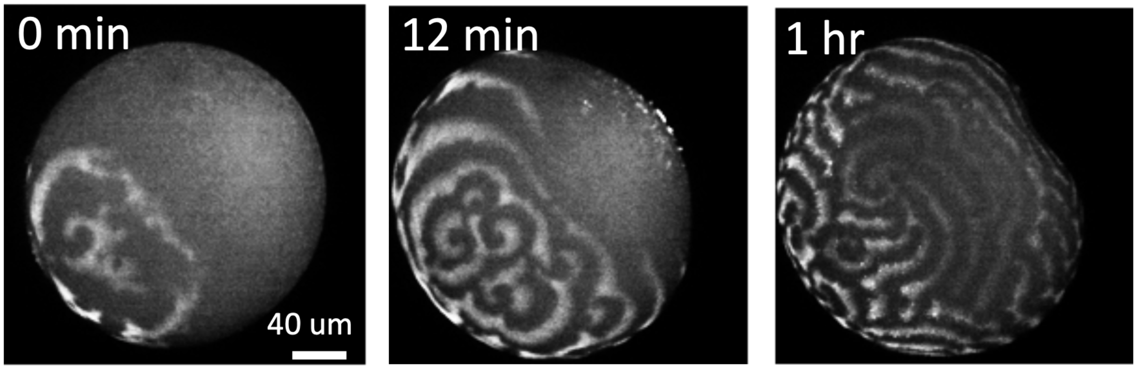

Figure 1-3: Time lapse of fluorescently labeled Rho-GTP patterns on the surface of a *Patiria miniata* oocyte after maturation. After the propagating spiral wave front ends at the animal pole of the oocyte, the spiral patterns persist on the oocyte membrane for multiple hours.

tion ring, sweeps the oocyte, starting at the vegetal pole, and ending at the animal pole. The conclusion of this process coincides with a meiotic division, and a polar body ejection.

In the *Patiria miniata* oocytes with Ect2 overexpression, however, a propagating front of Rho-GTP spiral waves is observed [5]. These spatio-temporally evolving spirals are created by reaction-diffusion dynamics of bistable Ect2 activity, and remain visible on the oocyte surface for multiple hours (Figure 1-3). Instead of a traveling contractile ring, these patterns create dynamically evolving surface fluctuations that arise from active cortical stress.

In this thesis, I highlight two distinct methods for uncovering the nature of mechanochemical coupling between Rho GTPase signaling molecules and cellular mechanics using sea star oocytes as a model system. The oocytes of the sea star *Patiria miniata* are ideal systems for studying mechanochemical coupling *in vivo* on the cellular level due to their experimental accessibility: the oocytes are transparent, allowing for live cell fluorescence imaging, possess a thick and well defined actomyosin layer, and exhibit rich and tunable spatio-temporal biochemical patterning.

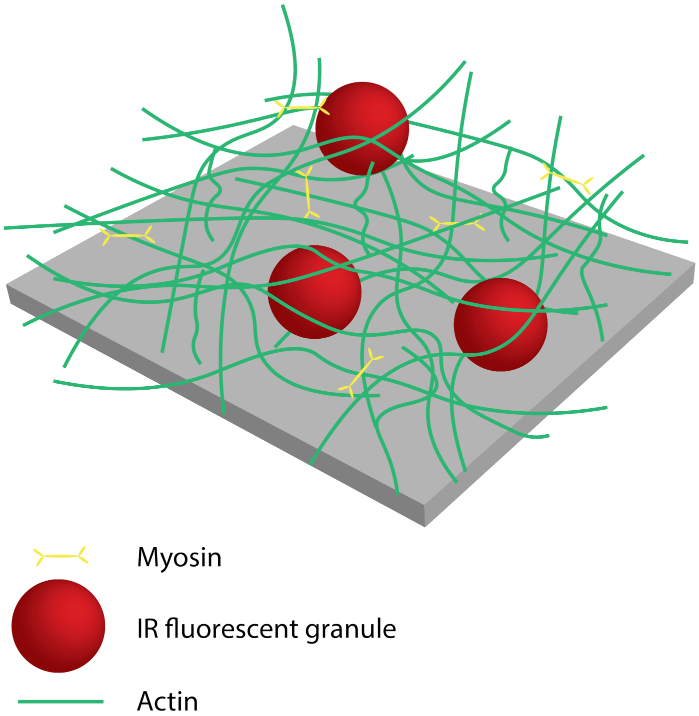

Figure 1-4: A simplified schematic drawing of the cellular actomyosin cortex. Lying directly inside (represented as above in the drawing) the cell membrane, this layer gives the cell its shape and is responsible for large scale cellular shape deformations. The actin filamentous proteins make up the scaffold of the cortex, while myosin molecular motors generate forces. In *Patiria miniata* oocytes, the cortex also contains infrared fluorescent granules embedded in the actin mesh.

1.2 Uncovering the mechanical deformations created by chemical patterns using passive probes

Ect2 overexpressed *Patiria miniata* oocytes exhibit spatiotemporal Rho-GTP spiral waves on their surfaces [5], creating dynamic stress patterns on their actomyosin cortices. Though active Rho can be easily visualized through time lapse imaging of its fluorescent reporter, the mechanical deformations are more difficult to observe without the injection of exogenous probes that may alter cellular dynamics. This problem is avoided in sea star oocytes, which contain endogenous, fluorescent granules embedded in their cell cortices. As the cortical layer experiences forces and deforms under the effect of myosin activity due to RhoA patterning, the granules entangled in the actin mesh move with it, making them ideal point particles for visualizing

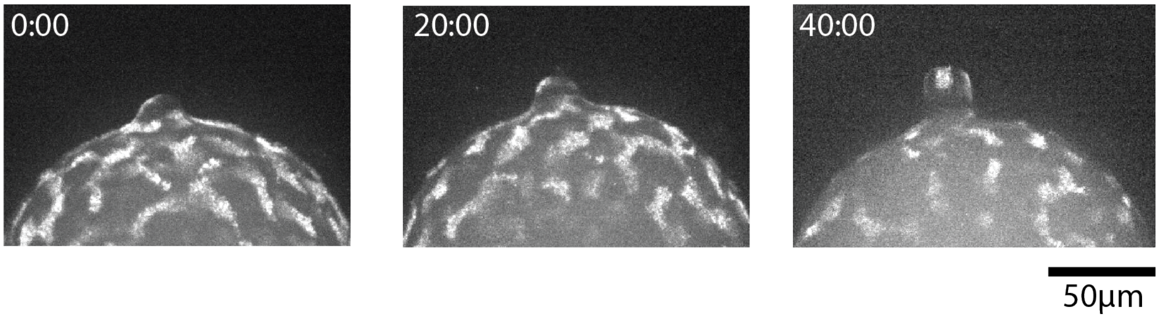

Figure 1-5: Fluorescence images of spiral RhoA patterns on a partially aspirated *Patiria miniata* oocyte membrane. Time stamps are presented in mm:ss format.

the movement of the cell cortex. By identifying and tracking the motion of these granules using fluorescence microscopy, the deformations of the actomyosin layer can be captured. Our studies into the nature and spectral properties of these granules is described in Chapter 4.

In Chapter 2, I show how simultaneous fluorescence time lapse imaging of spiral patterns of Rho-GTP concentration and cortex embedded granules reveal the coupling between the chemical and mechanical fields in this system. From the motion of the granules, strain rate maps of the cortex are constructed, and are found to exhibit the same temporal periodicity as the RhoA patterns. Furthermore, strong anti-correlation between RhoA concentration and local area change is established, and alignment of principal strain-rate components with RhoA pattern shapes is observed.

1.3 Tuning biochemical patterns through active geometrical perturbations

In Chapter 3, I explore how RhoA patterns evolve in response to active deformations and adapt to evolving geometries, such as in the case of cell division. Through the use of micropipette aspiration, dramatic yet highly controlled geometrical deformations are induced on *Patiria miniata* oocytes expressing spiral RhoA patterns. This versatile tool allows for a wide range of geometries to be accessible, as well as variation in the speed of deformation. By combining live fluorescence confocal imaging of RhoA patterns with micropipette aspiration, the evolution of biochemical patterns inside the micropipette are imaged in real time (Figure 1-5). The patterns are found to display time and location dependent dynamics along the micropipette, indicating that they can be tuned through such deformations.

1.4 Identification of the spectral properties of fluorophores via infrared fluorescence spectroscopy

Though a plethora of fluorescent proteins and other fluorophores are at the disposal of scientists, they suffer from undesirable properties such as low photostability, high non-specific binding rate, and shallow substrate penetration depth. Thus, the discovery of new fluorescent markers with more desirable properties is still an active field or research. Identifying the physical and spectral properties of these substances is central to their discovery and development. To this end, in Chapter 4, I describe the infrared spectroscopy setup we have built in the Fakhri Lab for the identification and characterization of such novel fluorophores and their photoproperties.

Chapter 2

Quantifying mechanochemical coupling in the actomyosin cortex *in vivo*

> *"There are only patterns, patterns on top of patterns, patterns that affect other patterns. Patterns hidden by patterns. Patterns within patterns. "*
>
> — Chuck Palahniuk

2.1 Abstract

Biochemical reaction-diffusion patterns, coupled with downstream cellular effects such as cytoskeletal activity, actuate many dynamic and complex cellular processes. Though observed across a wide range of length and timescales, a quantitative analysis of the interplay between biochemical signaling and cellular force generation has not been fully explored. In this work, using the oocytes of the sea star *Patiria miniata*, we aim to quantify the coupling between the spatio-temporal patterns of the biochemical RhoA and the mechanical deformations of the actomyosin cortex of the cell. By simultaneously tracking endogenous tracer particles embedded in the cell cortex and imaging a fluorescent RhoA-GTP reporter, the local dynamics of the cell cortex

can be visualized in real time alongside the biochemical patterns. The actomyosin cortex is found to exhibit strain-rate patterns closely resembling those of RhoA activity, with maximal strain strongly aligned with the pattern shapes. Extending this analysis to include the full viscoelastic nature of the cell cortex, the mutually coupled constitutive relationship between biochemical activity on the cell membrane and the patterned active forces driven by RhoA can be uncovered.

2.2 Introduction

2.2.1 RhoA: A contractility regulating biochemical vital for cellular function

The Rho family of proteins drives a plethora of crucial cellular processes such as cell division and migration by directing the organization of the cytoskeleton and regulating the spatial patterning of myosin motor proteins [36]. Highly conserved across the animal kingdom, this family of biochemicals is found in a wide range of species as an essential regulator of cellular and sub-cellular level force generation. For instance, during cell division, Rho localizes to the mid-plane of the cell, orchestrating the formation of the cytokinetic ring [50].

Rho actuates and precisely carries out such dramatic cellular shape changes through its communication with the biochemical's downstream affectors that generate local forces on the cellular cytoskeleton. By switching between Rho's active (phosphorylated) and inactive (dephosphorylated) states through the interactions with the protein's the upstream regulators GEF and GAP (Figure 1-1), Rho can form spatially and temporally varying domains of activity on the cell surface. Such dynamic contractility driving activity can create significant deformations to the cell geometry, leading to local strain patterns. In turn, these deformations could affect the Rho patterning that created them, forming a feedback loop. One way such mechanochemical coupling could manifest on a cellular level is through the contractile nature of the cortex. A patch of active RhoA on the cell cortex will lead to a contraction in that

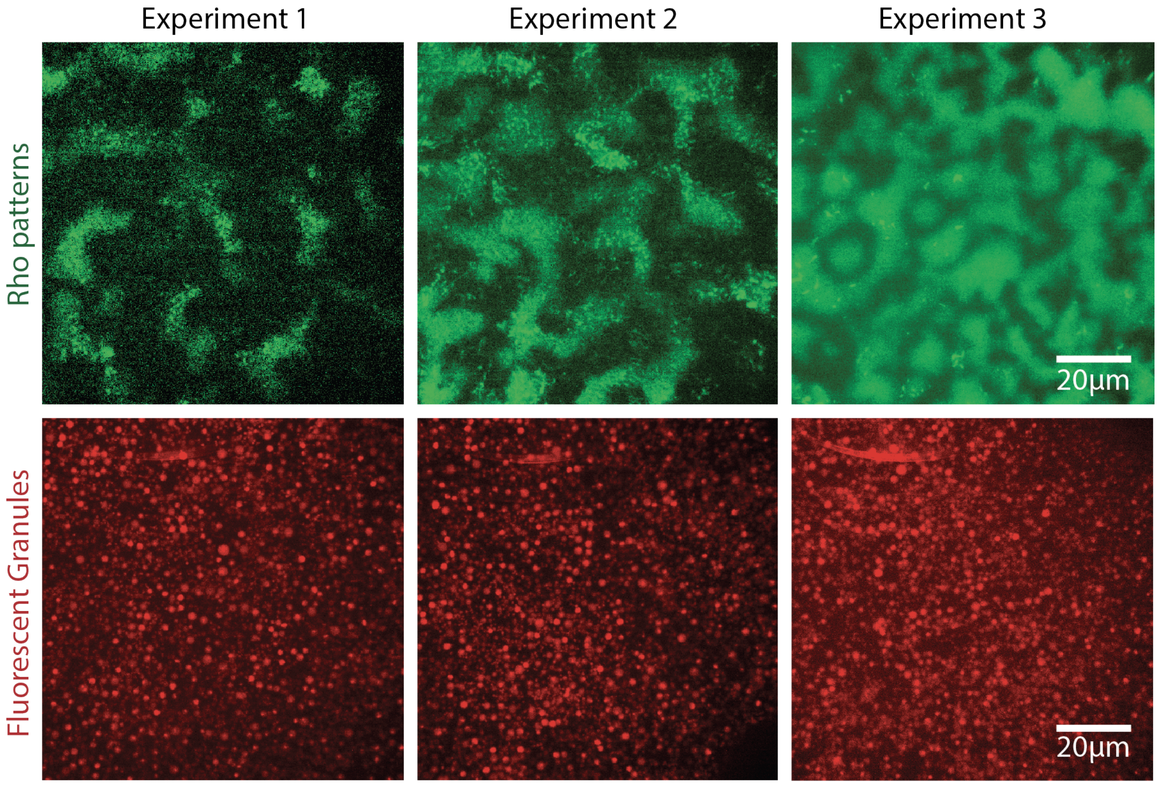

Figure 2-1: Confocal fluorescence microscopy images of Rho activity patterns (top row) and their corresponding granule fields (bottom row). The experiments are obtained from different oocytes, with each cell displaying a unique Rho activity pattern, depending on its specific activity level.

region, which will enhance the local density of RhoA, which, in turn, will lead to a stronger local contraction, and so on. While such biochemical feedback mechanisms have been proposed, their details remain unclear and many aspects have not been experimentally confirmed.

Through its interactions with force generating biochemicals such as RhoA, the actomyosin cortex gives the cell its dynamic shape. Operating far out of thermal equilibrium, the internal activity of the cellular cytoskeleton gives rise to unusual material properties such as active stresses and spontaneous flows[12]. The cortex can be thought of as a two-dimensional gel-like network of filaments, crossed linked by specialized passive and active linkers that couple the filaments and generate forces. This property gives rise to elastic behavior in short timescales. Continuous remodeling of the cortex relaxes the stresses over time and the strain energy gets dissipated.

This behavior results in viscous flow in long timescales[8]. Using a viscoelastic model, it is possible to reveal not only the properties of the cortex but also how the spatiotemporally patterned biochemicals manifest as forces in the mechanical field.

In this project, we aim to quantify and uncover the nature of mechanochemical coupling between the signaling molecule RhoA and the actomyosin cortex of a single cell. The oocyte of the starfish *Patiria miniata* is the ideal model system for the study of mechanochemical patterns *in vivo* due to their experimental accessibility: they exhibit a range of biochemical patterns upon maturation (which can be induced via a known hormone), possess well defined actomyosin cortices, and are optically transparent, making *in vivo* fluorescence imaging possible. When the biochemical Ect2, responsible for the activation of RhoA, is overexpressed, these oocytes display dynamically evolving spiral RhoA waves which can be observed through fluorescent labeling of the active form of RhoA, as shown in Figure 2-1.

2.2.2 Endogenous infrared fluorescent granules as passive point probes for cortical deformations

Phosphorylated (active) RhoA acts as a local recruiter for the molecular motor myosin II [49], and also interacts with actin, where RhoA locally promotes polymerization of actin, and in turn, polymerized actin may promote dephosphorization (inactivation) of RhoA [5]. Through this interaction, dynamically evolving spirals manifest as spatiotemporally patterned forces and stresses on the cell cortex. The response of the mechanical field can be observed by tracking endogenous, fluorescent granules embedded in the *Patiria miniata* oocyte cortex.

These fluorescent granules can be excited with visible wavelength lasers in the blue to green wavelength range, and have emission peaks in the infrared. They can be observed with high spatial and temporal resolution owing to their remarkable photostability. With typical sizes of around 1-3 μm, they are embedded in the cellular cytoskeletal mesh (Figure 2-1). Their motion is a result of the local stresses on the cortex, as well as the continuous remodeling of the cytoskeletal network.

Typical techniques for studying the deformation of the cellular cortex, for instance in the case of atomic force microscopy (AFM), magnetic twisting, and optical tweezers, rely on applying extrinsic forces to the cell. Such methods are designed to create precise and known external forces on the cells to assess the nature of the cortical response. However, passive probes are also used to probe cytoskeletal modulation. Such techniques include the use of single walled carbon nanotubes (SCWNTs) [61], nanobody-functionalized quantum dots which can be fabricated to target cytoskeletal components such as actin [38], and direct fluorescent labeling of such components, for example via Lifeact [53]. The highlighted methods all require the addition of extrinsic bodies into the cell, some of which adhere to cellular components. Such introduction of foreign objects could alter the intrinsic dynamics of the cell cortex and its interactions with other biochemicals or cell components in ways that are not well characterized, leading to errors in the acquired results.

The granules embedded in the *Patiria miniata* sea star oocyte cytoskeletal mesh are endogenous, passive, and highly fluorescent. Thus, they require no perturbations, nor the addition of foreign bodies, for tracking the local motion of the cellular actomyosin cortex. As such, these endogenous granules make excellent passive probes for visualizing the deformations of the cellular cortex in response to RhoA activity. Since both the Rho family of chemicals as well as the underlying make-up of the actomyosin cortex is conserved across a wide range of cell types, the results attained from this project will shed light on universal properties of mechanochemical coupling in biological systems.

2.3 Co-imaging RhoA spiral waves and endogenous fluorescent granules

How cells communicate with force generating signaling molecules, such as RhoA, to change their shape robustly and reliably is still not fully understood. By co-imaging the evolving reaction-diffusion based activity field of the biochemical RhoA simultaneously with the spatiotemporally patterned deformations of the cortex, it is possible to quantitatively uncover the dynamic mechanical strain patterns generated by RhoA activity on the cellular actomyosin cortex *in vivo*.

Since the emission spectrum of cortex embedded fluorescent granules lies largely in the infrared wavelength region, these granules can be imaged via fluorescence microscopy, by using a visible wavelength excitation laser and a far-red emission filter, such as Cy5 (700/75nm). At the same time, RhoA activity can be probed via a Rho-GTP reporter, which has been tagged with the green fluorescent protein (GFP). Through the use of multi-channel confocal fluorescence microscopy, these two fields can be imaged concurrently with high temporal resolution.

In order to maximize the temporal resolution of the time lapse images of RhoA and granules, the imaging plane must consist of a flat surface, parallel to the imaging plane. This is due to the fact that confocal microscopy rejects out of focus light, therefore improving the signal-to-noise ratio. If the oocyte membrane lies on a curved surface, many image slices would need to be acquired in order to construct a region of a desired size. Due to this, after the maturation of GEF overexpressed *Patiria miniata* oocytes, the cells are placed between a glass slide and a cover slip separated by a gap of around 100μm, squeezed into a pancake shape, as shown in Figure 2-2a. Through this setup, a flat surface of around 100-200 μm in diameter is attained. Via this method, the number of z-stacks (repeat images taken at different focal depths) is minimized, and a temporal resolution of 8 seconds per frame is realized.

2.4 Obtaining strain patterns in the actomyosin cortex from fluorescence imaging of passive probes

The IR fluorescent granules were identified and their motion tracked using u-Track, a versatile particle tracking software from Danuser Lab. Through the use of this method, it was possible to identify the instantaneous velocities of the visible granules at any point in time. Yet, in order to uncover the deformations of the actomyosin

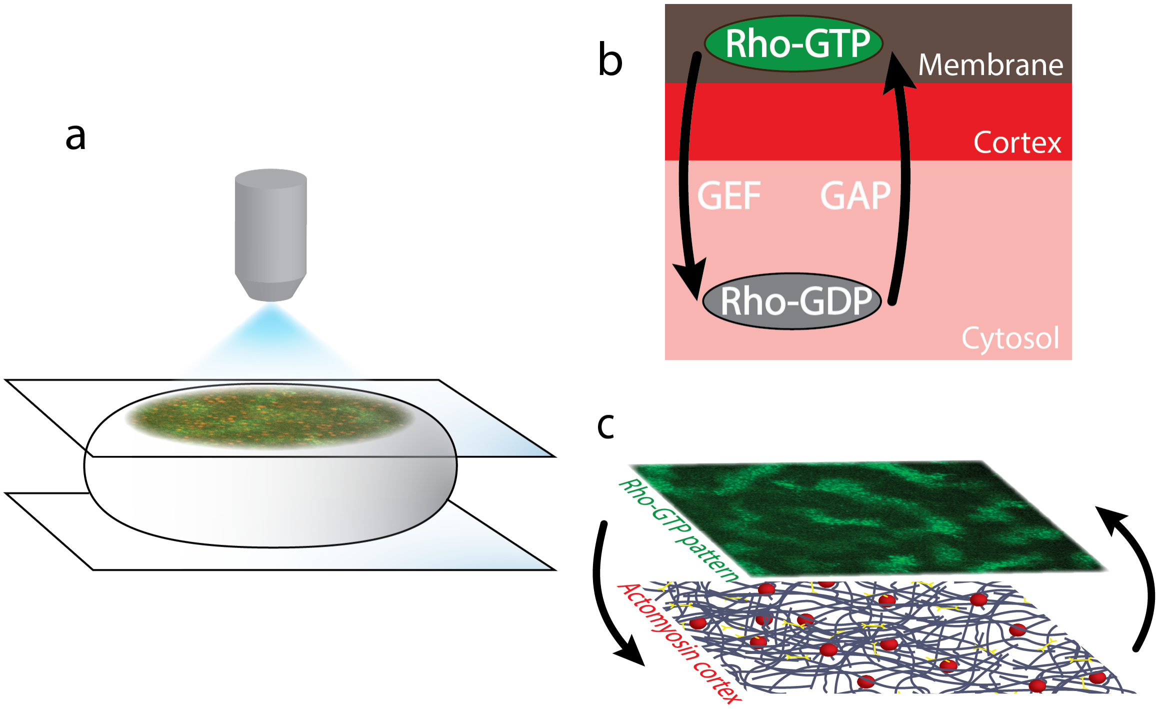

Figure 2-2: Coimaging spatio-temporal patterns and cellular actomyosin cortical deformations. **a** Fluorescence imaging set up for coimaging Rho fluorescent reporter and cortical granules. The GEF over-expressed oocyte is pressed between a glass slide and a cover slip. The imaging is performed on the flat part of the oocyte pressing against the cover slip. Coherent laser light source is used to excite the fluorescent substances, and imaged via the appropriate fluorescence emission filters. **b** A simplified diagram showing the Rho GTPase reaction network. Rho is activated/inactivated by GEF/GAP. Rho-GTP, the active form, is associated with the cell membrane while Rho-GTP, the inactive form, diffuses in the cytosol. The cell cortex lies in between the cytoplasm and the membrane. **c** The Rho-GTP patterns, which lie directly above the actomyosin cortex, drive deformations through the spatio-temporal organization of forces. Through various mechanisms, these deformations could affect the evolution of the Rho patterns.

cortex, the velocity field of the entire field of view needed to be constructed. This field was attained by using particle image velocimetry (PIV), through PIVLab.

2.4.1 Calculation of strain rate and principal strain rate components

The two-dimensional velocity field $\vec{U}$ of the cortex was obtained from PIVLab in the form of

$$\vec{U}(x, y, t) = (u(x, y, t), v(x, y, t)),$$

where u denotes the local velocity in the horizontal direction, and v denotes that of the vertical direction. The velocity spatial gradient tensor, or the strain-rate tensor, was calculated as

$$\mathbf{L} = \boldsymbol{\nabla}\vec{U} = \begin{bmatrix} \frac{\partial u}{\partial x} & \frac{\partial u}{\partial y} \\ \frac{\partial v}{\partial x} & \frac{\partial v}{\partial y} \end{bmatrix}.$$

The affect of any global translational movement of the cortex, such as in the case of drift of the microscopy stage, is eliminated via this method.

The strain-rate tensor $\mathbf{L}$ can be decomposed into its symmetric and anti-symmetric components. The symmetric tensor

$$\dot{\epsilon} = \frac{\mathbf{L} + \mathbf{L}^T}{2}$$

denotes the rate of shear, compression, and stretch along the x and y directions. The anti-symmetric tensor

$$\dot{\omega} = \frac{\mathbf{L} - \mathbf{L}^T}{2}$$

describes the rotation rate of the local region. The rate of pure expansion/contraction, or area change, can also be calculated simply by taking the trace of $\mathbf{L}$, which is equal to that of $\dot{\epsilon}$.

In order to uncover the magnitude and orientation of maximal strain-rate, $\dot{\epsilon}$ can be separated into its two eigenvalues λ_1 and λ_2, which express the amplitude, and eigenvectors ν_1 and ν_2, which denote the directions of maximal strain rate. By construction, the eigenvalues only have real values, and the two eigenvectors are orthogonal to one another. Through this formulation, it is possible to uncover not only the rate of local area change, but also the amount and direction of highest deformation.

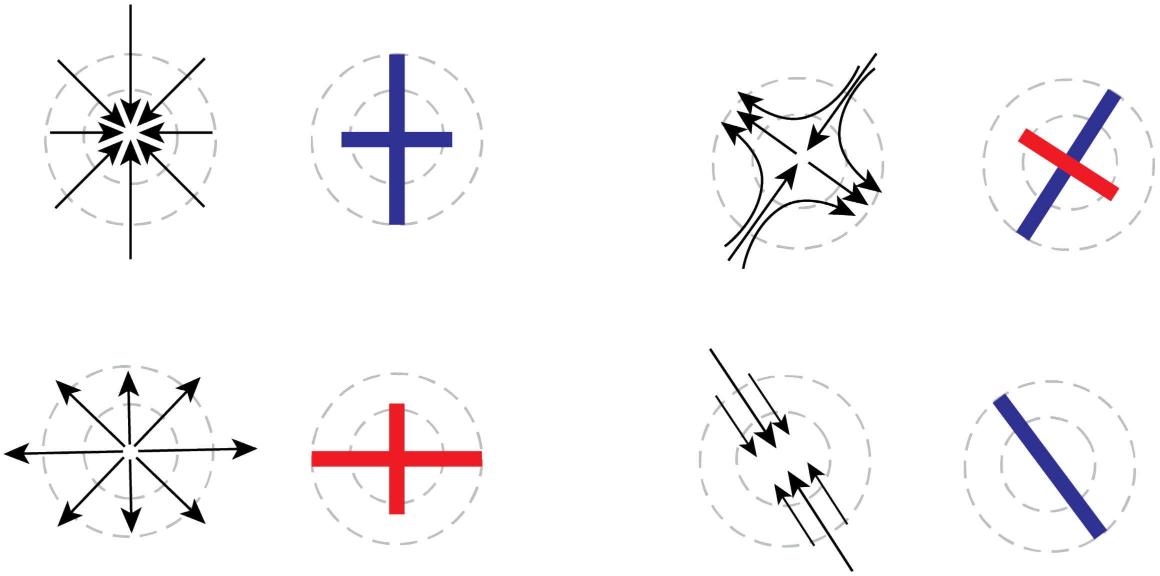

Figure 2-3: A schematic drawing demonstrating principal strain rate component representations for various velocity fields. The components are expressed as two orthogonal, intersecting lines. Blue/red color represents contractile/extensile motion, and the length of the line represents the magnitude of the strain rate component. A lack of line corresponds to translational, rotational, or no motion. The orientation of the lines denote the angle of the principal strain rate component, which is equivalent to the direction of maximal deformation.

While local area change can be depicted via a simple heat map, in order to illustrate both the amplitude and the orientation of the principal strain-rate components, a representation shown in Figure 2-3 is chosen. For any point, for which $\lambda_{1,2}$ and $\nu_{1,2}$ are calculated, two perpendicularly intersecting lines are drawn, with lengths proportional to $\lambda_{1,2}$, and orientations given by $\nu_{1,2}$. Blue/red lines denote contraction/expansion for that particular (λ, ν) pair. Depending on the local velocity profile, the components can have the same or opposite sign. For instance, for a purely contractile region, both components will be colored blue, as depicted on the top left schematic of Figure 2-3. For pure shear without local area change, the two lines will have different colors, with orientations corresponding to their respective eigenvectors.

2.5 Results and Discussion

2.5.1 Rho intensity oscillations and circular granule motion

For GEF over-expressed *Patiria miniata* oocytes, RhoA fluorescence intensity manifests as an oscillatory signal at any spatial point with constant periodicity in time (Figure 2-4 b), during the period of interest.[1] Oocytes exhibit differing RhoA activity patterns with distinct temporal oscillation frequencies. The normalized temporal power spectral densities of RhoA activity from two distinct oocytes is shown in Figure 2-4e.

Granule motion obtained from u-Track also reveal patterned behavior. As shown in Figure 2-4c and d, the motion of the granules is circular, though they also exhibit domain specific drift. (As mentioned in the previous section, global drift will not affect the strain-rate calculations performed later in the chapter, but spatially varying drift will factor in.) The overall movement of the granules is governed by various distinct sources: thermal noise, actin architecture remodeling, and active drive, for instance those originating from RhoA patterning. The effects of these sources are separated in timescales. Thermal noise generally dominates motion at sub-second timescales, actin remodeling can take place on the order of one to tens of seconds [57, 56], and RhoA oscillations are observed to have periodicity of around 100 seconds. Since the temporal resolution available in this system is 8 seconds per frame, the calculated velocities of the granules are dominated by RhoA activity and the specific material properties of the actomyosin cytoskeleton on these timescales, and the effects of thermal noise are averaged out.

The normalized temporal power spectral density (PSD) of the horizontal velocity component of the granules, shown in Figure 2-4f shows that the spectrum exhibits a

---

[1] Pattern frequency varies during oocyte surface contraction waves accompanying meiotic division. The experiments covered in this chapter are conducted after these cellular events are completed, when the oocyte is exhibiting steady-state patterns with constant frequency and wavelength.

strong peak, very similar to that of the RhoA patterns. The location of the RhoA and granule velocity PSD peaks match closely, and as shown in Figures 2-4e and f, the granule velocity peak location changes with varying RhoA oscillation frequency. Such close pairing of the spectral peaks suggests that the two fields are strongly coupled to one another, with RhoA acting as a periodic drive for granule motion.

For the temporal PSD spectrum of RhoA activity, a significantly smaller yet clearly discernible peak at a higher frequency than that of the primary oscillation peak is also observed for both patterns. This originates from the anisotropy in duration between time periods of high and low Rho intensity.[2] Such behavior is clearly visible in the time series graph of RhoA activity oscillation in Figure 2-5c. Since PSDs are obtained from expressing the signal as a set of Fourier modes, higher modes are necessary to express such anisotropy between high and low activity in time. Even this higher frequency behavior is reflected in the granule motion, leading to the observation of a secondary peak at the same frequency in the granule velocity PSD.

2.5.2 Strong anti-correlation between Rho activity and rate of area change

The instantaneous velocity field of the entire field of view is obtained using PIV, from which the strain-rate field is calculated through the method outlined in Section 2.4. To compute the velocity field at a particular point in time, the PIV method compares consecutive images against one another. Thus, various timescales might be available to the observer, capturing a range of properties of the actomyosin cortex. While at short timescales elastic behavior is observed, at longer timescales, due to actin turnover, the stresses relax, and the cortex exhibits viscous flow. The crossover between the two timescales is characterized by the Maxwell time, or the stress relaxation time. For gastrulating zebrafish and single-cell *Caenorhabditis elegans* roundworm embryos, the Maxwell time is observed to be around 3-5 seconds [56].

---

[2] This effect arises from the duty cycle of the signal not being 50-50.

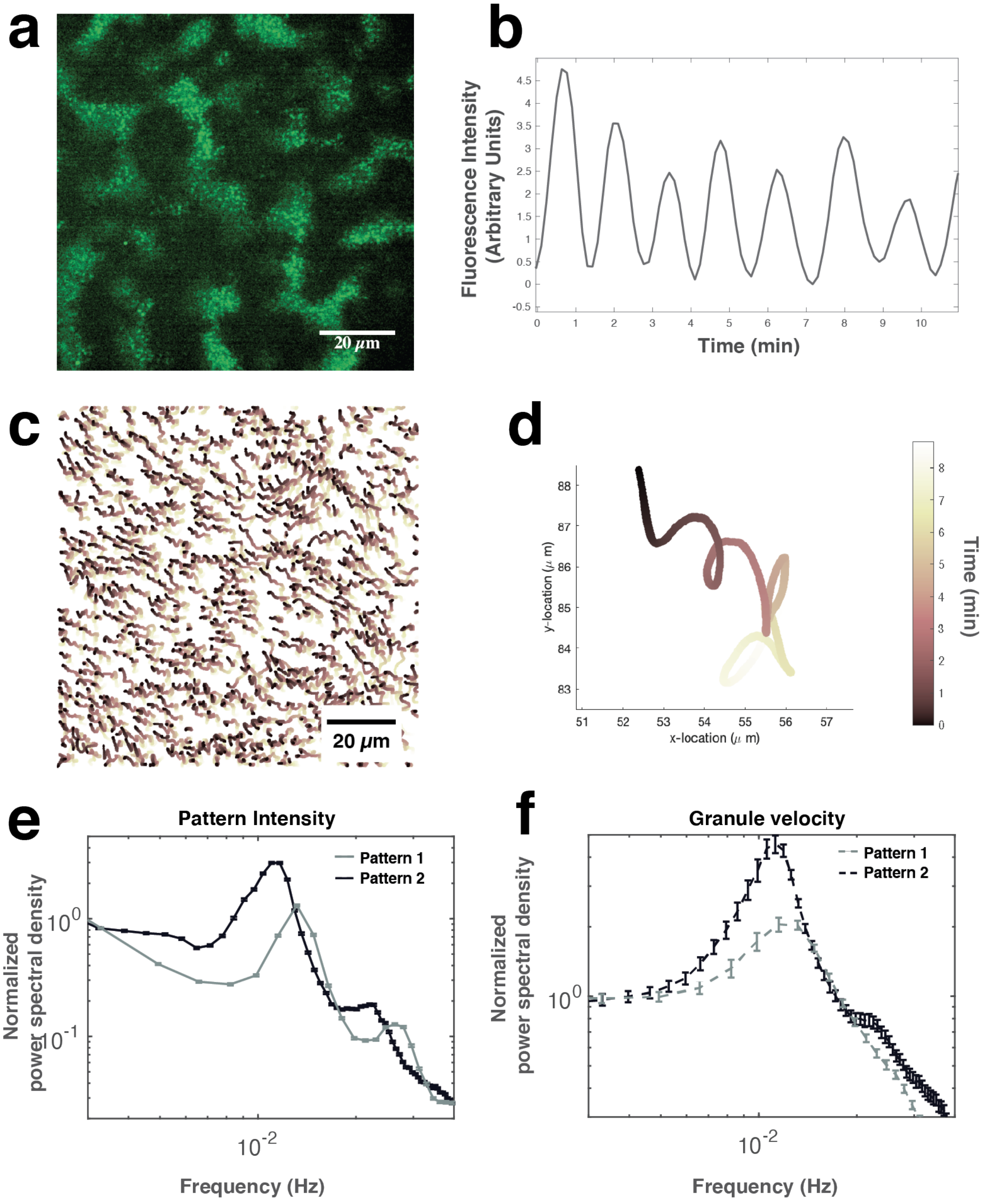

Figure 2-4: Rho pattern and granule motions and their temporal power spectral densities. **a** Rho fluorescence reporter intensity of the field of view at a time point. **b** The temporal oscillations of a point from panel a. **c** Worm plot showing the motion of the tracked endogenous granules within the entire imaging field. **d** The motion of a sample granule from panel c. **e** Normalized temporal power spectral density of Rho fluorescence intensity from two experiments. The two patterns have distinct oscillation frequencies measuring at 0.0117 and 0.0129 Hz. **f** Normalized temporal power spectral density of granule velocity from the same two experiments from panel e. The velocity oscillation frequencies measure at 0.0112 and 0.0123 Hz, consistent with the prominent temporal oscillation peaks of the Rho patterns.

In this experimental system, the temporal resolution available to us is 8 seconds per frame. Furthermore, PIV analysis is done on pairs of every other frame (e.g. frames 1 and 3, 2 and 4, etc..). Therefore, the time difference between consecutive frames of comparison becomes 16 seconds. Comparing this value to the experimentally observed Maxwell times of other model systems leads us to believe that the observed physical material properties of the actoymosin cortex may be similar to that of a compressible, two-dimensional viscous fluid.

For linear elastic materials, strain (ϵ) is proportional to stress, which in this experimental system would arise from the forces induced by Rho activity. While for viscous materials, stress is proportional to strain-rate ($\dot{\epsilon}$). This led us to explore the relationship between Rho activity on the oocyte membrane and the cortical strain-rate field.

The local expansion and contraction of the field at each spatial and temporal point was calculated (Figure 2-5b) by taking the trace of the strain-rate tensor, $\mathbf{Tr}(\dot{\epsilon})$. Not only were both contractile and extensile areas observed, but these regions evolved closely following RhoA fluorescence intensity. In time, the compressive strain rate $\mathbf{Tr}(\dot{\epsilon})$ exhibited oscillatory behavior at each spatial point with the same frequency as that of RhoA (Figure 2-5c). For regions with high RhoA activity, contractions of up to 0.0075 s^{-1} or 0.45 min^{-1} were observed, consistent with the understanding that RhoA directs the contractile machinery of the actomyosin cortex. For regions with low RhoA activity, local expansion was observed at similar rates as the contractile regions.

Three-dimensional cross-correlation analysis was performed between the Rho intensity field and the compressive strain-rate field. The contour plot resulting from this analysis is displayed in Figure 2-5d. The cross-correlation coefficient, which gives the similarity between the two fields, decays to zero as the spatial offset is increased in any direction. Since we believe there to be no preferred spatial orientation, this result is consistent with our understanding of the biological system. This decay length is around a few microns, consistent with the size of high Rho activity regions.

As the time offset is varied, the cross-correlation coefficient oscillates between

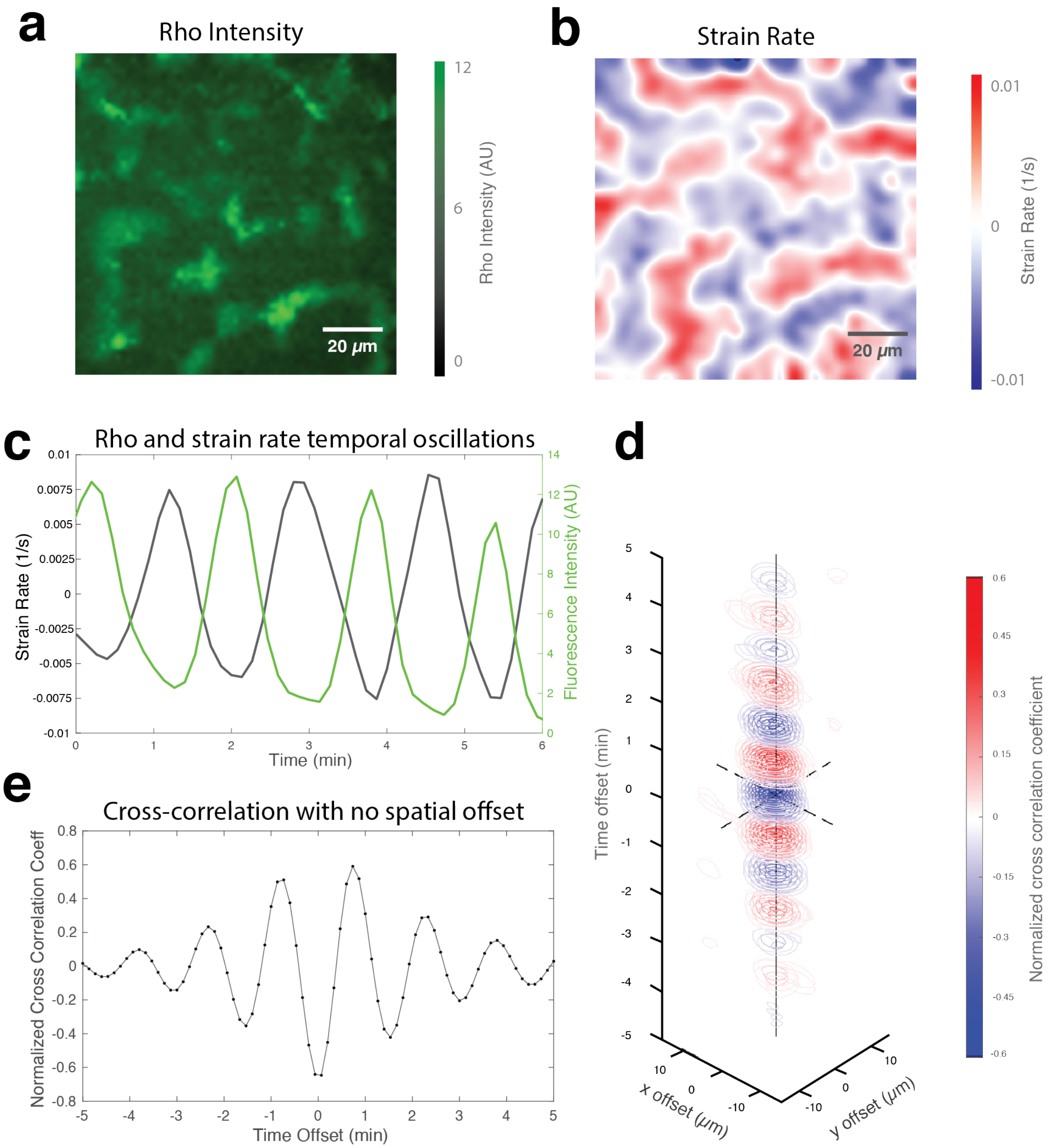

Figure 2-5: Three dimensional cross correlation between Rho fluorescence intensity and strain rate. **a** Rho fluorescence reporter intensity **b** Strain rate field of the field corresponding to the same time point as panel a. Red/blue regions correspond to local expansion/contraction. **c** Temporal oscillation of Rho fluorescence intensity and strain rate of a sample point from fields shown in panels a and b. **d** Contour plot of 3D normalized cross-correlation of Rho fluorescence intensity and strain rate in space (2D) and time. The dashed lines correspond to axes of no spatial offset in X and Y along zero time offset. The solid black line denotes the axis along which there is no spatial offset. Red/blue denotes positive/negative cross-correlation coefficient. **e** The values along the solid black line from panel d.

positive and negative values, as demonstrated in Figure 2-5e. This behavior can be attributed to the sinusoidal nature of the RhoA activity and the compressive strain-rate fields. The amplitude of the cross-correlation coefficient also decays as the time offset is increased in either direction. This slow decay is due to the high level of spatial self-similarity of RhoA patterns after each oscillation, which only exhibits large variation after multiple cycles. The largest anti-correlation between RhoA activity and cortical extensile behavior occurs at a value close to zero temporal offset, indicating that the interactions are close to instantaneous on the scale of the shortest time difference observable.

This analysis demonstrates that high Rho activity drives local and highly dynamic actomyosin contractility with astounding spatial precision. Rho intensity is found to be proportional to local compressive strain-rate with the biochemical activity translating into cortical deformations within the experimental time resolution. Away from high Rho regions, the cortex is also observed to exhibit a positive rate-of-change in its area, corresponding to local expansion.

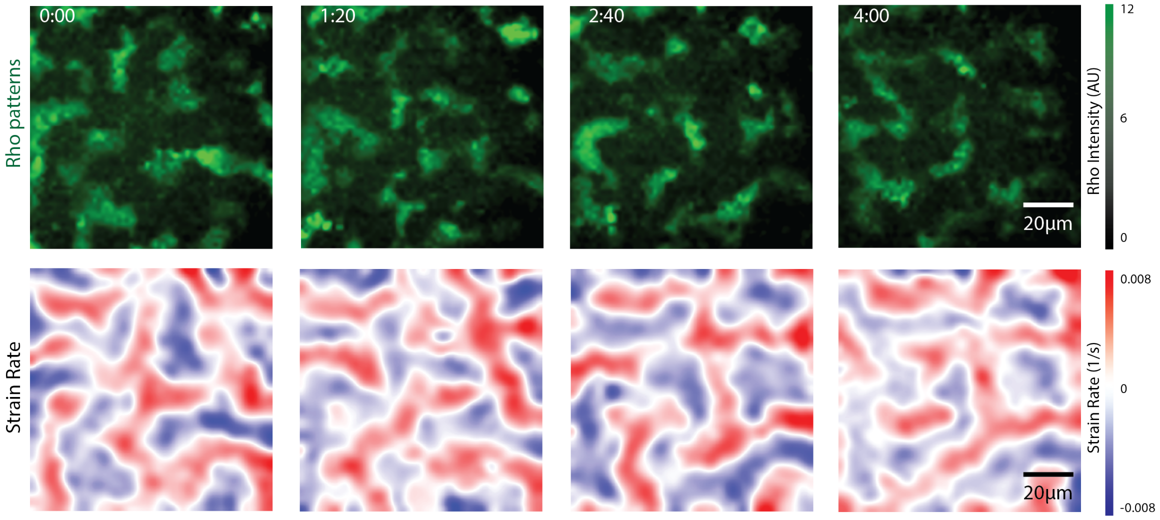

Figure 2-6: Rho fluorescence intensity (top row) and corresponding compressive strain rate maps (bottom row) for an oocyte expressing spiral Rho activity patterns. Positive strain rate denotes local expansion, and negative strain rate denotes local contraction. The time stamp is denoted in mm:ss format.

2.5.3 Strain rate during meiotic contraction wave

The calculation of compressive strain-rate was repeated for wildtype oocytes without GEF overexpression, during the meiotic surface contraction wave. A traveling wave of contractile region, lying in between two extensile regions was observed (Figure 2-7a and b). Computer simulations were performed to model the behavior. 200 point particles were scattered randomly in the 2D window. These particles were moved with respect to the biochemical concentration field $C(x_i, x_j, t)$, and also experienced random fluctuations by means of a normally distributed noise added to their instantaneous velocity at each time point. The particles only sensed the local biochemical field and its spatial derivatives, and no coupling from the mechanical field to the chemical concentration was considered.

The interactions between the two fields were modeled as

$$\frac{\partial C(x_i, x_j, t)}{\partial x_{i,j}} \propto v_{i,j}(x_i, x_j, t),$$

with $C(x_i, x_j, t)$ denoting the local biochemical concentration field, and $v_{i,j}(x_i, x_j, t)$ denoting the local velocity in the $\hat{\imath}$ and $\hat{\jmath}$ directions, coupled via a proportionality constant.[3] With this interaction, a behavior similar to that of the experimental system was observed: a traveling wave of contractile strip, inlaid between two rows of extensile regions (Figure 2-7c and d).

These results corroborated the findings from GEF over-expressing oocytes exhibiting spiral waves, namely that traveling Rho activity and local compressive strain-rate are anti-correlated. As this simple coupling was able to capture key components of the experimentally observed interactions, it can act as a springboard from which to explore more complex and elusive features of the interplay between the two fields.

---

[3] The strain-rate tensor was calculated by performing quasi-conformal mapping, using the point particles as landmarks. More information about this method can be found in section 2.6.3.

[b]

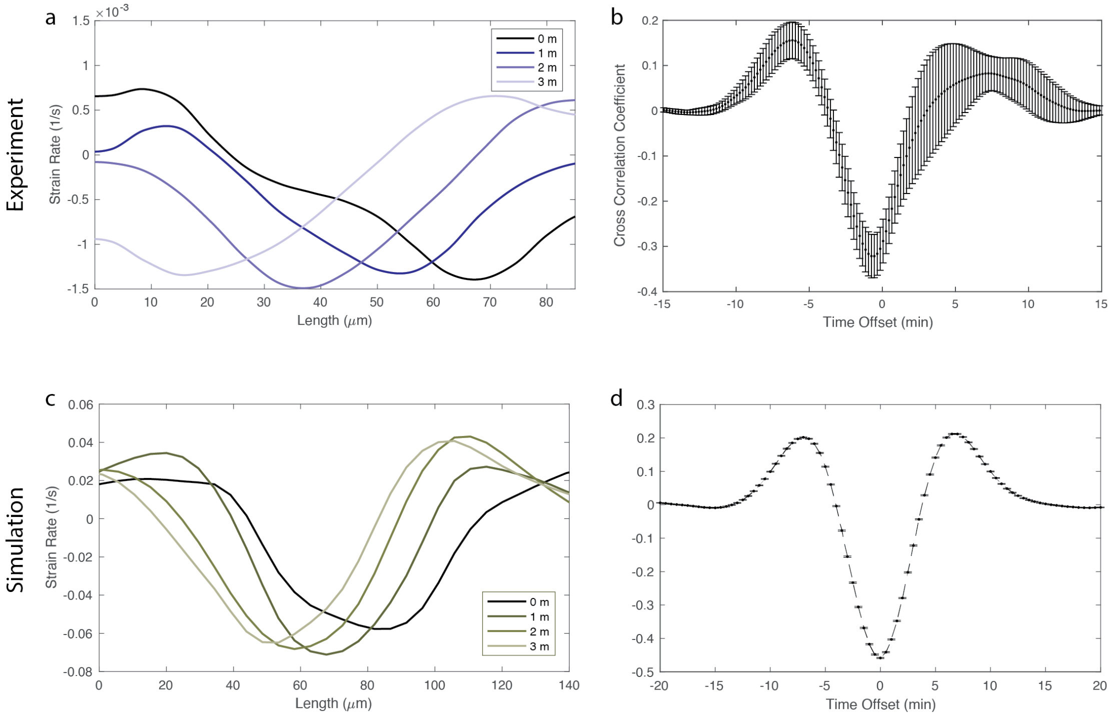

Figure 2-7: Strain rate resulting from a traveling Rho wave matches closely with a computer simulation of a traveling Gaussian wave coupled to the local mechanical field via $\partial C(x_i, x_j, t)/\partial x_{i,j} \propto v_{i,j}(x_i, x_j, t)$. **a** (**c**) Rate-of-change of area resulting from an experimental observation (computer simulation) of a traveling surface contraction wave. **b** (**d**) Normalized cross-correlation of experimental (simulated) Rho fluorescence intensity and compressive strain-rate.

2.5.4 Principal strain-rate components of the actomyosin cortex deformations

In order to reveal a more detailed relationship between Rho activity and cortical strain-rate, the principal strain-rate components were calculated using the method outlined in Section 2.4. As shown in Figure 2-8a, extensile (red) regions were found to correspond to those of low Rho activity (black), and contractile (blue) patches matched closely with those of high Rho activity (white), consistent with the results obtained in the previous section.

Furthermore, most regions were found to exhibit strain rate component amplitudes of the same sign (both contractile or both extensile), except for areas at the borders of the Rho pattern, where the magnitudes of both eigenvalues were low.

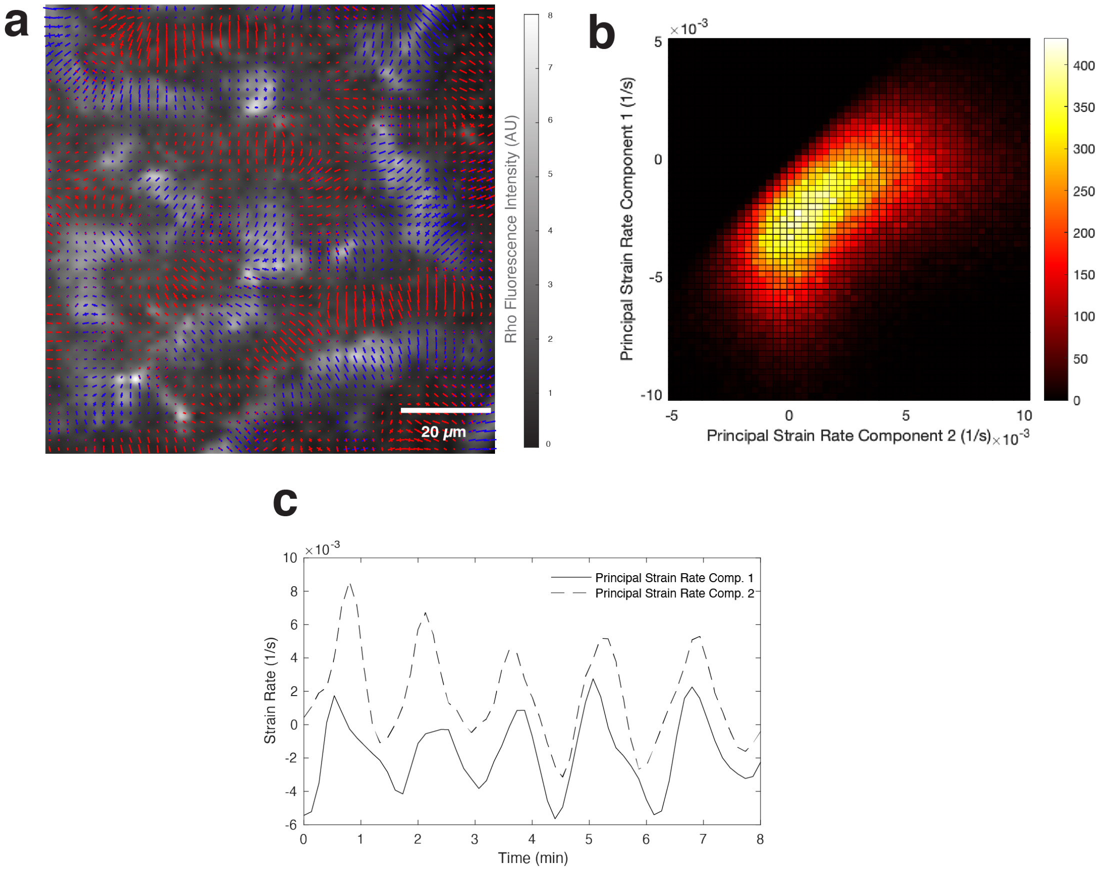

Figure 2-8: Principal strain rate components observed in the experimental system. **a** Rho fluorescence intensity (grayscale) overlaid with principal strain rate components at the same point in time. The strain rate components are represented as described in Figure 2-3. **b** Histogram showing the relationship between the magnitudes of the two principal strain rate components. **c** The highly correlated temporal oscillations of the magnitudes of the two strain rate components of a point.

These also corresponded to the regions of small compressive strain-rate, similar to the areas colored white in Figure 2-5b. In addition, like the compressive strain-rate field, each individual eigenvalue also displayed periodic oscillations in time (Figure 2-8c), precisely in phase with one another, and in a linearly correlated manner (Figure 2-8b).

Overall, the deformations tended to be dominated by a single principal strain-rate component, indicating that a large proportion of local cortical stretch or compression could be characterized by a single direction. The orientation of this component strongly aligned perpendicularly with the wave front, or parallel to the short axis of the Rho pattern. This behavior was observed for regions of high Rho activity as well as low.

Such spatially coordinated deformation points to a non-negligible hydrodynamic length scale, the characteristic distance of force propagation. This value varies widely for different biological model systems, from 14.4μm in *Caenorhabditis elegans* embryonic cells to 67.6μm in zebrafish embryos [56]. It is possible to uncover the mechanical properties of the cortex, such as the hydrodynamic length, of sea star oocytes by extending the approach highlighted in this chapter.

In summary, through a simple biochemical manipulation, *Patiria miniata* sea star oocytes were shown to express dynamically evolving RhoA activity patterns on their membranes. Such RhoA activity was found to induce surface deformations through its interactions with the cellular actomyosin cortex. Using cortex embedded fluorescent granules, these deformations were tracked in real time, alongside the RhoA patterns, with high spatial and temporal resolution, on the order of microns and seconds respectively. The use of these endogenous granules allowed for the mechanics of the cell cortex to be uncovered via passive mechanical probes without the introduction of any external objects or other physical manipulations.

RhoA activity was found to act as an oscillatory driver of local cytoskeletal motion, with frequencies of around 0.01 Hz (Figure 2-4). By calculating the rate-of-change of local surface area, RhoA activity was also shown to create cortical deformations with excellent spatial precision, exhibiting compressive strain-rate maps nearly identical to the RhoA patterns. Finally, through the analysis of principal strain rate components in all experimentally available spatial and temporal positions, the maximal deformations were discovered to be highly correlated with the overall shape of the RhoA activity patterns, lying parallel with the direction of motion, and perpendicular to the wave front, suggesting long-range force propagation.

This work provides a framework for a quantitative understanding of the relationship between Rho activity on the sea star oocyte membrane and cortical deformations with micron scale resolution. Since Rho is a highly conserved, contractility driving biochemical responsible for a plethora of vital cellular processes, these findings pave the way for uncovering common features of coupled mechanochemical biological systems.

2.6 Future work and outlook

2.6.1 Actin as an additional constituent of the mechanochemical system

Actin filamentous proteins make up the scaffolding of the cellular actomyosin cortex, the cytoskeletal mesh on which myosin molecular motors apply forces, leading to cell deformations. Variations in actin density and filament organization lead to changes in cortical stiffness, and previous work has shown that cells dynamically regulate this property throughout various stages of life in order to accurately and effectively accomplish necessary cellular processes [20, 31]. In addition to recruiting myosin II and creating local forces on the cortex, Rho has also been shown to interact with actin filaments, increasing polymerization [58]. In turn actin may act as an inhibitor of active Rho [5].

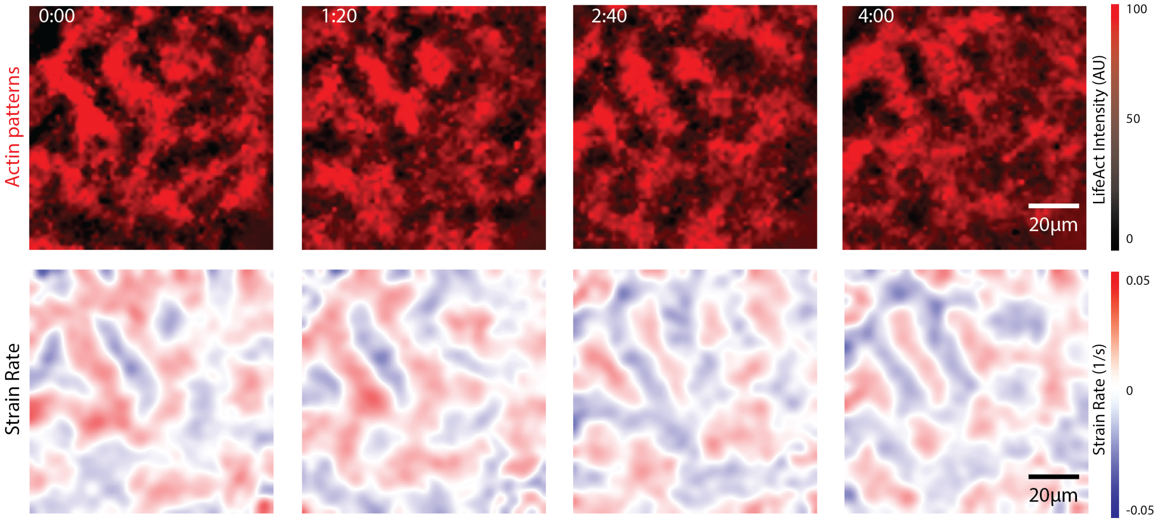

Figure 2-9: LifeAct fluorescence intensity (top row) and corresponding compressive strain rate maps (bottom row) for an oocyte expressing spiral Rho activity patterns. Positive strain rate denotes local expansion, and negative strain rate denotes local contraction. The time stamp is denoted in mm:ss format.

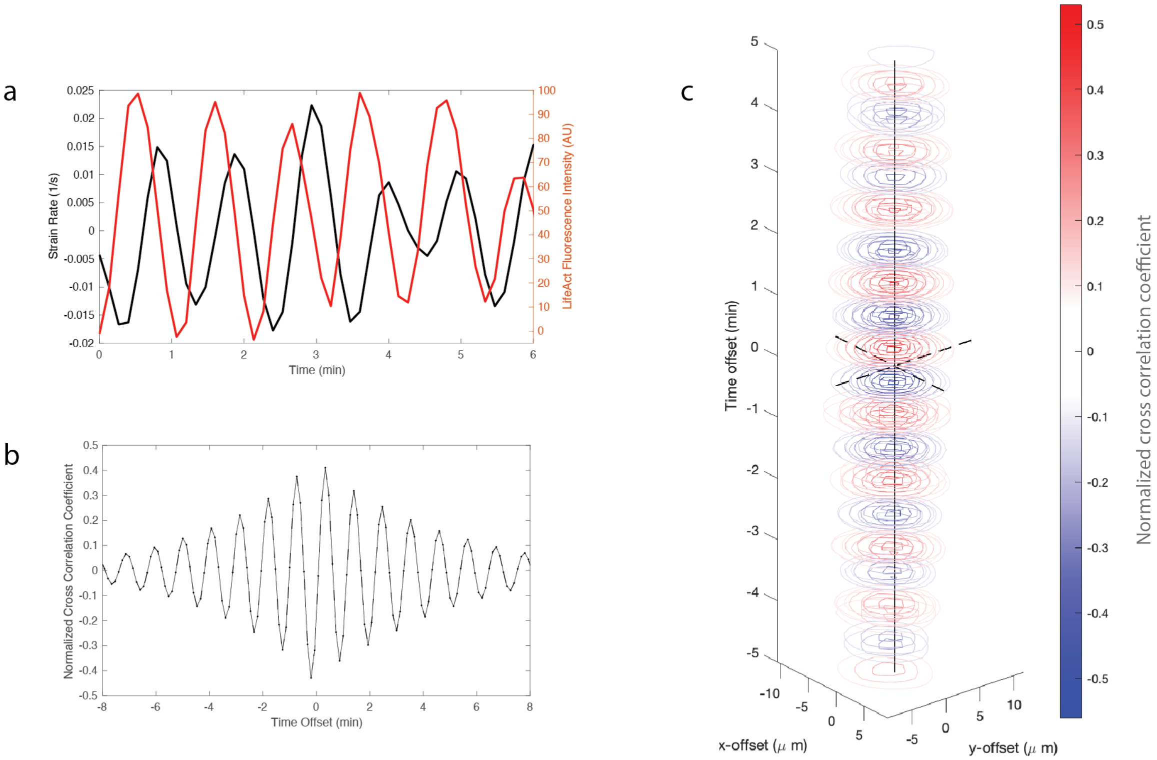

Figure 2-10: Three dimensional cross-correlation between LifeAct fluorescence intensity and strain-rate. **a** Temporal oscillation of LifeAct fluorescence and compressive strain-rate of a sample point from Figure 2-9. **b** Normalized cross-correlation coefficient for no spatial offset. **c** Contour plot of 3D normalized cross-correlation of LifeAct fluorescence intensity and compressive strain-rate in space (2D) and time.

Such dynamic relationship between Rho and actin leads to spatiotemporal patterning polymerized actin density, which we have observed via the use of fluorescent LifeAct, a marker for actin (Figure 2-9). These polymerized actin density waves may create spatial variations in cortex stiffness which evolve in time, and may even locally pattern other mechanical properties such as Maxwell time and the hydrodynamic length. Uncovering the spatially and temporally dependent mechanical properties of the cortex will shed further light into the coupling between Rho and the individual constituents of the cellular actomyosin cortex. Control of Rho, through, for instance, optogenetic tuning, could also serve as a way to selectively modify the local mechanical properties of cellular actomyosin cortices.

Furthermore, in this chapter, only a unidirectional relationship between biochemical patterning and mechanical deformations has been considered; RhoA, through its downstream effectors such as actin and myosin, has been shown to induce patterned deformations on the cell cortex. Yet, mechanical components may feed back into the RhoA patterns and play a role in altering them. Such an effect could partially stem from the interactions between Rho and actin. Thus, it might prove necessary to include the actin field in attaining the complete and detailed mechanochemical model between Rho and the cellular cortex.

2.6.2 Extending the mechanochemical model to 3D using spherical harmonics

In deforming the oocyte into a pancake shape by squeezing it between a microscopy slide and a cover slip, as shown in Figure 2-2a, we aimed to partially simplify the cell geometry, reducing it from a curved three-dimensional, to a flat quasi two-dimensional surface. This allowed for both increased temporal resolution in imaging using confocal fluorescence microscopy, and also reduced the dimensionality of the mechanical properties calculated from the experimental data. Yet, in nature, cells are truly 3D systems, contracting, expanding, and deforming in complex manners that may not be captured by a 2D model.

This experimental system can be extended to three dimensions by representing the patterns as a summation of spherical harmonic functions, which form an orthonormal basis for spherical geometries, at each point in time. By removing higher modes, using such a method could also aid in the denoising of experimental data. As previously mentioned, imaging a spherical oocyte of around 170μm depth using conventional confocal fluorescence imaging would lead to very limited temporal (cycle time on the order of minutes) as well as depth resolution (adjustable, but generally on the order of a few microns). Furthermore, spatial resolution would suffer as the depth is increased, likely leading to the inability to attain high quality fluorescence images of the hemispherical surface facing away from the objective. More sophisticated imaging systems such as light sheet fluorescence microscopy, which boasts high imaging speed and excellent optical sectioning, could be used to overcome these problems.

With this set up, granules could be tracked in three-dimensions, and the strain rate maps of the entire oocyte surface could be constructed. The strain rate, membrane curvature, and Rho fluorescence intensity fields could be expressed as a summation of spherical harmonic modes:

$$I(\theta, \phi, t) = \sum_{l,m} c(l, m, t) * Y_l^m(\theta, \phi)$$

where $I(\theta, \phi, t)$ denotes the mechanical or chemical field in question in spherical coordinates as projected onto a unit sphere, $Y_l^m(\theta, \phi)$ the spherical harmonic functions, and $c(l, m, t)$ the associated coefficients. Via this method, the actomyosin cortex response to Rho activity at different length scales can also be explored (Figure 2-11).

2.6.3 Constructing the constitutive relationship between RhoA and cortical deformations

In order to fully uncover the relationship between RhoA activity and cell surface deformations, a constitutive relationship between the mechanical and biochemical fields must be constructed. As can be seen from the model in Appendix A, this might require the need to take multiple spatial derivatives of the biochemical and the mechanical deformation fields. The model could also be extended to include temporal derivatives. These derivatives could be taken via the finite difference method. Yet, not only does the experimental data suffer from noise, but each discretized pixel-wise derivative taking step would further amplify this noise, drowning out the signal. Thus, it is crucial to perform denoising techniques that represent the data well while also enabling derivatives to be taken robustly.

To achieve effective denoising, the experimental data can be transformed from real space to the appropriate basis. Assuming that the bases are separable in each dimension, the data can be expressed as

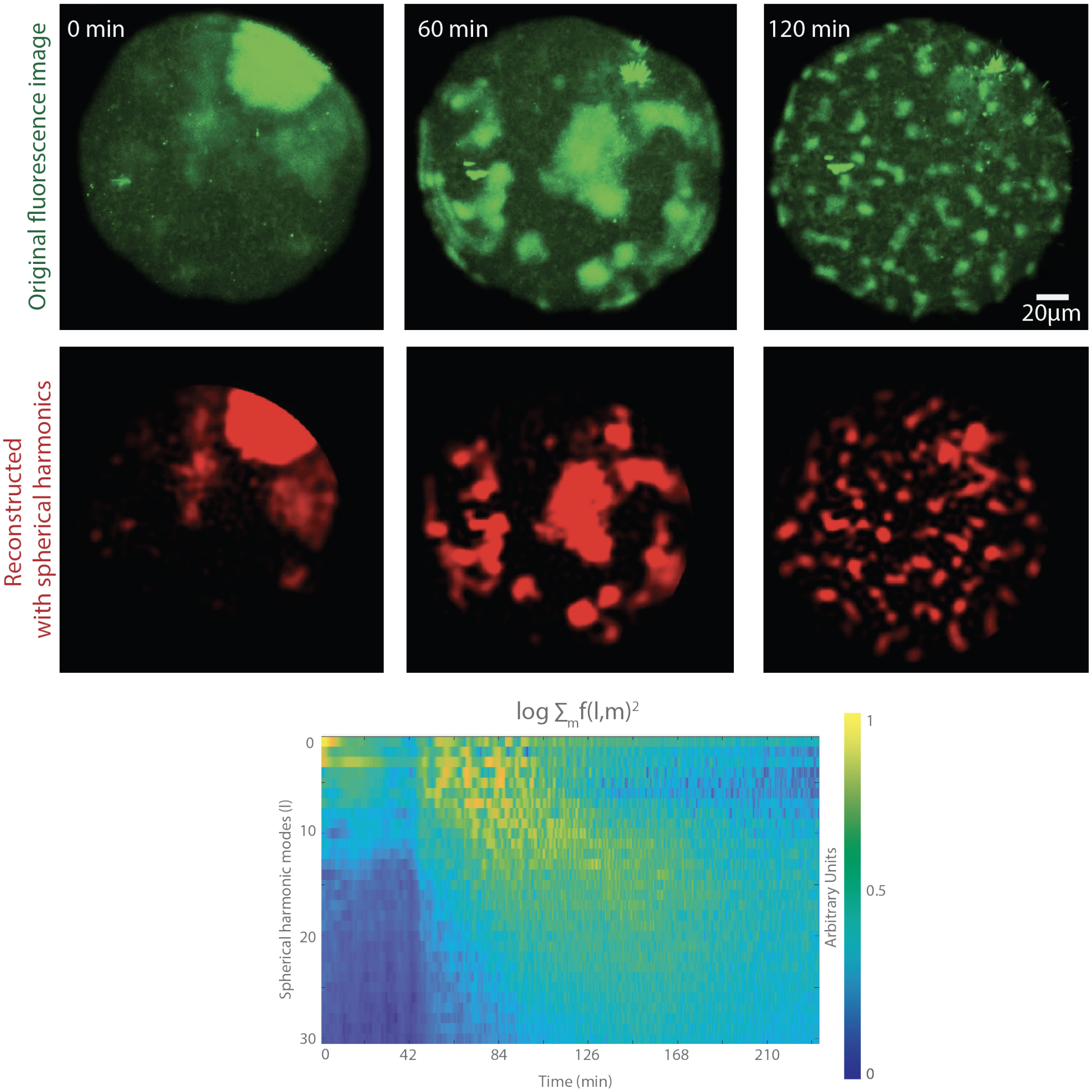

Figure 2-11: Reconstructing Rho activity patterns using spherical harmonic functions. The top row of images are those of an oocyte exhibiting non-steady-state Rho activity patterns that display decreasing length scale in time. This pattern can be expressed using spherical harmonics, denoised, and reconstructed (middle row). The spherical harmonic mode amplitudes are seen to reflect this ever decreasing length scale via the population of higher modes, as seen in the graph (bottom) showing the coefficients of spherical harmonic modes (l) as a function of time. (Experimental images courtesy of Dr. Tzer Han Tan.)

$$I(x,y,t) = \sum_{m}^{\infty}\sum_{n}^{\infty}\sum_{k}^{\infty} c_{m,n,k} X_m(x) Y_n(y) Z_k(t)$$

where $I(x,y,t)$ denotes the experimental data, X, Y, Z are the chosen bases in each dimension for a two dimensional video, and m, n, and k are the modes of their respective bases. Denoising is performed by removing higher modes and summing up to a selected threshold m_{max}, n_{max}, and k_{max}. Choosing the correct basis functions is crucial as the basis must represent the data well with the fewest number of modes in order to robustly remove noise while fully preserving the signal.

Furthermore, both spatial and temporal derivatives can be taken using the basis functions themselves, without the need of finite-difference methods, thus suppressing noise and achieving more robust calculations. As the functions have analytic expressions with values at any point, such representation of the signal can also be used to increase temporal and spatial resolution of the experimental videos. This, of course, would not represent the dynamics at smaller length and timescales than the experimentally sampled rate.

For the mechanical field, a unique and differentiable field must be attained. This can be achieved via quasi-conformal mapping, using granules as landmarks. Conformal mapping is an established method for quantifying shape changes on a domain. It can be visualized as tiling the surface with infinitesimal circles. Since conformal maps are angle preserving transformations, these circles map to other infinitesimal circles. As landmarks are used to constrain local deformations, angle preservation might not be possible. For this, quasi-conformal maps, which allow for angular distortions, shine as an alternative. In this transformation, circles are mapped onto ellipses, where the transformation satisfies the Beltrami equation

$$\frac{\partial f}{\partial \hat{z}} = \mu_f(z) \frac{\partial f}{\partial z}$$

where μ_f denotes the complex Beltrami coefficient. Performing a first-order approximation of f, the major and minor axes, as well as the angle of ellipses are calculated. The Teichmüller map is constructed by optimizing the transformation f

such that μ_f is constant everywhere. This optimization ensures that the minimum maximal dilation over the entire space is attained.

Applying this method on the starfish oocyte cortex, the granules can be treated as landmarks, their Teichmüller maps constructed with the appropriate constrains, and the strain and strain-rate tensors can be attained [14, 13]. This field can additionally be denoised using the same basis representation formalism described above.

Finally, using machine learning approaches, the differential equations relating the chemical and the mechanical fields can be constructed. Such an approach would not only shine light on the exact mechanical properties of the cortex and how Rho activity creates spatiotemporal forces on the cellular actomyosin cortex, but also whether the patterning of various mechanical constituents or deformations affect the Rho patterns that created them in the first place. This constitutive relationship then be tested by perturbing the mechanochemical system either globally, for instance through sequestering myosin II activity with the application of drugs, or locally, for example via mechanical shearing or pulling. [4]

2.7 Materials and methods

2.7.1 Oocyte preparation

The wild isolate *Patiria miniata* sea stars were procured from South Coast Bio-Marine and kept in a salt water fish tank with 35 ppt salinity at a temperature of 15^{o}C (59^{o}F). The extraction of oocytes was made through an incision of around 1 cm applied to the bottom side of the sea star. The extracted ovaries were placed in a beaker with calcium-free seawater with 35 ppt salinity to prevent maturation. The ovaries were repeatedly lacerated with scissors to release the oocytes. After the oocytes were washed twice in calcium-free seawater to remove ovary tissue, they were incubated at 15^{o}C in filtered seawater for up to three days.

---

[4] The work in this section is conducted in collaboration with the Dunkel Group at MIT. Basis representation of experimental data is developed by Alasdair Hastewell and quasi-conformal mapping of the oocyte cortex is performed by Dr. Gary Choi.

When maturation of oocytes arrested at prophase of meiosis I was desired, 1μM 1-methyladenine (1-MA) was added to a 1mL tube of saltwater solution containing 50μL of oocytes. Germinal vesicle breakdown of cells was observed at about 30 minutes post 1-MA addition. Fluorescence imaging was carried out starting two hours after the initiation of maturation to ensure steady-state RhoA activity patterns was observed.

2.7.2 mRNA synthesis and oocyte microinjection

A fluorescent RhoA reporter and a Rho-GEF mRNA construct was used in this study. eGFP-rGBD, a fluorescently labelled rhotekin binding domain construct, was used as the RhoA reporter. The construct was deposited to Addgene by William Bement and purchased by the Fakhri Lab from the company. Ect2-T808A-mCherry was used for the Rho-GEF construct. A gift from George von Dassow, this Ect2 mutant is not sensitive to a type of phosporylation by cyclin-dependent kinase 1 (Cdk1), a protein kinase and a cell cycle regulator.

The constructs were amplified by overnight growth of Ampicillin resistant bacterial culture in LB media at 37^oC. After lysing the bacteria, the plasmid was isolated using the Qiagen miniprep kit, and linearized through appropriate restriction enzyme digestion. The linearized plasmids were transcribed using the Thermo Fisher Scientific Invitrogen mMESSAGE mMACHINE SP6 Transcription Kit, and finally a poly(A) tail was added to the RNA transcripts with the Invitrogen Poly(A) Tailing Kit.

The *Patiria miniata* oocytes were microinjected with an mRNA mixture of eGPF-rGBD and Ect2-T808-mCherry and incubated at 15^oC for 24 hours to express the fluorescent proteins before imaging.[5]

2.7.3 Sample slide preparation

Two pieces of 100μm thick double sided tape were placed parallel to one another on a glass microscopy slide, leaving around a centimeter of gap between them. 20μL of oocytes that had been incubating in filtered seawater with 1μM 1-MA for 10 minutes

---

[5] The oocyte preparation, mRNA synthesis, and oocyte microinjection protocols are similar to those in Chapter 3 of this thesis.

were placed in the channel between the tapes. A coverslip was gently placed on top, making sure to cover the oocytes as well as both strips of the double sided tape. If the chamber was not fully filled, filtered seawater solution with 1μM 1-MA was pipetted from the side openings until the chamber was completely filled. VALAP, a mixture of vaseline, lanolin, and paraffin wax, was used to seal the chamber on all four sides. In this configuration, oocytes were pressed into the chamber, resembling a pancake shape, allowing for a flat imaging surface.

2.7.4 Confocal imaging

All imaging was carried out at the W.M. Keck Biological Imaging Facility located in the Whitehead Institute. The confocal images were acquired using the RPI spinning disk confocal microscope, which possesses a Zeiss AxioVert 200M inverted microscope frame and a Yokogawa CSU-22 spinning disk confocal scan head with Andor Borealis modification. A 488nm 150mW optically pumped semiconductor laser line light source was used to excite the fluorescent RhoA reporter molecules, and the GFP filter (525/50nm) was selected for the emission path. For the fluorescent endogenous granules, the same 488nm excitation laser was used, but for the emission path, Cy5 filter (700/75nm) was picked.

The Zeiss Plan NeoFluar 25X/0.8 multi immersion objective or the Zeiss Plan Apochromat 40X/1.3 oil immersion objective was used for optimal spatial resolution and window size. Images were captured by a Hamamatsu Orca-ER cooled CCD camera via MetaMorph image acquisition software. Image slices were acquired with a total frame rate of eight seconds, and maximum intensity projection was used to produce the final images.

2.7.5 Granule tracking

For granule identification and trajectory stitching, the MATLAB software u-track 2.0 from Danuser Lab was used. The software is publicly available on GitHub. After visually verifying the tracked granule locations and trajectories, granules that were tracked for fewer than ten frames were discarded.

2.7.6 Particle image velocimetry

For particle image velocimetry (PIV) analysis, the MATLAB software PIVLab from Dr. William Thielicke, was used. The software is publicly available on GitHub and MathWorks File Exchange.

The image differences were calculated between every other frame (e.g. frames 1 and 3, 2 and 4, 3 and 5, etc...). The velocity, strain rate, and other values associated with the deformation of the oocyte actomyosin cortex were placed at the time point exactly in between the frames in question. For example, if frames 10 and 12 were analyzed by the PIV software, the various output values would be assigned to the time corresponding to frame 11.

Chapter 3

In vivo tuning of self-organized biochemical patterns by dynamic mechanical deformations

> *"Go suck an egg.*
> *This expression has been used as a disparaging, dismissive comment –*
> *but for us, it became a research direction."*
>
> — Janice P. Evans and Douglas N. Robinson

3.1 Abstract

Robust yet intricate coordination between biochemical patterns and shape transformation of cells or tissues is vital to the survival of organisms. Yet, the mechanisms underlying this relationship are not fully understood. Through a simple biochemical perturbation, the oocytes of the starfish *Patiria miniata* can be made to express dynamical spiral patterns of the protein RhoA on their membranes, which induce active, local surface contractions. This system is an ideal biological model for exploring the coupling between biochemical patterning and mechanical deformations in evolving mechanochemical systems. In order to understand how changing geomet-

ric constraints affect such spatiotemporal biochemical patterns, we partially aspirate the oocyte using a micropipette. Through this method, it is possible to dynamically deform the surface in a highly controlled geometry. By combining live fluorescence imaging of RhoA patterns with micropipette aspiration, the evolution of the patterns inside the micropipette are imaged in real time. We show that the patterns, which display time and location dependent dynamics along the micropipette, can be manipulated via geometrical deformations induced by aspiration.

3.2 Introduction

3.2.1 Chemical and mechanical patterning in nature

Spatial and temporal protein patterning has been widely observed in many biological systems, from sub-cellular structures to multicellular units such as embryos and tissues [27]. For instance, spatiotemporal oscillations of Min proteins in *Escherichia coli* allow for the cell to find the center such that the two resulting daughter cells after division are equally sized [33]. In the yeast *Saccharomyces cerevisiae*, patterning of the biochemical Cdc42 acts as a polarity regulator, which determines the position of budding during asymmetric division [21]. In both of these examples, spatial protein patterns regulate the assembly of force-generating cellular components, resulting in mechanical deformations.

In these cases and many more, biochemical patterns arise concomitantly with cellular shape distortions, requiring the chemical patterns to continuously sense their mechanical environment, and evolve synchronously with it. Thus, changes in the geometry of the system could affect the spatial distribution of proteins accompanying dramatic deformations of living systems. While biochemical feedback mechanisms have been proposed [65], the fundamental nature of such coupling has remained elusive. Furthermore, how these biochemical networks are influenced by evolving geometries is largely unexplored.

3.2.2 RhoA directs and regulates cell contractility

GTPase proteins in the Rho family of biochemicals initiate and drive vital cellular processes involving contractility, such as cell division and migration, across a vast range of cell types [36]. Through their effectors such as Rho-associated coiled-coil containing protein kinase (ROCK) and Diaphanous Homologue (DIAPH), Rho proteins direct the organization of the cellular cytoskeleton and regulate the spatial patterning of myosin motor proteins that exert forces on actin filamentous proteins which make up the physical scaffold of the cell cortex. Specifically, the Ras homolog family member A (RhoA) protein is implicated in many cellular processes that necessitate controlled shape deformations. Thus RhoA is regarded as a master regulator of cellular contractility, playing a prominent role in the spatial and temporal coordination of cytoskeletal contractile dynamics.

Rho proteins switch between an active state and an inactive state (Figure 1-1), and can form regions of varying activity on the surface of the cell, leading to spatial and temporal patterning of surface contractility and cell deformations. Since Rho GTPase patterning determines dramatic shape changes in the cell, such mechanical deformations and Rho protein patterns span similar timescales, necessitating the need for the biochemicals to sense and adapt to the evolving geometrical constraints. Yet the mechanisms underlying such synchronous behaviors are still not fully understood.

3.2.3 Spatiotemporal RhoA patterns in sea star oocytes

During meiotic maturation of *Patiria miniata* sea star oocytes, the surface of the cell forms a ring shaped contraction. This contractile ring is co-localized with active RhoA and travels from one end to the other coinciding with the first asymmetric cell division. Ect2, the guanine nucleotide exchange factor (GEF) for Rho, is responsible for the activation of RhoA in this system. In the oocytes where the Ect2 concentration is increased, instead of a traveling contractile ring, spiral waves of active RhoA are observed (Figure 1-3). These spiral waves persist on the oocyte membrane with constant spatial and temporal properties, such as wavelength and oscillation frequency,

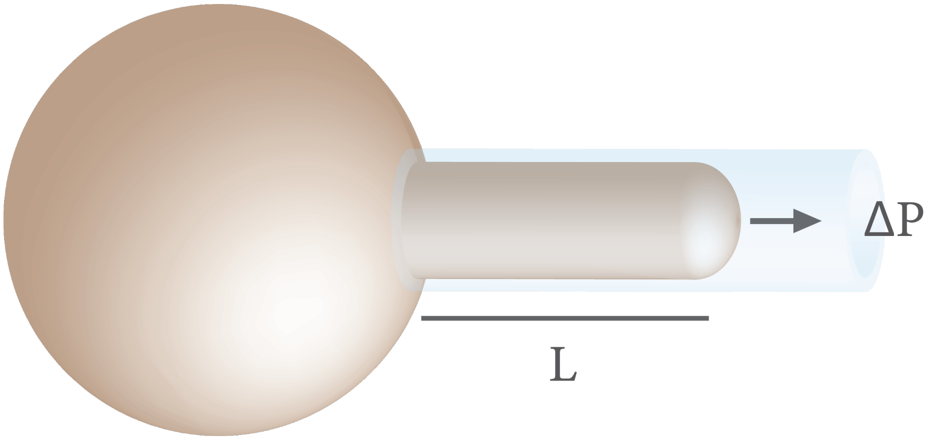

Figure 3-1: Schematic representation of partial aspiration of an oocyte. The pump lowers the pressure inside the micropipette which partially pulls the oocyte into the glass capillary. The pressure difference ΔP between the outside and the inside of the micropipette determines the speed of aspiration. The amount of aspiration is characterized by the length L of the oocyte inside the micropipette.

for several hours [5, 60]. Due to the ease of experimental accessibility of such dynamic biochemical patterns, *Patiria miniata* oocytes are an ideal model system for uncovering the behavior of spatiotemporal biochemical patterns in dynamically evolving geometrical constraints *in vivo*.

3.3 Micropipette aspiration

Micropipette aspiration is a non-invasive technique for assessing cellular mechanics of cells, cell aggregates, and embryos *in vivo*. It can be used to measure an array of mechanical properties such as cortical tension, elastic Young's modulus, and time-dependent viscoelastic behavior [32]. Though other methods, such as atomic force microscopy [26] and optical trapping of cells [2] have been used to exert forces on cells to uncover their mechanical properties, these methods only provide small (sub-nanoNewton) forces exerted over short (sub-μm) length scales. As such, these methods are not ideal for the study of large-scale cell shape changes, especially in big oocytes, embryos, or tissues. On the other hand, micropipette aspiration is capable of applying a precise amount of pressure over a well defined area, leading to the ability to generate tens of nanoNewtons of force over tens of μms. The technique can be used to impose well defined, temporally varying confinement to large cells.

The micropipette aspiration system, in essence, is comprised of a glass capillary with a narrow opening of a few μm^2 attached to a pump that is capable of providing a negative pressure differential between the inside and the outside of the capillary. The system is brought close to the biological organism of interest, and by applying suction, allowed to be partially aspirated into the mouth of the pipette. A schematic diagram of this process is shown in Figure 3-1.

Combining this method with microscopy allows for the time and pressure dependent behavior of the cell inside of the micropipette to be tracked. In general, cells exhibit viscoelastic behavior, with elastic response on short (up to tens of seconds) and viscous flow on long timescales. The Law of Laplace states that the pressure drop across an interface is equal to the curvature times the tension. In accordance with this law, as the pressure difference is increased, the cell is sucked in with increasing curvature, until it forms a hemispherical shell, where its largest distance into the micropipette is equal to the pipette radius. When ΔP exceeds this critical point, the cell starts exhibiting viscous flow, moving further into the micropipette. The speed of the flow can be controlled by adjusting ΔP. Furthermore, by manipulating the cytoskeleton-plasma membrane attachment-detachment dynamics, cells can be made to form blebs and exhibit more exotic behaviors such as oscillatory or saltatory motion [11].

Micropipette aspiration is also a versatile technique in its wealth of accessible geometries. Since the total force applied to the biological system is equal to ΔP times the area of the micropipette cross section, this also allows for a range of forces to be applied to the cell or tissue of interest. Diverse geometries such as those shown in Figure 3-2 can be attained by varying the velocity, heat, pressure, loop, and delay parameters of a needle puller. Though each micropipette puller will require its unique set of parameters to produce a particular micropipette shape, a general rule of thumb is to increase heat, pull, and velocity while decreasing time, delay, and pressure parameters for a longer taper, leading to a smaller tip, and vice versa for a shorter

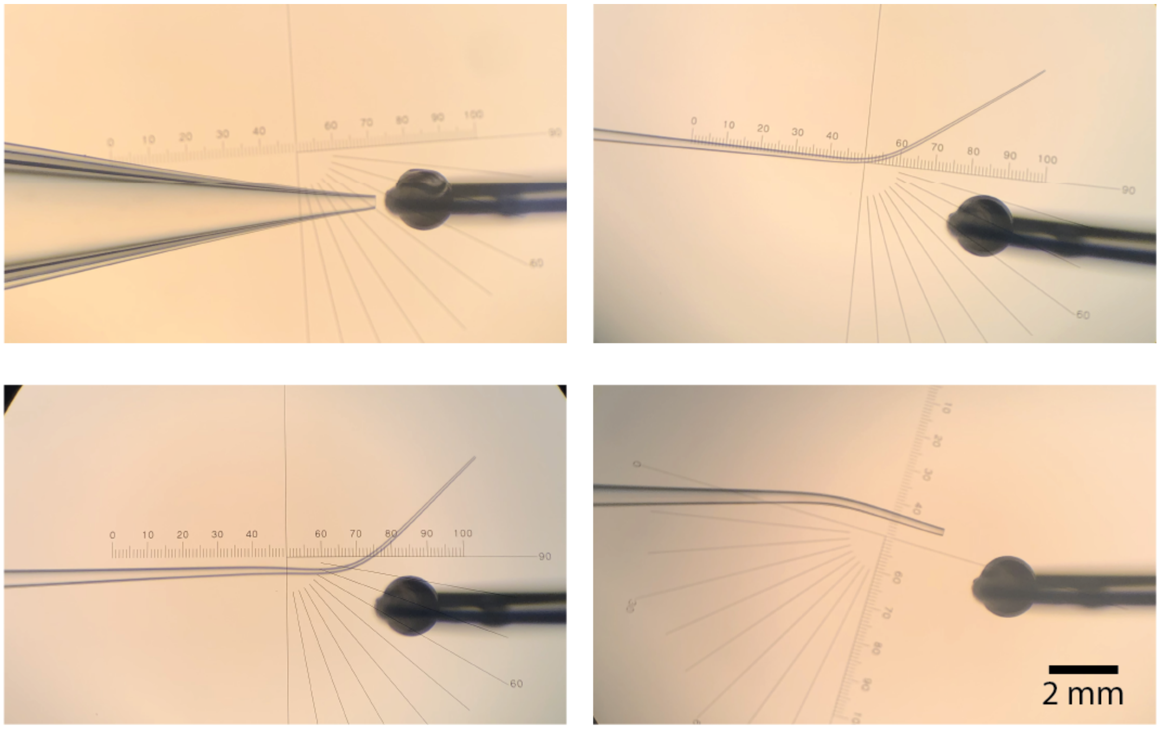

Figure 3-2: Images of microforged micropipettes, as viewed from the microforge objective, demonstrating the wide range of confinement geometries that can be attained. The heating element of the microforge, a glass ball attached to a metal wire with variable current, can be seen on the right hand side of the images.

and steeper taper.[1]

In order to create an opening at a specific location along the micropipette or to introduce more complex geometrical elements such as bends or spikes, a microforge must be used. Equipped with an objective and a controllable heating element, this instrument allows for visual microworking of glass capillaries by melting the glass at desired locations via the application of heat. Combining micropipette pulling with microforging, a variety of complex boundary conditions, such as cylindrical, conical, bent, and curved confinement geometries, can be attained.

---

[1] For a detailed set of instructions for how to pull micropipettes, Sutter Instrument Company's Pipette Cookbook written by Adair Oesterle is an excellent source. The document is updated every two to three years and can be found online. Many of the newer micropipette puller models, such as Sutter Instrument Company P-1000, are also equipped with the cookbook.

3.4 Live fluorescence imaging of biochemical patterns inside a micropipette

The assessment of mechanical properties of cells or tissues using micropipette aspiration, such as those mentioned in the previous section, is made possible by tracking the location of the oocyte tip inside the micropipette. This utilizes the property of optical transparency of glass capillaries. Researchers often use brightfield optical microscopy in order to accurately track the cell movement, and at times monochromatic light, in order to attain higher location accuracy.

On the other hand, combining fluorescence imaging with micropipette aspiration in order to probe mechanoresponsive behaviors of proteins has not been fully explored. Existing studies have only focused on simple behaviors such as mechanosensitive accumulation or depletion of signaling proteins or cytoskeletal elements [42]. Furthermore, to our knowledge, the evolution of *in vivo* reaction-diffusion protein patterns during micropipette aspiration has not been investigated prior to this study.

We use fluorescently tagged spatiotemporal RhoA patterns on the *Patiria miniata* sea star oocyte membrane as a model system for exploring the behavior of such biochemical patterns under time dependent boundary conditions. In order to accurately track these protein patterns inside the micropipette, the aspiration set up must be altered and adapted to effectively interface with a fluorescent microscopy system.

Though the fluorescent patterns appear on the surface of the oocyte, there is significant undesired background fluorescence arising from the cytoplasm. In order to minimize this contribution, a confocal fluorescence microscope is utilized. While the signal-to-noise ratio can be increased and high spatial resolution can be attained via this method, temporal resolution may suffer. This arises from the background fluorescence blocking mechanisms of confocal microscopes. They do so by utilizing one (scanning) or a set of (spinning-disk) small spatial pinholes which reject light emanating from objects outside the focal point. While this increases contrast, it also necessitates multiple images to be taken at different depths to capture the entire cell surface. Thus, it is crucial for the micropipette to be oriented perfectly parallel to the

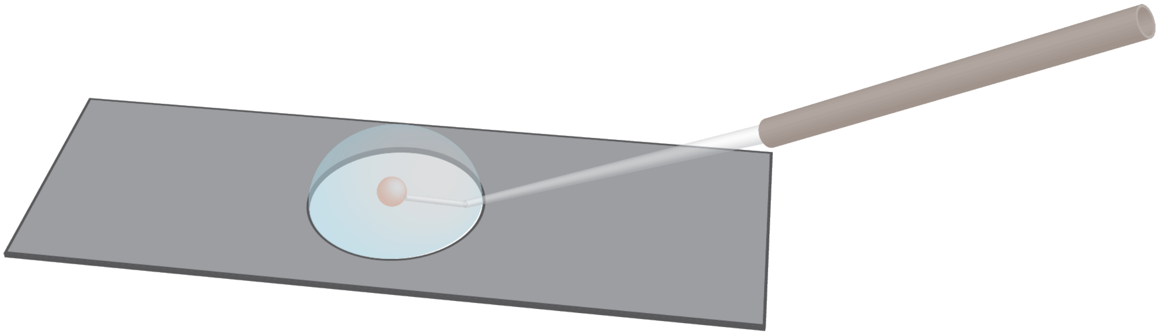

Figure 3-3: A close up schematic of oocyte aspiration fluorescence imaging set up. A metal slide the size of a regular glass microscopy slide with a hole in the middle is used as the sample holder. A cover slip is attached to the bottom using wax. The oocytes in seawater are placed on top of this cover slip and covered with oil to prevent evaporation. A micropipette filled with seawater and attached to a pump is inserted into the seawater and brought to close proximity of the oocytes. By lowering the pressure inside the micropipette, the oocytes are pulled in and partially aspirated.

imaging plane to minimize the number of images and maximize temporal resolution.

To this end, the sample holder was picked to have the most shallow edges possible. We used a metal slide with dimensions identical to that of a regular glass microscopy slide. A hole in the middle of the slide allowed for a cover slip to be attached and sealed via candle wax or VALAP, a mixture of vaseline, lanolin, and paraffin wax. This allowed for an optically transparent window to be created on the slide. The oocytes in filtered seawater were placed on this window, and covered with oil to prevent evaporation.

This set up still proved difficult to attain high frame rate images due to the edge height and glass capillary size at the base (1mm), so a bend of around 20^o was introduced to the micropipettes at around 3mm distance from the opening using a microforge. This bend did not affect the region of interest for imaging purposes, but allowed for optimal temporal resolution as the imaged portion of the micropipette was able to perfectly lie along the imaging plane. The vertical alignment of the micropipette orientation was performed visually. A schematic diagram of this set up is shown in Figure 3-3.

Using the method above, a total exposure time of 15 seconds was attained, around a three-fold improvement when compared to using straight micropipette needles.

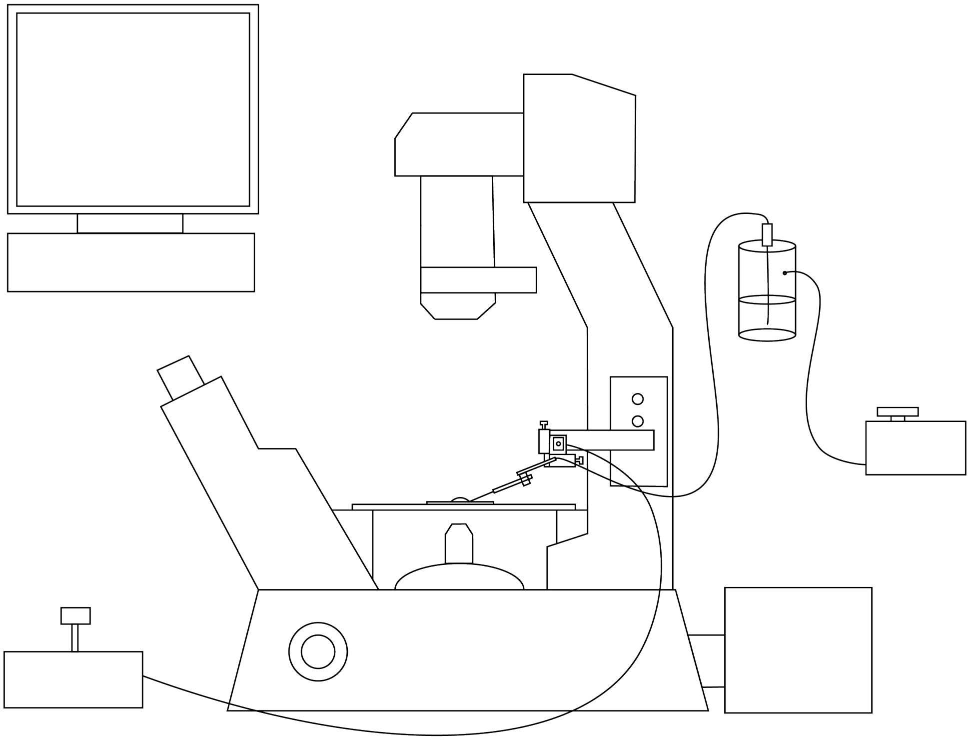

Figure 3-4: Schematic drawing of the aspiration set up on a confocal microscope. The oocytes in filtered seawater are placed on a slide located on the microscope stage, and covered with oil to minimize evaporation. Using an XYZ micromanipulator attached to the microscope body, a micropipette is inserted into the chamber. The pressure inside the micropipette is lowered by a pump and a pressure controller, pulling the oocytes into the glass capillary. The fluorescent protein patterns are imaged in real time through confocal microscopy.

Since unperturbed oocytes exhibit RhoA patterns with periodicity of around 100 seconds, this frame rate provided sufficient temporal resolution for capturing the dynamics of the protein patterns. As the unaspirated portion of the oocyte membrane spanned a different range of depths, only the part inside the micropipette was imaged.

Finally the oocyte aspiration setup was integrated into a confocal microscope body via the appropriate connector and a micromanipulator capable of motion in three orthogonal directions (Figure 3-4). The attachment of the system to the microscope frame not only allowed for the precise positioning of the micropipette relative to the

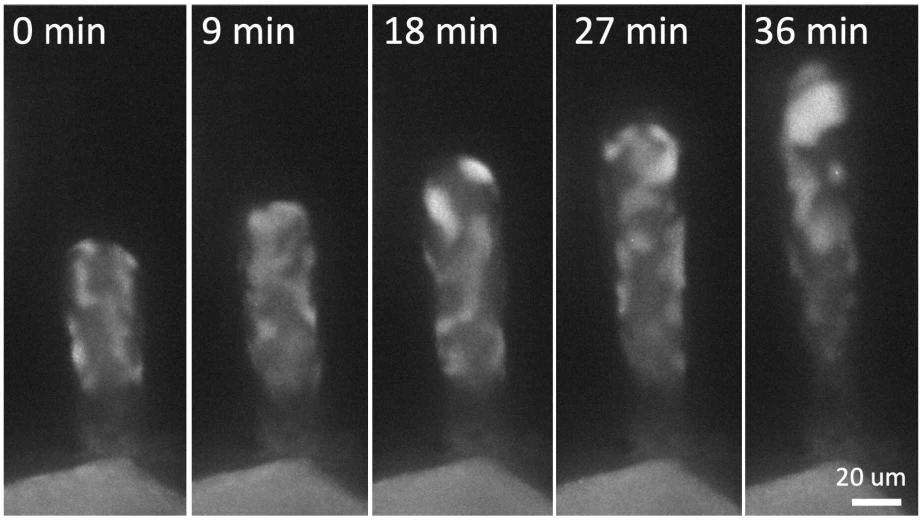

Figure 3-5: The evolution of the spiral Rho patterns inside the micropipette for a partially aspirated oocyte. The micropipette opening is located towards the bottom of the images, where the unaspirated part of the oocyte can be seen. With time, the oocyte flows inside the micropipette, moving upwards and away from the opening.

objective, but also minimized vibrations and drift. The oocytes expressing steady-state RhoA spatiotemporal patterns were imaged on this micropipette integrated confocal imaging system around two hours post maturation.

Experiments were carried out using cylindrical micropipette geometries with diameters ranging from 20 to 80 μm. The motion of the oocyte inside the micropipette was kept nearly static, with $L(t)$, the length of the oocyte along the micropipette at a given time t, changing much more slowly when compared to the evolution of the RhoA patterns.

3.5 Results and discussion

3.5.1 Spiral wave front alignment with the pipette long axis

RhoA spiral waves were observed to undergo significant alterations inside the micropipette. These biochemical patterns, which display turbulent spirals with chaotically interacting waves on the unperturbed surface of the oocyte (Figure 2-1), transformed into lines along the micropipette's long axis that move coherently in the radial

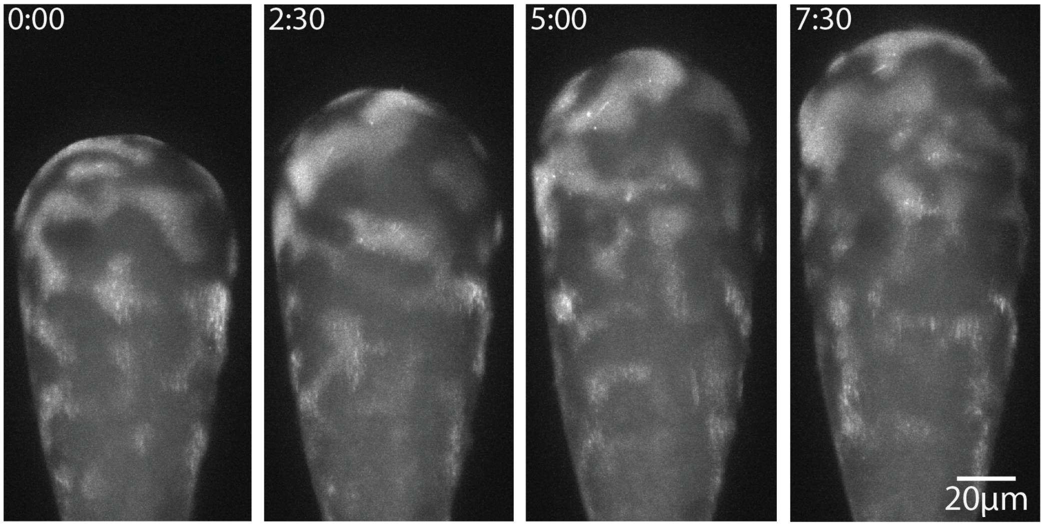

Figure 3-6: Fluorescence images of spiral RhoA patterns on a partially aspirated *Patiria miniata* oocyte membrane inside a micropipette 60 μm in diameter. The time stamps are presented in mm:ss format.

direction with well-defined sizes and spacings. Such behavior is shown in Figure 3-7a, where the patterns become increasingly ordered over time, and the emergence of spatial correlation can be seen (Figure 3-7b and c).

This type of pattern transformation was often detected in regions closer to the opening of the micropipette. Aspirated oocytes were also observed to exhibit a mixture of behaviors, for example in the experiment shown in Figure 3-6, where the patterns towards the bottom of the images (closer to the pipette opening) are linearly arranged, with the wave fronts parallel to the short axis of the micropipette, and those at the top (further from the pipette opening) of the image are more turbulent, similar to those seen on an unperturbed oocyte surface.

Such pattern dependence on geometrical conditions has been observed in the phyllotactic patterns mediated by the phytohormone auxin in the shoot apical meristem (SAM) of plants. In order to reproduce the patterns, Rueda et al. developed a model in which the hormone concentration was coupled to the geometry of an evolving domain by both inducing stress as well as being guided by it [54]. The authors utilized geometries what were cylindrical, with a dome-like tip, similar to a hemisphere. Depending on the geometry as well as the hormone concentration, the emergence of a

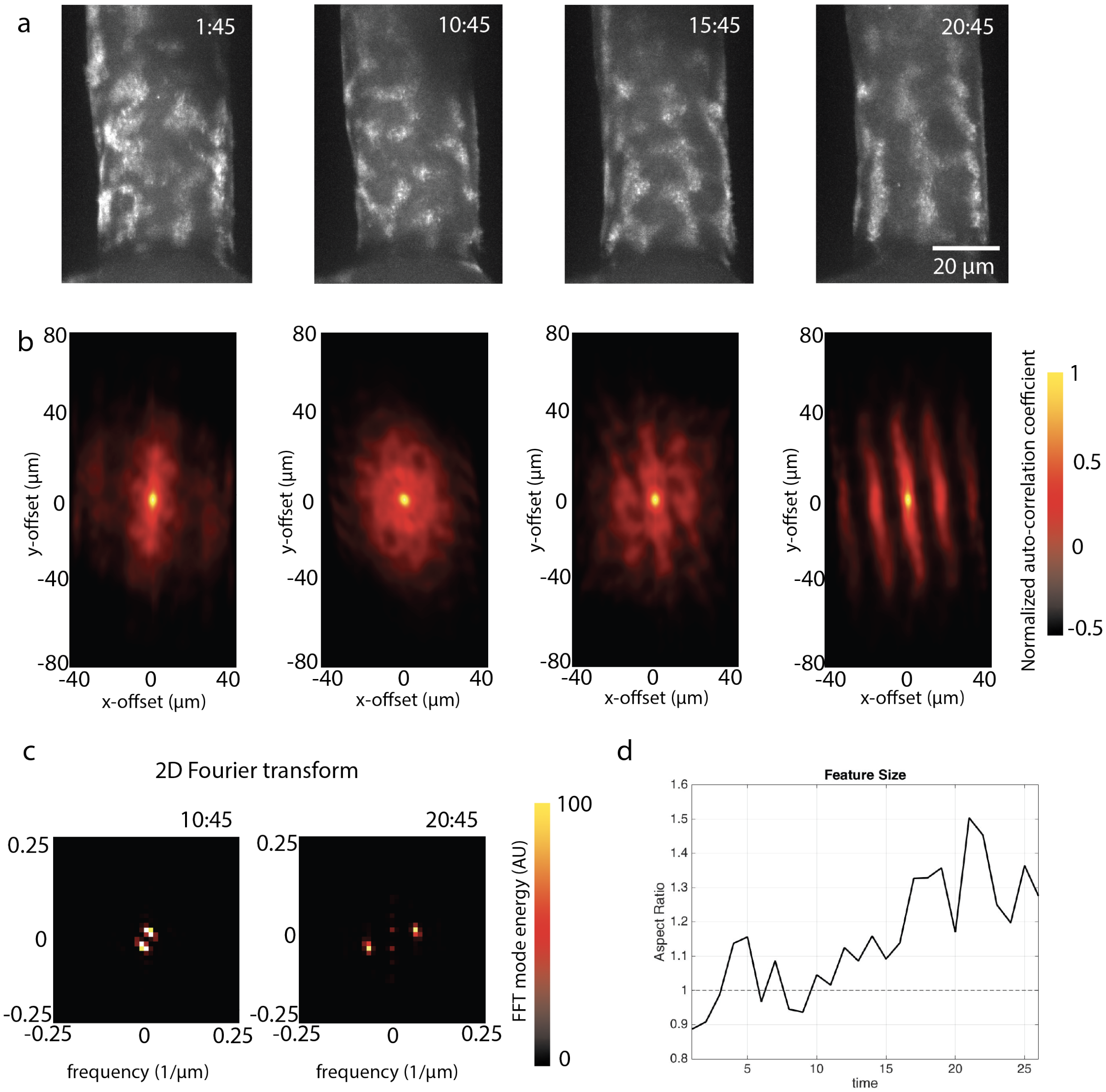

Figure 3-7: **a** Close up images of Rho activity patterns inside the micropipette displaying emergence of longitudinal spiral wave front alignment. **b** Normalized spatial auto-correlation of the images in panel a. **c** 2D Fourier transform of two images from earlier and later times, respectively. **d** Aspect ratio of patterns in time (min). Time stamps are denoted in mm:ss format.

multitude of patterns, such as spiral, ribbed, and spot, were observed. These patterns displayed differing structures depending on their location relative to the tip. The dependence of the patterns on the overall micropipette geometry and spatial positioning along it may suggest a similar curvature or stress sensitivity of the reaction-diffusion patterns of Rho. Such behavior can be further explored via the incorporation of local membrane tension measurements and the observation of pattern response to dynamic change of curvature.

3.5.2 Spatially and temporally varying pattern frequency and fluorescence intensity

Plotting the Rho activity patterns of Figure 3-5 along the micropipette yields the 2D space-time kymograph shown in Figure 3-8a. This representation reveals the length dependent frequency behavior of the Rho patterns: the oscillation period grows as a function of the distance away from the micropipette opening. This observation is confirmed via the Fourier transform of the signal (Figure 3-8b), where the pattern oscillation frequency at the leading tip of the oocyte inside the micropipette (around 15/hr) is revealed to be around half of that of the patterns in the vicinity of the pipette mouth (around 30/hr).

While such spatial variation in pattern frequency is intriguing, this analysis omits possible temporal variation. In order to uncover the spatially resolved time-frequency properties of the pattern oscillations, Fourier synchrosqueezed transformation (FSST) is performed. The oscillatory signal $f(t)$ at any given point in space can be expressed by

$$f(t) = \sum_k f_k(t) = \sum_k A_k(t) e^{i\phi_k(t)},$$

where $A_k(t)$ denotes a slowly varying amplitude in time, and $\phi_k(t)$ represents the oscillatory phase. Thus, $d\phi_k(t)/dt$ corresponds to the instantaneous frequency. Fourier transform of this signal $f(t)$ convolved with a window function $v(t-\tau)$, for example a Gaussian or Kaiser-Bessel function, centered at the time point of interest

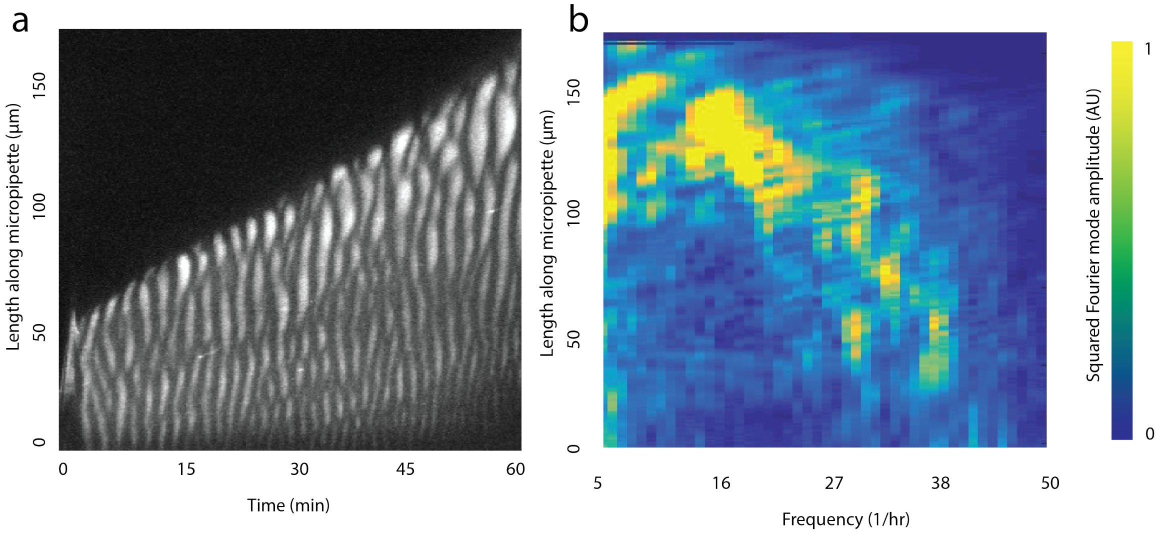

Figure 3-8: **a** Space-time kymograph of Rho activity patterns along a micropipette for the experiment shown in Figure 3-5 and **b** its Fourier transform along the temporal axis, showing a varying pattern frequency along the micropipette.

τ, reveals the time resolved frequency spectrum of any given point. Called the short time Fourier transform (STFT), this mathematical transform can be expressed as

$$\tilde{F}(\tau, \omega) = \int_{\infty}^{\infty} f(t)v(t-\tau)e^{i\omega(t-\tau)}dt.$$

By sliding the window function in time, the spectrogram, which denotes the 2D amplitudes of frequencies as a function of time, can be obtained. The transform values can subsequently be "squeezed" such that they are amplified around instantaneous frequency curves. The dominant frequency of any spatial point can then be calculated by picking the frequency with the highest mode amplitude from its spectrogram (Figure 3-9).

Such an analysis can be performed for the points along the micropipette. Yet, it is imparative to disassociate the pattern dynamics from the aspiration motion. This disentanglement is performed via a change in reference frame, from the lab frame, where the micropipette is stationary, to that where the leading tip of the oocyte inside micropipette is static (Figure 3-9a). As the cell is continually aspirated, the domain grows, and the individual points inside the region of interest can be referenced as a function of their distance to the oocyte tip. The areas outside the aspirated oocyte are

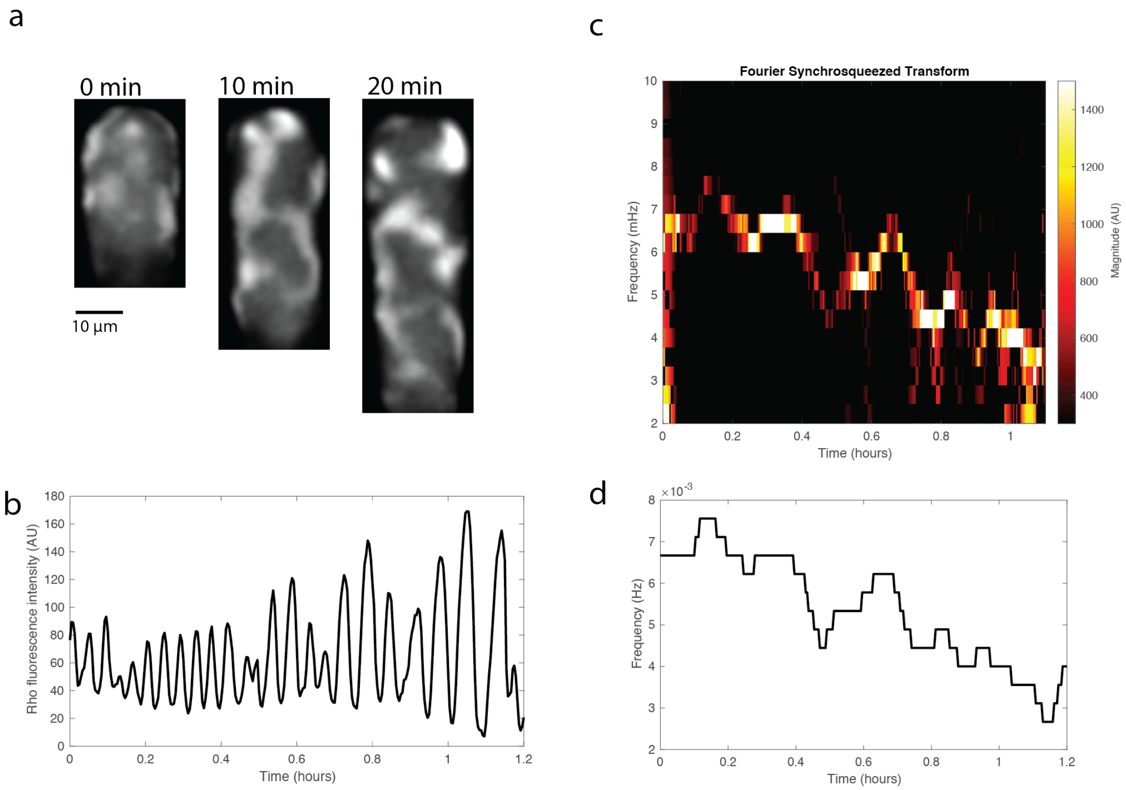

Figure 3-9: Extraction of instantaneous frequencies of Rho patterns along the micropipette via Fourier synchrosqueezed transform. **a** The frame of reference is shifted such that the tip of the oocyte is static. **b** Time series of Rho patterns are extracted from each pixel. **c** Time-frequency spectrogram is attained for each pixel. **d** Instantaneous frequencies are extracted by selecting the frequency with the maximum magnitude in the spectrogram at each time point.

identified by setting an intensity threshold, and marked with ’NaN’ (not a number) intensity and 0 Hz frequency.

When averaged along the short axis, the pattern frequency of the points inside the micropipette, identified by FSST, revealed a gradient of frequencies along the pipette. The frequencies increased with distance away from the oocyte tip (Figure 3-10), consistent with the simple Fourier transform of the intensity kymograph (Figure 3-8). This gradient was seen in small as well as large micropipette diameters, such as in the case of the experiment shown in Figure 3-6. The frequencies along the micropipette for this experiment are shown in Figure 3-12. Furthermore, the frequency of every point along the micropipette was also observed to decay with time, regardless of its position relative to the oocyte tip. This decay appeared to be uniform in space.

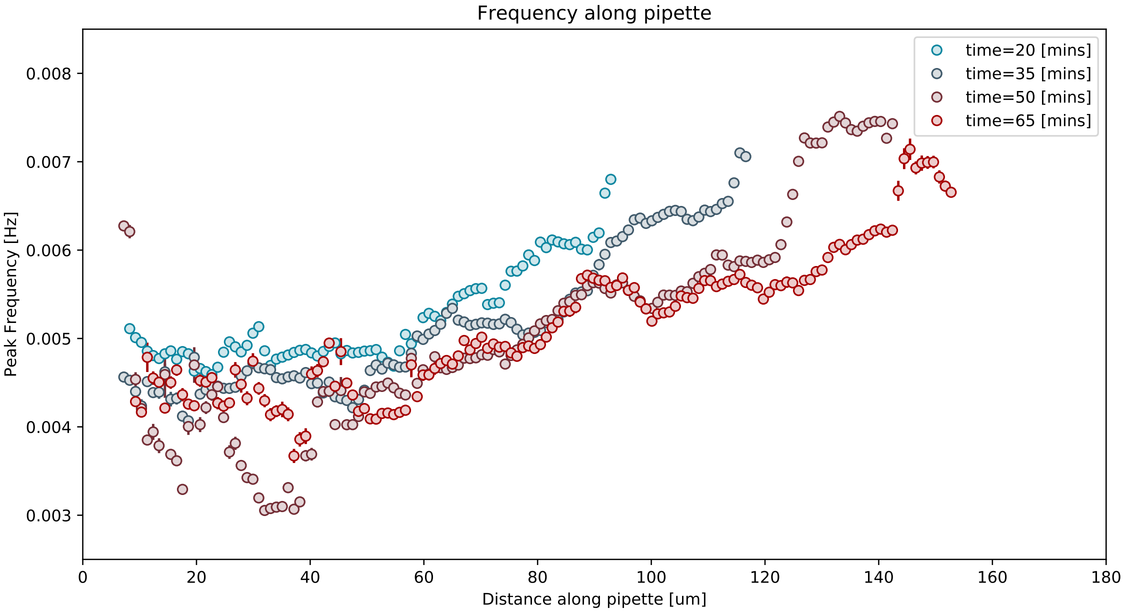

Figure 3-10: Pattern frequencies as a function of distance away from the aspirated tip along a micropipette 20 μm in diameter manifest as a gradient increasing with distance. These frequencies also exhibit time-dependent, spatially uniform decay.

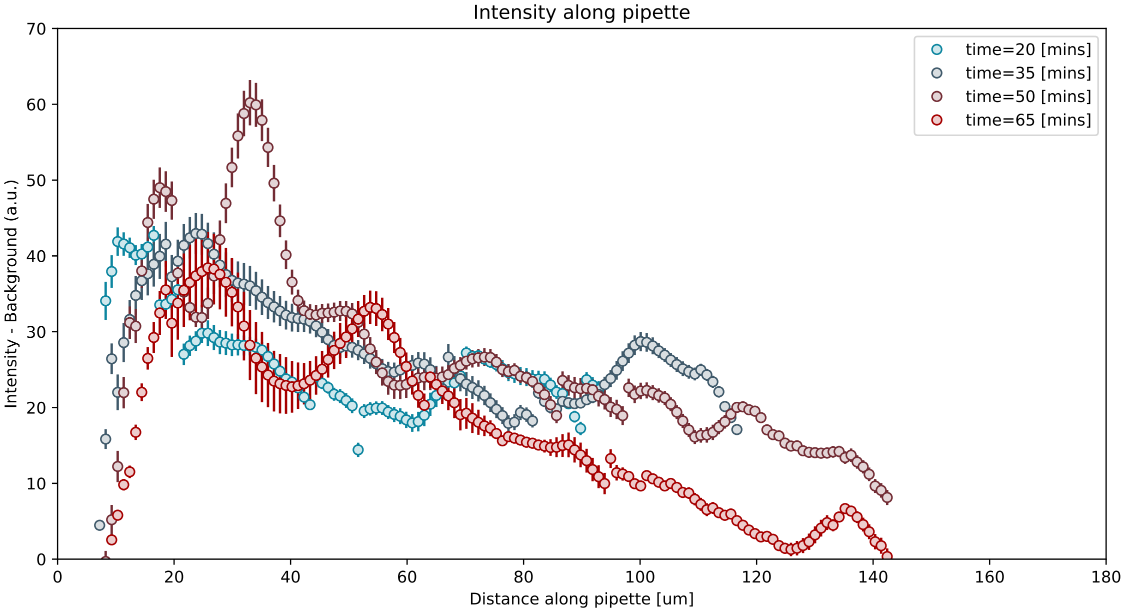

Figure 3-11: Average pattern intensity as a function of distance away from the aspirated tip along a micropipette 20 μm in diameter manifest as a gradient decreasing with distance.

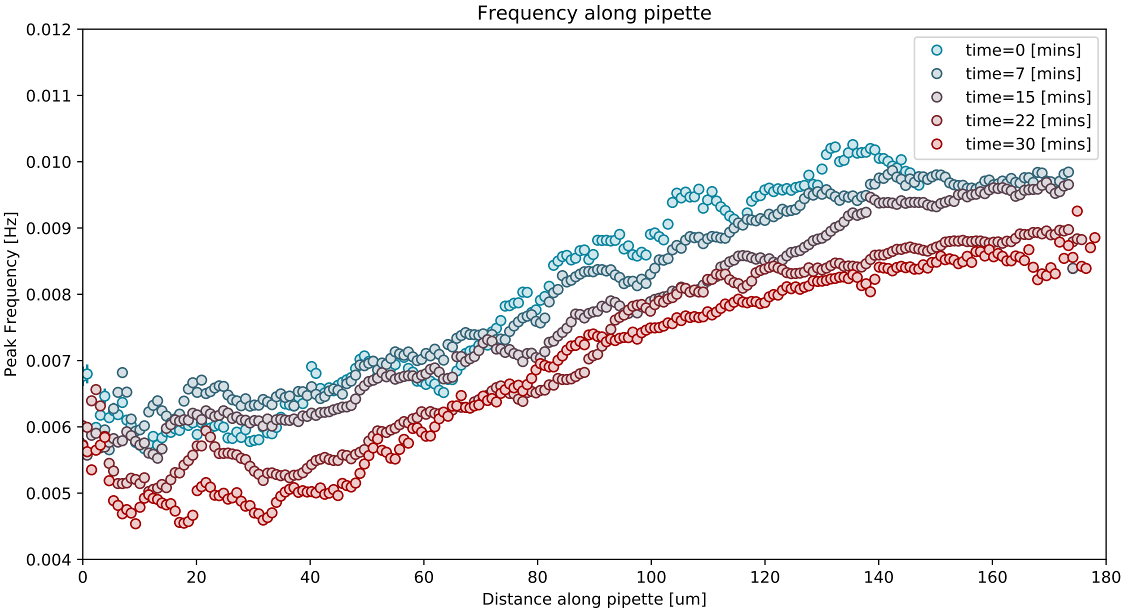

Figure 3-12: Pattern frequencies as a function of distance away from the aspirated tip along a micropipette 60 μm in diameter manifest as a gradient increasing with distance, similar to that of Figure 3-10.

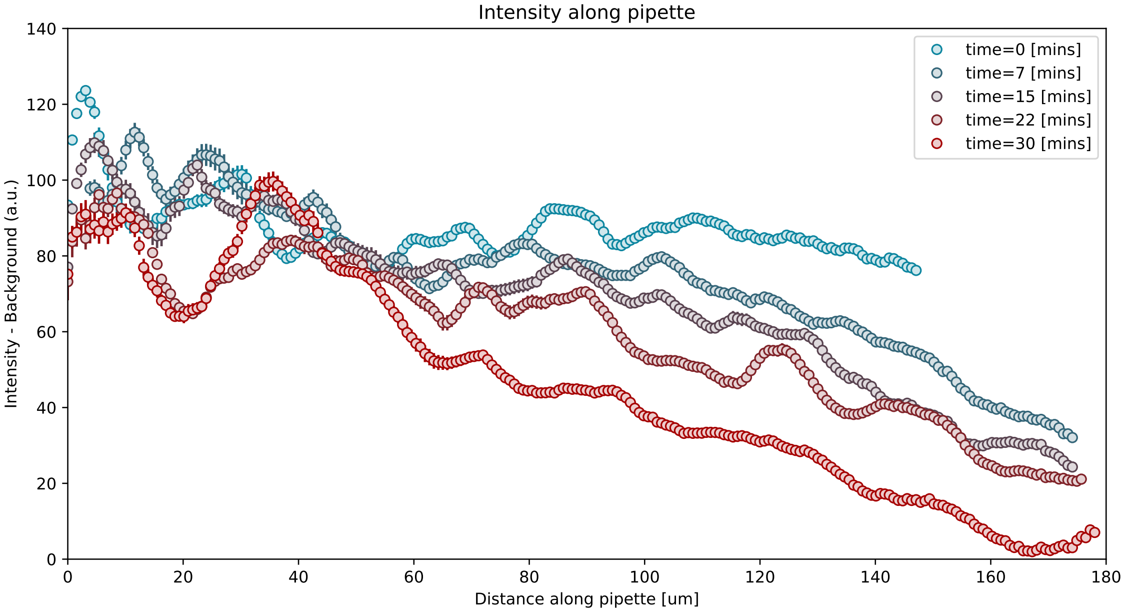

Figure 3-13: Pattern frequencies as a function of distance away from the aspirated tip along a micropipette 60 μm in diameter manifest as a gradient increasing with distance, similar to that of Figure 3-11.

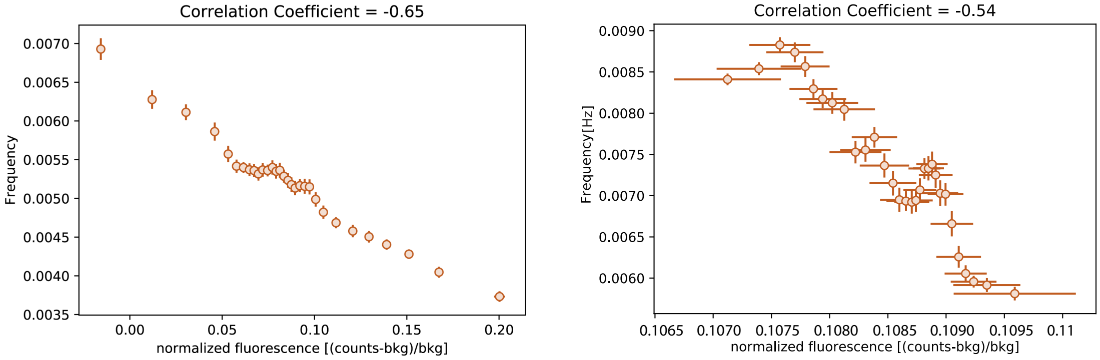

Figure 3-14: Profile plots of Rho activity pattern frequency vs. fluorescence intensity along two micropipettes of differing widths: 20 μm, experiment shown in Figure 3-5 (left) and 60 μm, experiment shown in Figure 3-6 (right). Strong anti-correlation is observed between the two variables.

The average fluorescence intensity of Rho activity patterns also manifested as a gradient along the micropipette. In contrast to pattern frequency, the intensity profile displayed a negative slope (Figures 3-11 and 3-13), with fluorescence decreasing as a function of increasing distance away from the oocyte tip. Again, only the area inside the micropipette was considered, and pixels lying outside of the micropipette were removed from this calculation.

The profile plot of pattern frequency and intensity (Figure 3-14), which describes the relative behavior of the two variables of interest, revealed strong anti-correlation between the two fields. This behavior is consistent with the Rho pattern properties during the initiation of such waves, which corresponds to the meiotic contraction wave (Figure 1-3). Unlike the steady-state patterns covered in this thesis, during meiosis, Rho patterns exhibit time-dependent oscillation frequencies (Figure 3-15). A hierarchical ordering of protein patterns working upstream of Rho enable this cellular process. Specifically, a moving GEF front, set up by a decaying gradient of Cdk1-cyclinB, a cell cycle regulator, enables the formation of the traveling Rho wave in wild-type oocytes [67]. In GEF (Ect2) overexpressing oocytes, this Rho wave gives way to a spiral front. In time, the spatial GEF variation vanishes, and the concentration of the biochemical becomes homogeneously distributed throughout the oocyte. This is when the steady-state spiral Rho patterns are observed in oocytes overexpressing GEF.

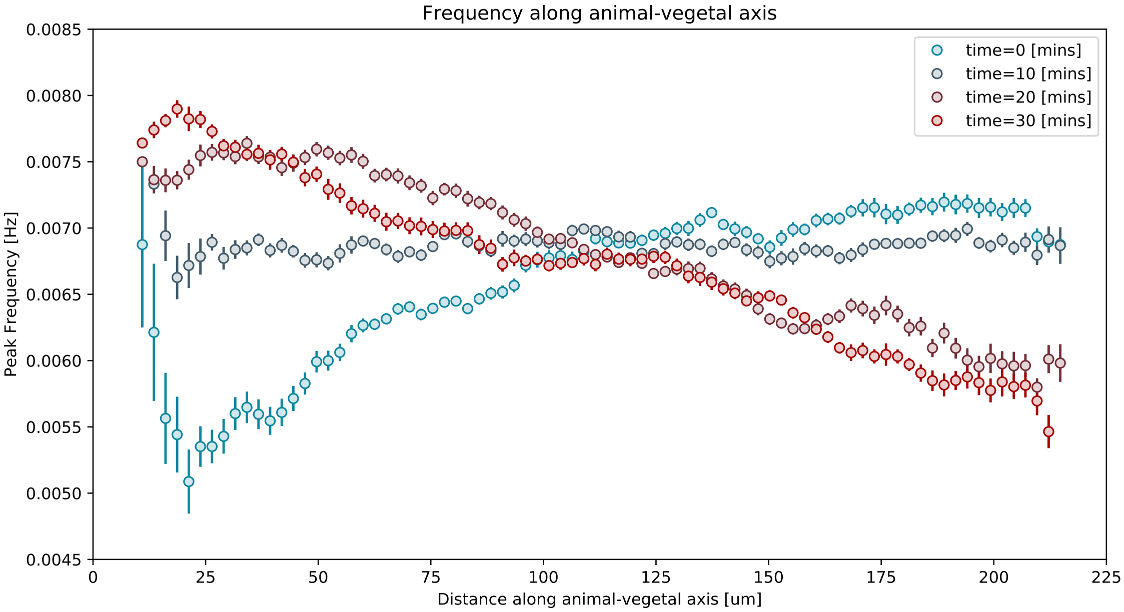

Figure 3-15: Rho oscillation frequency along the animal-vegetal axis of a GEF overexpressing oocyte during meiosis.

In their 2020 Cell Reports article, Kamps et al. [37] investigated the relationship between oscillatory RhoA dynamics and GEF-H1, which is one of at least three RhoGEFs present in the sea star oocyte alongside Ect2 and MyoGEF [6]. By optogenetic tuning of GEF-H1, the authors could control GEF-H1 concentration, and alter RhoA activity. Similar to the experimental system described in this thesis, the authors used a fluorescently tagged GBD, which bound only to active RhoA to track its dynamics. Including myosin concentration as an additional variable, the authors modeled the biochemical reaction scheme as set of three coupled ordinary differential equations:

$$\frac{dR}{dt} = \frac{k_1 G(R_T - R)}{K_{m1} + R_T - R} - \frac{k_2 R}{K_{m2} + R},$$

$$\frac{dG}{dt} = k_3(G_T - G)R - k_4 GM,$$

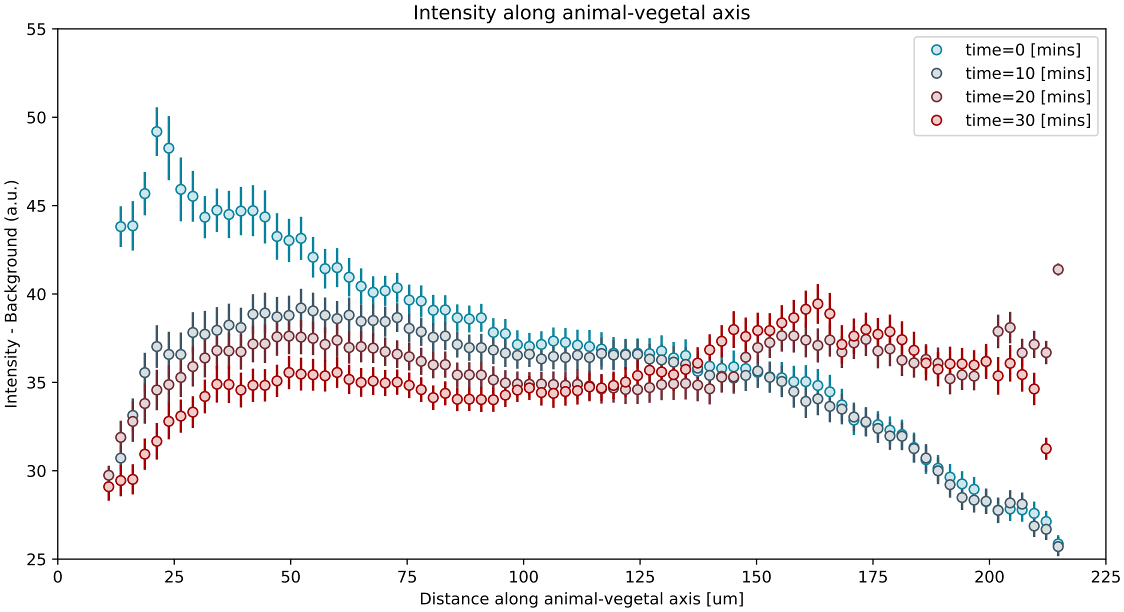

Figure 3-16: Rho fluorescence intensity along the animal-vegetal axis of a GEF overexpressing oocyte during meiosis.

$$\frac{dM}{dt} = \frac{k_5 R(M_T - M)}{K_{m5} + M_T - M} - \frac{k_6 M}{K_{m6} + M},$$

where $R(t), G(t)$, and $M(t)$ denote active and membrane associated RhoA, GEF-H2, and myosin, R_T, G_T, and M_T represent the total concentrations of these components, and k_{1-6} and K_{m1-6} are rate and Michaelis constants. In this model, oscillatory Rho activity patterns were observed for a range of GEF concentrations, and the findings were experimentally confirmed. As these biochemicals are highly conserved throughout the metazoa, their reaction dynamics are expected to be similar across different species.

Using this model, I plotted the Rho peak intensity and oscillation frequency as a function of GEF-H1 concentration. As shown in Figure 3-17, with increasing GEF concentration, Rho intensity was found to increase, and frequency decrease, resulting in anti-correlation between the two observables. This result is consistent with Rho activity during the meiotic contraction wave in GEF overexpressing oocytes, as well as with Rho patterns inside the micropipette. In the latter case, a GEF accumulation inside the aspirated region would be expected, establishing a gradient along the

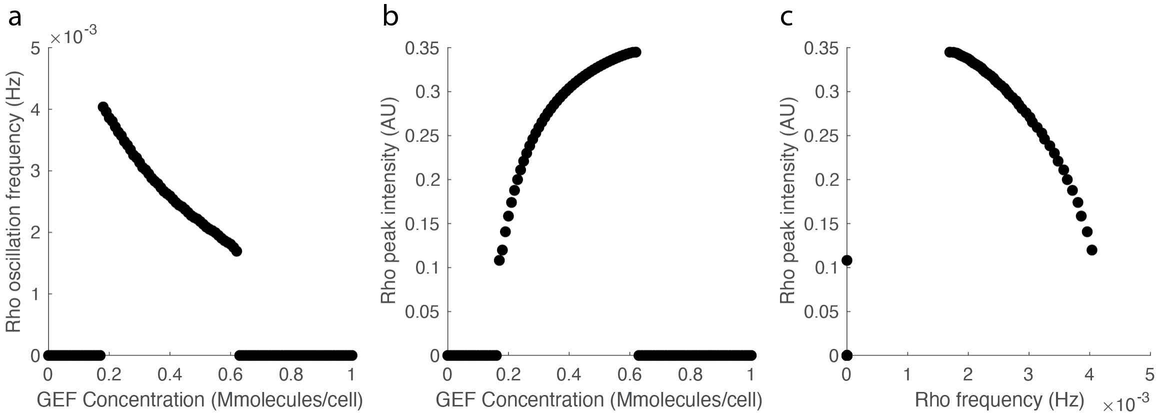

Figure 3-17: **a** Rho oscillation frequency and **b** amplitude as a function of GEF concentration, and **c** the relationship between these two variables, using the model outlined in Kamps et al. 2020. [37].

longitudinal axis of the micropipette, leading to an increasing (decreasing) gradient of frequency (Rho intensity). As GEF continues to accumulate, the frequencies along this axis would continually decay, and Rho intensity would increase. While the former is clearly observed in the experiments highlighted above (Figures 3-10 and 3-12), the latter is not. This might be due to photo bleaching of the fluorescent reporter, leading to a decrease in the overall fluorescence over time.

Many cytoskeletal components and associated biochemicals have been shown to exhibit mechanosensitive behavior, leading to protein accumulation inside the aspirated cortex of cells [42]. Such mechanosensitive behavior was found to generally serve to counteract external forces by increasing local contractility. As GEF is the activator protein for Rho, which induces contractile behavior in the actomyosin cortex, GEF accumulation inside the micropipette could serve as a way for the cell to resist the imposed mechanical deformations and locally activate its contractile machinery. This increase of protein concentration inside the micropipette can be explored via the fluorescence imaging of GEF.

In summary, by combining confocal fluorescence imaging with micropipette aspiration, dynamic geometrical deformations were induced on *Patiria miniata* oocytes expressing spiral Rho activity. Exhibiting steady-state dynamics in unperturbed oocytes, these patterns were altered inside the micropipette. Gradients of Rho frequency and intensity were established along the longitudinal axis, and an anti-correlation between these two properties was observed. These dynamics were consistent with a GEF gradient being established inside the pipette.

3.6 Future work and outlook

3.6.1 The effect of micropipette shape and the dynamics of geometrical confinement

In this work, aspiration speeds were kept low in comparison to pattern dynamics. Such a setup allowed for the Rho activity patterns to experience pipette geometries that were quasi-static. Using a digital pressure controller, it is possible to apply a range of driving forces to the oocyte to explore highly dynamic geometries. Inducing oscillatory and high-speed deformations would be of particular interest, as such experiments would shed light on the effects of highly non-static geometries as well as the effects of varying cortical stress on pattern dynamics. In order to observe the process with which Rho patterns relax to steady-state after a geometrical perturbation, high speed aspiration can be performed, followed by a stationary period during which the patterns are imaged with a high frame rate. Such experiments will help uncover the mechanisms underlying pattern formation and evolution during geometrically dynamic cellular processes.

Micropipettes used in this work ranged from 20 to 60 μm in diameter, multiple times the Rho pattern size. Even in these geometries, strong directional alignment of patterns was observed, suggesting that the patterns might be able to sense the local micropipette geometry. Decreasing micropipette diameter to lengths comparable to the Rho pattern size would add an additional constraint on the patterns: in the azimuthal direction, the patterns would experience periodic boundary conditions with a very small domain size, where the wave front would 'chase' the tail, interacting with it. As the distance along the longitudinal direction would be significantly longer, this asymmetry could force both pattern shape and motion to change. Furthermore, in

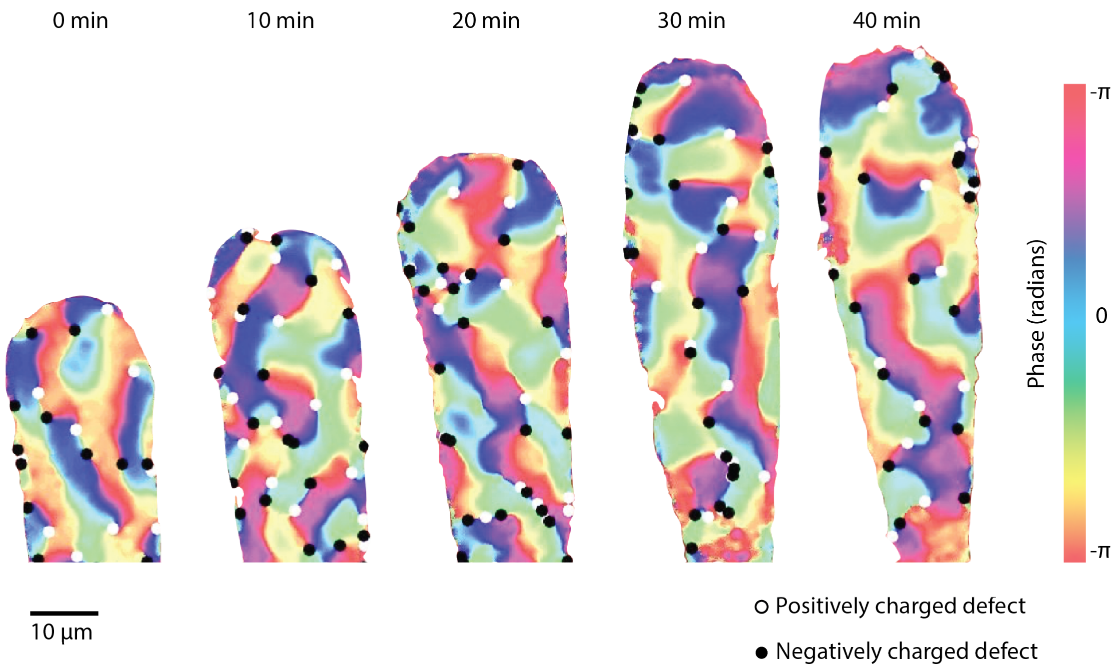

Figure 3-18: Snap shots of the phase field of Rho patterns as acquired by the Hilbert transform and its associated topological defects along the micropipette from the experiment shown in Figure 3-5.

such small geometries, coupling through bulk depletion might also be observed.

3.6.2 Spiral core distribution and motion on curved surfaces

Since Rho fluorescence patterns are oscillatory in time, they can alternatively be expressed by only their phase $\phi(t)$, removing the time varying amplitude $A(t)$. This representation can be accomplished by taking the Hilbert transform of each point in time, and constructing the phase field $\phi(x, y, t)$ (Figure 3-18). The phase fields of these spiral Rho patters smoothly vary throughout space, except for at certain point-discontinuities. These topological point defects in the phase field correspond to the spiral core locations, with positively (negatively) charged defects corresponding to counter-clockwise (clockwise) rotating spirals.

Since the distribution of the spiral cores and their motion dictate the entire pattern and its evolution, the dynamics of these defects are of particular interest in understanding the behavior of Rho patterns in dynamically evolving domains with

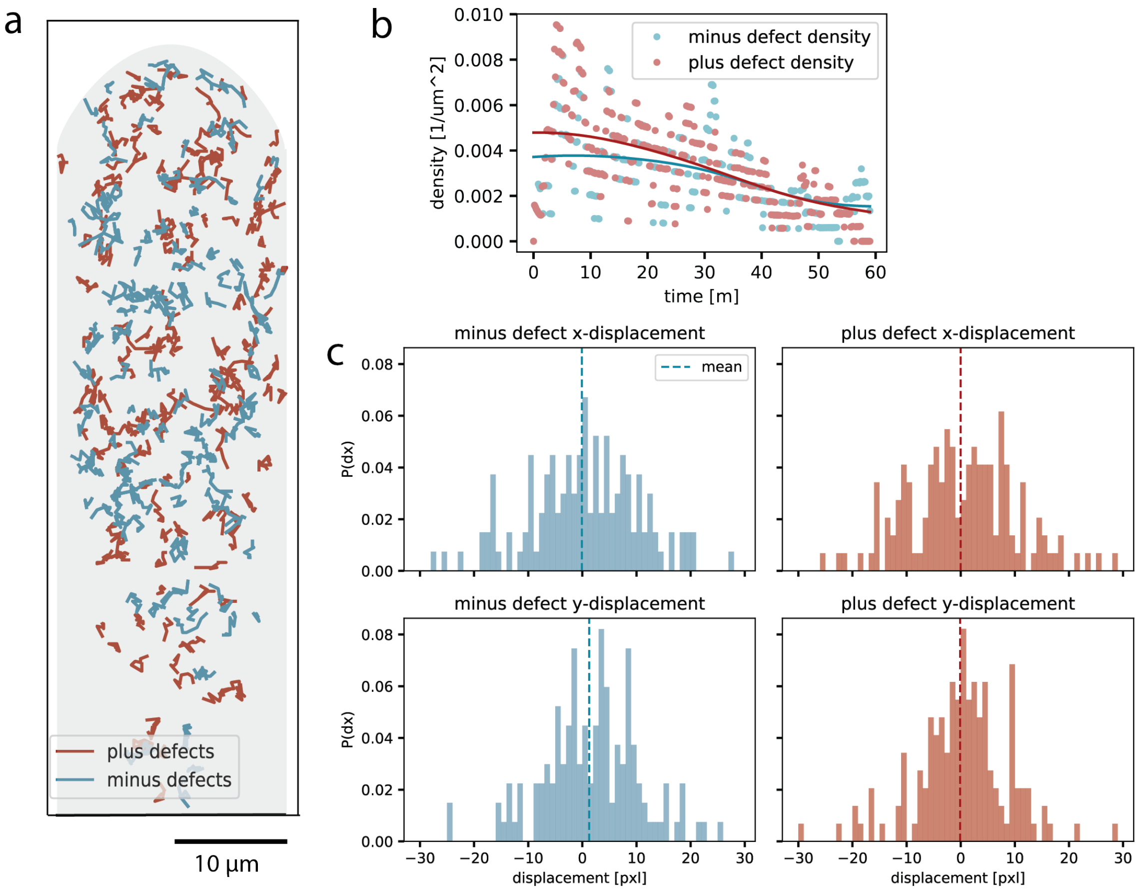

Figure 3-19: Topological defect **a** trajectories, **b** densities, and **c** displacement statistics inside the micropipette shown in Figure 3-5. Defects of opposite charges (plus and minus) are observed with the same frequency, and their densities are found to decay over time. No preferred directional movement is observed.

curvature. The observation of ordered, linear patterns inside the micropipette points to geometrically, or more specifically curvature, dependent spatial arrangement and defect-defect interactions. Such ordered spatial distribution of defects is especially clear in the left-most image in Figure 3-18, where oppositely charged defects seem to largely be paired in the longitudinal direction, creating the vertical Rho activity stripes.

Preliminary data shown in Figure 3-19 points to the positively and negatively charged defects occurring with equal rates, and their displacements not favoring any particular horizontal or vertical direction. Over time, a decrease in defect density for both charges (Figure 3-19b) is observed, consistent with an increase in pattern oscillation period and size. Yet, further work is necessary to uncover whether curvature plays a role in such spatial distribution and motion. Such a study would extend the defect-defect interaction dynamics explored in *Tan, et al. 2020* [60] to include surface curvature and evolving domain boundaries.

3.7 Materials and methods

3.7.1 Oocyte preparation

The wild isolate *Patiria miniata* sea stars were procured from South Coast Bio-Marine and kept in a salt water fish tank with 35 ppt salinity at a temperature of 15^oC (59^oF). The extraction of oocytes was made through an incision of around 1 cm applied to the bottom side of the sea star. The extracted ovaries were placed in a beaker with calcium-free seawater with 35 ppt salinity to prevent maturation. The ovaries were repeatedly lacerated with scissors to release the oocytes. After the oocytes were washed twice in calcium-free seawater to remove ovary tissue, they were incubated at 15^oC in filtered seawater for up to three days.

When maturation of oocytes arrested at prophase of meiosis I was desired, 1μM 1-methyladenine (1-MA) was added to a 1mL tube of saltwater solution containing 50μL of oocytes. Germinal vesicle breakdown of cells was observed at about 30 minutes post 1-MA addition. Experiments were carried out starting two hours after the initiation of maturation.

3.7.2 mRNA synthesis and oocyte microinjection

A fluorescent RhoA reporter and a Rho-GEF mRNA construct was used in this study. eGFP-rGBD, a fluorescently labelled rhotekin binding domain construct, was used as the RhoA reporter. The construct was deposited to Addgene by William Bement and purchased by the Fakhri Lab from the company. Ect2-T808A-mCherry was used for the Rho-GEF construct. A gift from George von Dassow, this Ect2 mutant is not sensitive to a type of phosporylation by cyclin-dependent kinase 1 (Cdk1), a protein kinase and a cell cycle regulator.

The constructs were amplified by overnight growth of Ampicillin resistant bacterial culture in LB media at 37^{o}C. After lysing the bacteria, the plasmid was isolated using the Qiagen miniprep kit, and linearized through appropriate restriction enzyme digestion. The linearized plasmids were transcribed using the Thermo Fisher Scientific Invitrogen mMESSAGE mMACHINE SP6 Transcription Kit, and finally a poly(A) tail was added to the RNA transcripts with the Invitrogen Poly(A) Tailing Kit.

The *Patiria miniata* oocytes were microinjected with an mRNA mixture of eGPF-rGBD and Ect2-T808-mCherry and incubated at 15^{o}C for 24 hours to express the fluorescent proteins before imaging.[2]

3.7.3 Confocal imaging system

All imaging was done at the W.M. Keck Biological Imaging Facility located in the Whitehead Institute. The confocal images were acquired using the RPI spinning disk confocal microscope, which possesses a Zeiss AxioVert 200M inverted microscope frame and a Yokogawa CSU-22 spinning disk confocal scan head with Andor Borealis modification. A 488nm 150mW optically pumped semiconductor laser line light source was used to excite the fluorescent markers, and the GFP filter (525/50nm) was selected for the emission path. The Zeiss Plan NeoFluar 25X/0.8 multi immersion objective was picked for optimal spatial resolution and window size. Images were captured by a Hamamatsu Orca-ER cooled CCD camera via MetaMorph image acquisition software. Image slices were acquired with a total frame rate of 15 seconds, and maximum intensity projection was used to produce the final images.

3.7.4 Micropipettes

10cm long hollow borosilicate glass capillary tubes without filaments were bought from Sutter Instrument Company and and pulled using Sutter Instrument Company P-97 Micropipette Puller. The level of sharpness of the needles was controlled by

---

[2] The oocyte preparation, mRNA synthesis, and oocyte microinjection protocols are similar to those in Chapter 2 of this thesis.

changing the temperature and speed of pulling. Narishige MF-2 Microforge was used to forge the micropipettes. The micropipette tip was bent and its opening was created at this stage. The tip opening location was picked to achieve the desired micropipette geometry. This opening was fire polished by slight melting via the microforge in order to avoid rupturing the oocyte.

3.7.5 Micropipette aspiration and imaging set up

The forged micropipette was filled with 35 ppt salinity filtered seawater using a World Precision Instruments (WPI) MicroFil flexible needle, leaving an excess hemispherical droplet in its back end. The WPI PicoNozzle Kit v2 micropipette holder and its associated tube were filled with water, making sure not to have any bubbles trapped in it. An excess droplet was formed at the opening of the PicoNozzle and attached to the micropipette, droplet to droplet. The other end of the tube was connected to a P-CAP capped 2mL reservoir secured to a P-CAP reservoir stand. The pressure in the reservoir was provided by a 115V vacuum pump and modulated by a Flow EZ Module (0 to -69 mbar). The P-CAP, stand, pump, and pressure modulator were procured from Fluigent, Inc.

In order to attain precise manipulation of the micropipette tip location, the PicoNozzle micropipette holder was attached to a Narishige MM-94 XYZ motor-drive manipulator and controlled remotely by a joystick. To affix the system to the microscope, the XYZ manipulator was attached to the confocal microscope frame via the appropriate Narishige mounting adaptor.

3.7.6 Data analysis

The experimental images were corrected for spatial drift using Fiji (ImageJ) scientific image analysis software and cropped to remove areas away from the region of interest. These cropped images were uploaded to MATLAB, and and an intensity threshold was set, such that any pixel with intensity lower than the threshold was considered to be outside the micropipette, and their values changed to 'NaN' (not a number).

Since the regions without RhoA activity on the oocyte membrane still provided some amount of background fluorescence, but those outside the oocyte did not, the borders of the micropipette were able to be identified robustly.

To change the frame of reference to one with the stationary oocyte tip, the y-coordinate of the first pixel point as measured from the top of the image was identified, and the entire image was shifted up such that this pixel was placed at $y = 1$. The x values were left unchanged. This procedure was repeated for each time point.

The FSST analysis was performed on the time-series of each pixel using the MATLAB 'fsst' function, and convolved with a Keiser window of 80 frames in length (20 mins), and a shape factor $\beta = 40$ frames (10 mins), which corresponded to a full width at half maximum (FWHM) of 15 frames (3.75 mins). The results from the first and last 40 frames were discarded. The instantaneous frequencies were obtained from the spectrograms via the identification of the frequency with the maximum amplitude at each time point. Any points lying outside the micropipette were assigned 0 Hz frequency.

The pattern frequencies along the long axis (vertical direction) of the micropipette were obtained by calculating the mean of the values in the central region of the micropipette in the x-direction. This method was repeated for the pattern intensity values.

Chapter 4

Infrared Fluorescence Spectroscopy for Fluorophore Identification

> *"What will be the* A. victoria *and* C. elegans *of the future?*
> *Indeed, what will be the GFP of the future?"*
>
> — Martin Lee Chalfie
> GFP: Lighting Up Life

4.1 Abstract

Since the discovery of the green fluorescent protein from the bioluminescent jellyfish *Aequoera victoria*, fluorescent proteins have revolutionized the biological sciences. With this powerful tool, processes which were previously invisible, such as the internal protein machinery of the cell, have come to light. Today, a plethora of fluorescent proteins and various other fluorophores are at the disposal of scientists, and the discovery of new fluorescent markers with more desirable properties such as higher photostability, deeper penetration depth, and more specific binding is an active field of research. Unveiling the properties of these substances is crucial to their discovery and development. To this end, in the Fakhri Lab at MIT, we have built an infrared fluorescence spectrometer for the identification of such fluorophores and the char-

acterization of their photoproperties. This chapter outlines the spectroscopy setup, various calibration methods, and proposed improvements.

4.2 Introduction

4.2.1 Physics of fluorescence

A molecule occupying the ground state (lowest electronic state) can be excited, or elevated to higher electronic states, through the absorption energy in the form of a photon. This molecule will quickly lose energy in the form of heat through collisions with its surrounding molecules, and settle to the lowest vibrational level of its first excited state. From here, the molecule may relax to its ground state via the emission of a photon, in a process called fluorescence.

Due to non-radiative energy transfers in the relaxation process, the emitted photon always carries a lower energy, thus a longer wavelength, than that of the absorbed photon. The only exception is for the 0-0 transition, in which the molecule moves from the lowest energetic level in the ground state to the lowest level in the first excited state. In this case, the absorbed and emitted photon energies are equal. Due to this, the excitation spectrum of a molecule spans shorter wavelengths than its emission spectrum.

The details of the molecule's electronic structure determines the quantum efficiency – the likelihood of light absorption resulting in the emission of a photon – and gives rise to the characteristics of its excitation and emission spectra. In principle, the energy required to transition between each electronic state is discretized, which one could expect would lead to narrow bands of excitation and emission wavelengths. Yet, the wealth of available rotational and vibrational levels of most molecules results in their excitation and emission lines being so dense that they cannot be resolved. Thus they span an entire spectral region continuously. The range and shape of the excitation and emission spectra, and thus the structure of the molecule's electronic states, can be uncovered through fluorescence spectroscopy.

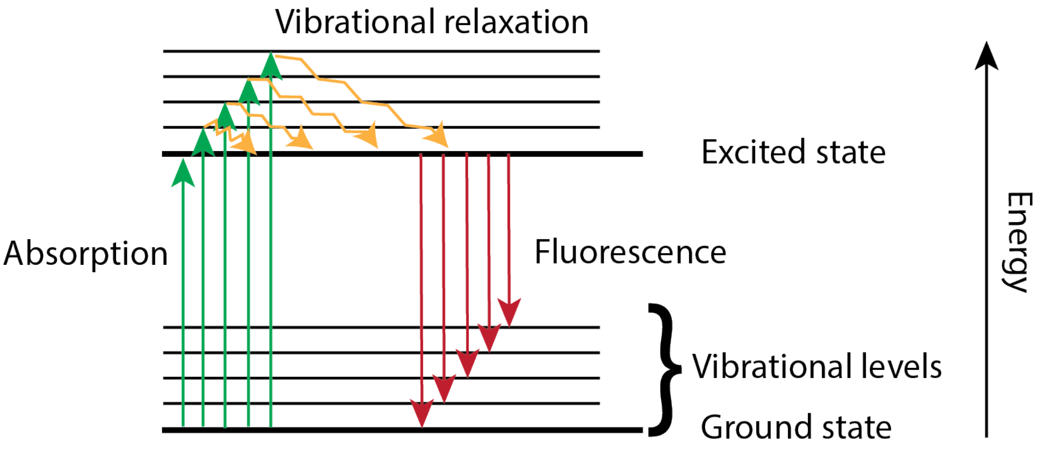

Figure 4-1: Jablonski diagram of an absorption and fluorescence process.

4.2.2 Principles of fluorescence spectroscopy

The aim of fluorescence spectroscopy is to identify the emission or the excitation spectrum of the sample of interest. Therefore, there are three components essential to a spectrometer: a source, a monochromator or a spectrograph, and a detector.

To excite the material, a light source with a selectable wavelength is needed. This can be accomplished either through a source with a specific output wavelength, such as a light-emitting diode or a laser, or with a broadband source, such as a xenon arc lamp, used in conjunction with a filter. In order to uncover the excitation spectrum, either a tunable source, such as a titanium-sapphire laser, or a set of filters that covers the spectral region of interest is needed.

After the sample is excited, the resulting emission is collected and filtered via a monochromator or a spectrograph. The former only allows for a narrow window of wavelengths through to be collected by the detector. The wavelength range can often be tuned mechanically. The latter disperses the light such that different wavelengths are mapped onto spatial points of the detector. A variety of monochromator and spectrograph configurations exist. The next section discusses the commonly used Czerny-Turner spectrograph set up.

After the emitted light is filtered or dispersed, it reaches the detector. Modern spectroscopy systems typically utilize one or two-dimensional semiconductor based array detectors. The choice in the semiconducting material depends on the spectral

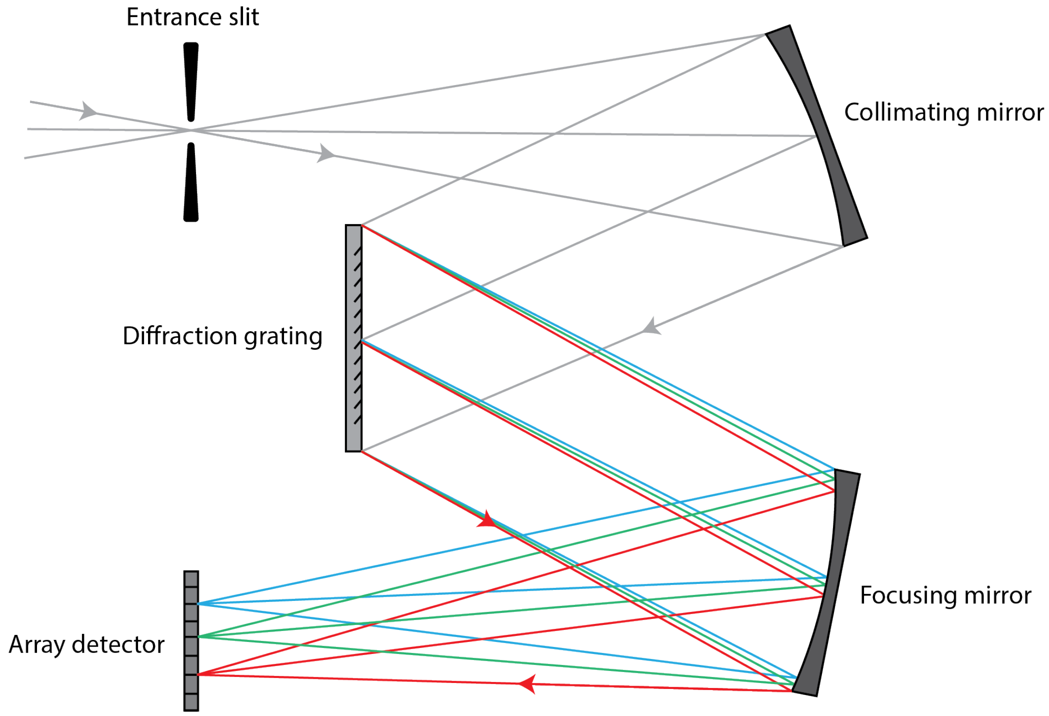

Figure 4-2: Schematic of a Czerny-Turner Spectrometer.

range of interest. For spectroscopic or imaging applications in the ultraviolet (UV) or visible range, silicon based detectors, such as charge coupling devices (CCD), electron multiplying CCDs (EMCCDs), or complementary metal-oxide-semiconductor (CMOS) devices, are preferred due to high acquisition speed and superior signal-to-noise performance. These detectors are effective for use starting in the UV, for wavelengths longer than 200nm, and extending into the NIR, up to 1000nm. Their quantum efficiency (QE) quickly plummets beyond this point.

For longer wavelengths, indium-gallium-arsenide (InGaAs) detectors are utilized. Though these detectors typically have higher inherent noise than that of silicon based arrays, standard InGaAs chips maintain high QE up to 1700nm, with extended wavelength InGaAs having the ability to go up to 2500nm.

4.2.3 Czerny-Turner spectrograph

A multitude of spectrograph configurations exist, with Czerny-Turner being the most common one. As depicted in Figure 4-2, in a Czerny-Turner spectrograph, incoming light enters through a slit and is collimated via a mirror before reaching the diffraction grating. The grating maps each wavelength to a unique angle, which gets mapped onto a specific location on the detector via a focusing mirror.

In order to attain the the maximum performance from the spectrograph, the collimating mirror must be completely filled by the incoming light, which can be ensured by matching the optical specifications such as its f-number. Depending on the wavelength range of interest, various optical coatings may be available, but protected silver coatings display superior reflectivity of nearly 98% for wavelengths from 500 nm to over 2μ m.

Arguably the most critical component of a spectrograph is the diffraction grating. To cover a wide range of wavelengths, these gratings may sit on mechanical turrets. Some of the factors that can affect grating efficiency are coating, angle of operation, and groove geometry (such as blaze value and whether it is ruled or holographic).

Once these conditions are optimized for the desired application, the relationship between the pixel location on the array detector and the wavelength it maps to must be determined. This can be accomplished by using a source with known, discrete, emission lines, such as a mercury lamp. Using the grating equation and combining it with the known locations of the emission peaks, the entire spectrum can be mapped out. During this process, care must be taken to ensure that only first order diffraction of the desired wavelengths will be imaged.

The grating equation can be expressed as

$$\sin(\alpha) + \sin(\beta) = kn\lambda$$

where α denotes the incoming beam angle incident on the grating, β the outgoing angle, k the diffraction order, n the grating groove density, and λ the wavelength of the beam. For a given incoming and outgoing beam angle incident on a specific grating,

$$k\lambda = constant,$$

so wavelengths that are integer multiples of one another get mapped onto the same location on the detector. For example, the 1st order diffraction of 1000nm light corresponds to the same location as the 2nd order diffraction of 500nm light. This can be avoided by minimizing stray light and placing a filter that blocks sample emission wavelengths outside of the desired range.

4.3 Infrared fluorescence spectrometer setup for uncovering the spectral properties of fluorophores

We have built a state-of-the-art spectroscopy system incorporating an Andor Czerny-Turner fluorescence spectrograph with a one-dimensional InGaAs detector. The spectroscopy set-up is optimized for coherent, visible spectrum excitation and is sensitive to infrared emission. Yet, it can be easily adapted to be used with shorter or longer wavelength excitation sources and can be expanded to incorporate a one or two dimensional detector sensitive to the visible spectrum.

4.3.1 Light source

The excitation source for the spectroscopy system is a 561 nm wavelength 50mW OBIS laser. The output power can be tuned through the OBIS computer application or a neutral density filter. The optical path is designed with the capability to integrate other lasers with different wavelength outputs. The choice of laser wavelength was made using the signal-to-noise ratio of the images attained under the illumination of various coherent light sources, attained from the custom built microscope in the Fakhri Lab.

4.3.2 Excitation path

The excitation arm consists of a laser line filter to ensure monochromaticity of the input light source, a beam expander (telescope), and a dichroic beam splitter. The lenses that make up the telescope contain A-type anti-reflective (AR) coating, which is optimum for the 350-700nm wavelength range (see Figure 4-3 for the reflectance

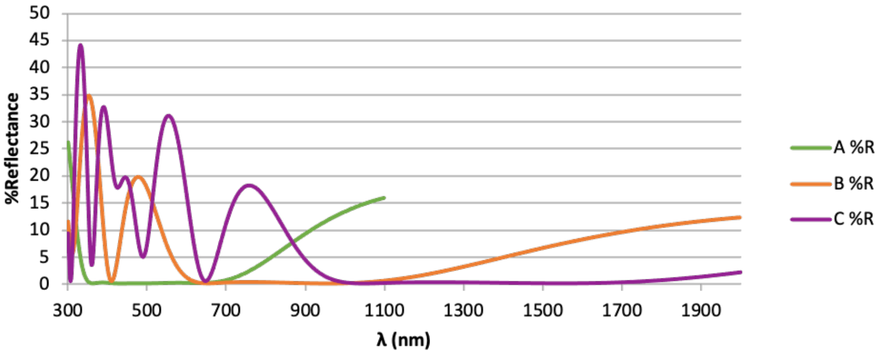

Figure 4-3: Reflectance curves of A, B, and C-type anti-reflective optical coatings, obtained from ThorLabs.

curve). The diameter of the resulting excitation beam is selected to fill the back focal lane of the objective.

Since the spectral properties of the fluorescent material is unknown, having the ability to observe a wide wavelength range, from around 700nm up to 1500nm, is ideal. Yet, most dichroic beamsplitters have narrower transmission windows, and are often designed for applications in the visible range, or less commonly, for far infrared wavelengths. Initially a notch beamsplitter that only rejects the laser line was used, but its performance was lacking in the NIR. Thus it was replaced with ThorLabs DMLP650, a long-pass filter with a 650nm cut-on and a steep edge transition. This component exhibits nearly 100% transmission from 650nm to 1650nm, but does not allow observations in the visible spectrum. The greatly improved performance of the dichroic beamsplitter in the NIR outweighs this drawback, since in its current configuration, the spectroscopy system is not optimized for use in the visible wavelengths: the spectrometer houses only an InGaAs array, which has low QE for visible wavelengths, and the optical components selected are not ideal for the visible range. Furthermore, in the future, this component can be replaced with a more suitable one, if a silicon-based detector is integrated and the optical components changed to those that are optimal for the visible range.

4.3.3 Objective and sample holder

An objective with a high numerical aperture (NA) is chosen in order to gather maximal fluorescence from the sample. To this end, a Nikon Apo Fluor 60X oil immersion objective is integrated into the set up. This objective has high efficiency in the NIR wavelengths and low chromatic aberration, which can broaden the fluorescence spectra at different wavelengths. If a larger field of view is desired, the Nikon Apo Fluor 20X air objective can also be used, but will suffer from lower NA.

The oocytes suspended in salt water or liquid purified samples are housed in glass bottom 96-well plates or quartz slides in order to minimize background fluorescence from the substrate. The sample holder rests on three linear manual stages for 2D lateral as well as vertical movement. The vertical motion of the sample is necessary as the objective is fixed.

4.3.4 Emission path

After the light emitted by the sample passes back through the objective and the dichroic beamsplitter, two silver coated mirrors are used to direct the beam into the entrance slit of the spectrograph at the correct height. The next component is a clean-up filter to remove the residual laser line, and a focusing lens that has a B-type AR coating, optimal for 650 - 1050nm wavelength range (see Figure 4-3 for the reflectance curve).The focusing lens is selected to match the f-number of the spectrograph for maximal performance.

Misalignment of the incoming beam translates as a tilt in the dispersed light that hits the InGaAs linear detector. Thus, it is crucial to ensure precise alignment of the beam to avoid errors in the detection of the spectrum. Unfortunately, the fluorescence is not visible and not bright enough to be observed through an IR scope. Thus, we first removed the filter and performed an initial alignment using the residual laser beam. For the subsequent fine alignment, we used the light from a Tungsten-Halogen lamp, which has a flat spectrum in the infrared region, and viewed the beam through an IR scope.

4.3.5 Andor Kymera 193i spectrograph

The Kymera 193i spectrograph has a Czerny-Turner style configuration, similar to the schematic depicted in Figure 4-2. Silver coated optics were selected for maximum reflectivity across the wavelengths of interest.

Housed on a mechanical turret, up to two gratings can be inserted at a time. The tilt, yaw, and pitch of the gratings can be adjusted manually. For maximum efficiency and optimal angle of operation, a 300 lines per millimeter (l/mm) ruled grating blazed at 1000nm and a 600 l/mm ruled grating blazed at 1000nm are selected. These gratings operate at optimum grating angles and boast over 50% efficiency for wavelengths between 800nm - 1400nm. Below and above this range the operating angle is still optimal, but the efficiency declines.

4.3.6 InGaAs photo diode array detector

The detector used in conjunction with the Andor Kymera 193i spectrograph is the Andor iDus 491 - 1.7μm InGaAs photo diode array (PDA). The PDA is thermo-electrically cooled down to -90°C in order to minimize dark current and maximize the signal-to-noise ratio. It is capable of detection from 600 nm up to 1.7μm wavelengths. For wavelengths between 950nm and 1.6 μm, the InGaAs PDA has a QE of above 80% with a peak QE of over 85%.

4.3.7 Andor Solis software

The spectrograph and InGaAs array are operated via the Andor Solis software. The software is equipped with the capability of communicating with the detector, such as cooling the PDA and capturing the pixel intensity, as well as operating the spectrograph, such as rotating the diffraction grating turret and moving the focusing mirror (see Figure 4-2) in order to auto-focus the spectral output onto the detector.

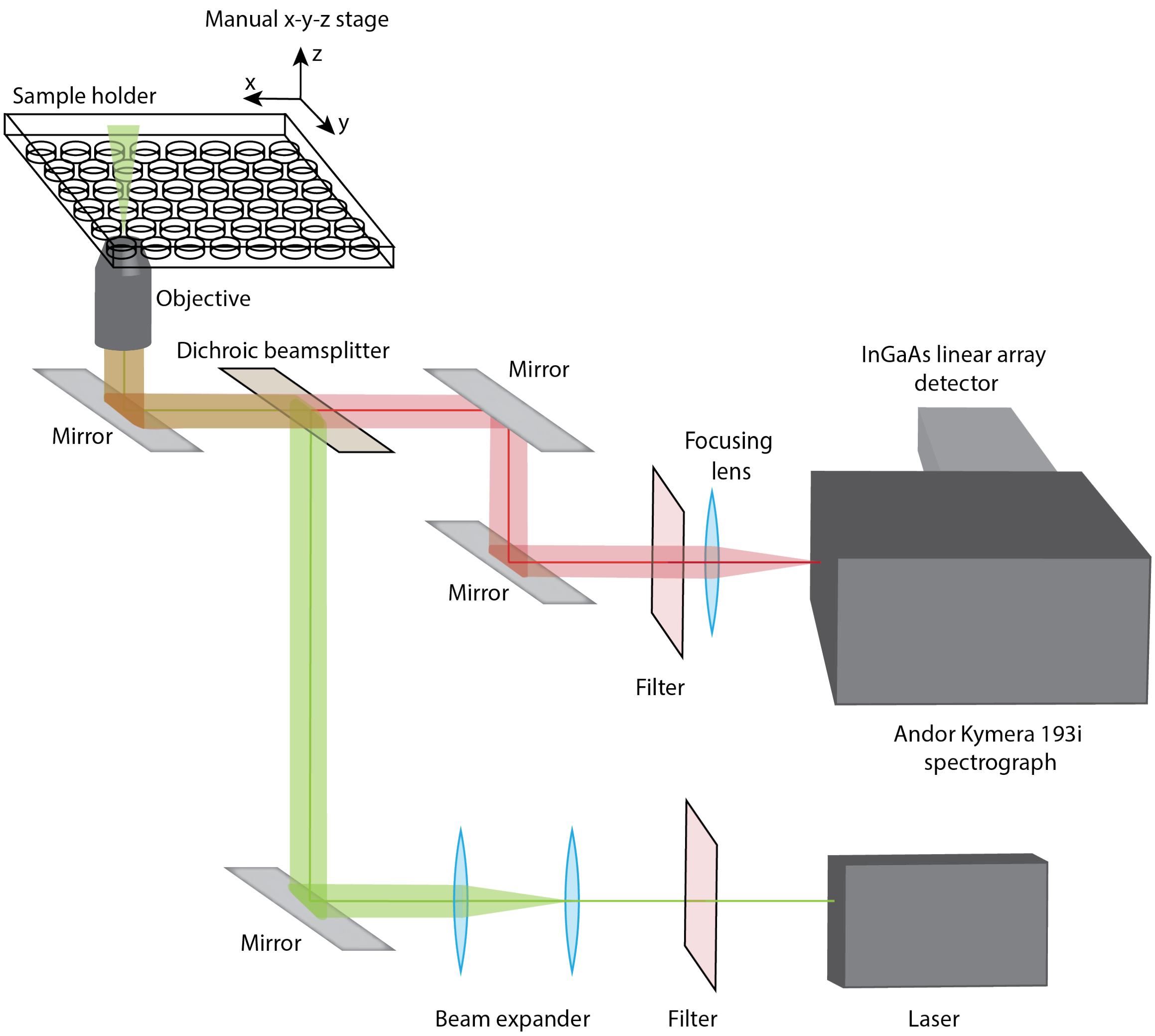

Figure 4-4: Schematic of the IR sensitive spectroscopy setup incorporating an Andor Kymera 193i spectrograph and Andor iDus 491 - 1.7μm InGaAs photo diode array. The excitation path consists of a 561nm coherent light source, a beam expander, and a dichroic beamsplitter with high transmission across the far-red and IR range. The objective is chosen with a high numerical aperture and low aberration. The emission path consists of mirrors that align the beam into the spectrograph slit, a filter to cut out residual laser and visible stray light, and a focusing lens selected to match the f-number of the spectrograh. The Czerny-Turner style spectrograph houses silver coated optics for maximum reflectivity across the wavelengths of interest, two gratings with maximal performance in the NIR, and an InGaAs array detector.

4.4 Calibration methods

Two types of calibrations are essential for attaining a reliable spectral output: wavelength calibration of the spectrograph and spectral responsivity of the spectroscopy system.

The former can be performed by using a source with multiple known, discrete, spectral emission lines. We performed this via the use of a mercury vapor arc lamp and a solution of single walled carbon nanotubes (SWCNTs) that were enhanced in a specific semiconducting lattice orientation with visible wavelength absorption and NIR range emission. This SWCNT solution was also used for focusing the sample.

The latter calibration requires the use of a source with a continuous spectral output in the rage of interest. For this, a tungsten-halogen lamp was used, as this source has emission across the entire far-red and IR range. This step is vitally important since different optical components exhibit spectrally varying responsivity to light. This necessitates the need to convert the acquired spectra to real intensity via the responsivity curve.

4.4.1 Mercury vapor arc lamp

Mercury lamps exhibit multiple emission peaks in the ultraviolet and visible region, ranging from 350nm to 600nm. Even though InGaAs detectors have low QE in this region, the Andor iDus 1.7μm is able to detect photons down to 400nm, and thus mercury lamps may be used for wavelength calibration.

120W mercury vapor short arc lamp (X-Cite 120Q) from Excelitas Technologies was used for spectral calibration of the Andor Kymera 193i spectrograph. After removing all optical components outside the spectrograph, the output of the lamp was directly coupled to the entrance slit of the spectrograph. The spectrum was taken and three peaks between 400nm and 600nm were identified. The locations of these peaks were matched to the mercury atomic spectrum peaks via the Andor Solis software.

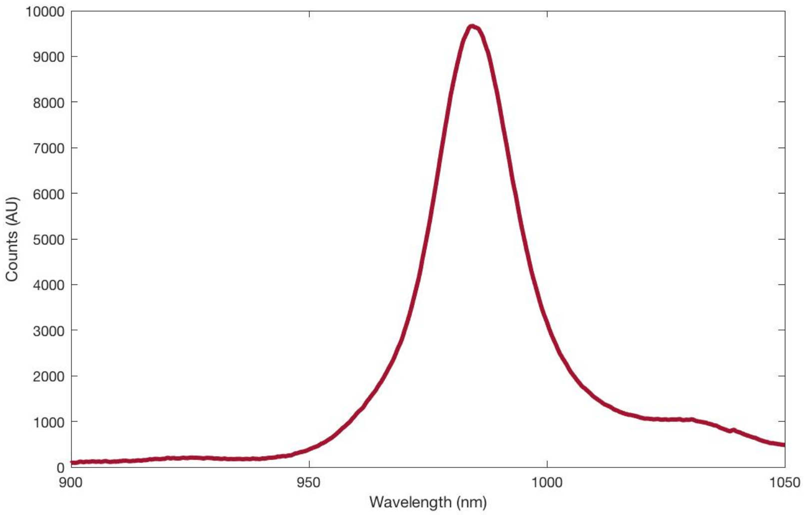

Figure 4-5: Fluorescence spectrum of a liquid sample of SWCNT solution enriched in (6,5) chirality, excited via a 561 nm laser, as captured by the Fakhri Lab spectrometer.

4.4.2 Single-walled carbon nanotubes

As discussed in Section 4.2.3, semiconducting SWCNTs exhibit excitonic fluorescence in the NIR and SWIR, with peak wavelengths dependent on their lattice orientation. We used a non-functionalized SWCNT solution enriched in the (6,5) chirality as a convenient tool for wavelength and sample focus calibration.

The (6,5)-SWCNTs have peak absorption at 565nm and peak emission at 988nm, making them excellent calibration tools for our set up as they are easily excited with the 561nm coherent light source, and their emission peak is close to the expected emission range of the sample of interest. Thus, the emission location of the (6,5) enriched nanotube solution was checked for possible misalignments or drifts in the spectroscopy system, and its fluorescence peak height was maximized before each experiment to ensure optimum focus.

4.4.3 Tungsten-Halogen lamp

To measure the responsivity curve of the spectrometer, a calibrated tungsten-halogen lamp from Ocean Optics (HL-3P-CAL) was used. The spectal output of the lamp is shown in Figure 4-6, with stars denoting the data points. The values in between the

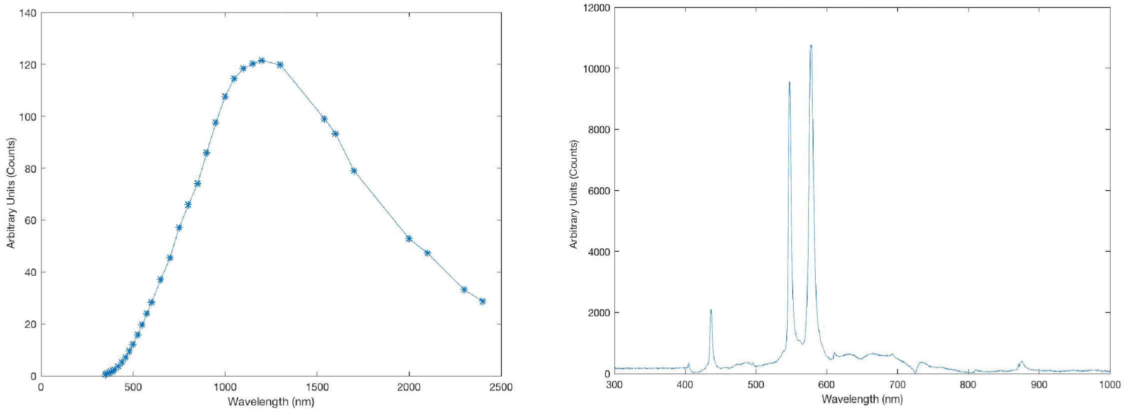

(a) HL-3P-CAL calibrated tungsten-halogen lamp spectral output, as provided by Ocean Optics.

(b) Exceltias Technologies X-Cite 120Q mercury vapor short arc lamp spectrum, as measured by the Fakhri Lab spectrometer

Figure 4-6: Spectra of calibration sources with continuous (a) and discrete (b) outputs.

points were determined via linear interpolation. This output was coupled to a multimode optical fiber. In order to capture the responsivity of the entire spectrometer, including the optical components outside of the spectrograph, such as the objective, dichroic beamsplitter, and focusing lens, the end of the optical fiber was placed at the focal point of the objective.

The responsivity curve $R(\lambda)$ is calculated by the following equation:

$$R(\lambda) = \frac{I_{meas}(\lambda) - I_{dark}(\lambda)}{I_{calib}(\lambda)},$$

where $I_{meas}(\lambda)$ denotes the measured intensity of the tungsten-halogen lamp, $I_{dark}(\lambda)$ is the intensity without a light source, and $I_{calib}(\lambda)$ is the intensity of the tungsten-halogen lamp acquired from Ocean Optics.

Therefore, the corrected spectrum of the sample, $I_{corr}(\lambda)$ is calculated by

$$I_{corr}(\lambda) = \frac{I_{meas}(\lambda) - I_{ref}(\lambda)}{R(\lambda)},$$

where $I_{meas}(\lambda)$ denotes the measured sample intensity and $I_{ref}(\lambda)$ is the measured intensity of the reference or blank.

4.5 Proposed improvements to the spectrometer

4.5.1 Motorized stage design

The samples of interest are housed in standard 96 well plates. This enables high-throughput spectroscopic analysis. Yet, due to the large lateral movement range that is needed to scan through the different samples, the current stage is unable to utilize the entire plate. Furthermore, the manual set up requires full time attention of an operator throughout the experimental process. Because the alignment of the wells and the objective is done by eye, slight misalignments can occur, leading to inconsistencies in data taking. During the alignment process there is also a risk of laser exposure.

In order to combat all of the mentioned shortcomings of the current stage set up, a motorized stage can be implemented. Such a motorized stage must be able to house a 96 well plate without significant sagging, and incorporate motorized linear translation stages with long range capabilities in the lateral (X-Y) as well as the vertical (Z) directions. This way, the entire experimental process can be automated. Such a motorized stage can be constructed in two ways, using the ThorLabs components outlined in Table 4.1.

Item	Description
MLJ150	Motorized high-load vertical translation stage
NRT150 (option 1)	150 mm linear translation stage, stepper motor
NRT100 (option 1)	100 mm linear translation stage, stepper motor
BSC202 (option 1)	Two-channel APT stepper motor controller
LTS150 (option 2)	150 mm linear translation stage with integrated controller, stepper motor
LTSP1 (option 2)	XY adapter plate for LTS150 or LTS300 stages
MP100-MLSH	Large insert holder, adjustment height: 148.1-208.5
MLS203P1	Multi-well plate adapter

Table 4.1: Components of proposed motorized stages

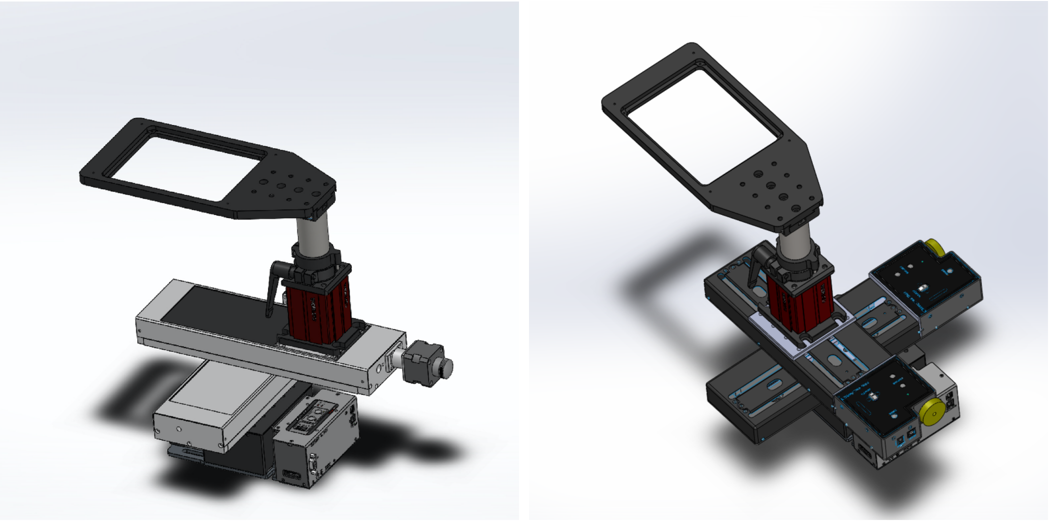

(a) Option 1: Proposed set-up utilizing ThorLabs NRT linear translation stages

(b) Option 2: Proposed set-up utilizing ThorLabs LTS linear translation stages

Figure 4-7: Schematics of two proposed motorized stage configurations

4.5.2 Additional excitation sources

Additional excitation sources can be integrated by simply implementing a flippable mirror before the beam expander in the excitation arm. Having a wider range of excitation wavelengths will not only allow for the spectroscopy set-up to be used for other fluorescent materials, but will also enable the absorption spectrum of the fluorescent granules to be identified. For the latter aim, instead of a specific wavelength, a source that has a wide range of spectral outputs is necessary. Through the use of an emission monochromator or a filter, the source wavelength can be tuned, and the excitation spectrum uncovered.

4.5.3 Separating the excitation and emission paths

The current spectroscopy setup contains a single objective that focuses the excitation beam onto the sample and collects the resulting fluorescence, capturing undesirable interactions with the sample holder substrate during this process. Since the sample fluorescence emanates in all directions, acquiring this radiation from an angle different from that of the excitation beam will not result in a decrease in photons. On the other hand, background emission from interactions with the substrate will be significantly lowered, increasing the signal to noise ratio.

4.5.4 Silicon based detector for increased spectral range

The Andor Kymera 193i spectrograph is equipped with two camera ports. Currently, only one is utilized with a one-dimensional InGaAs detector, but another detector sensitive to a different spectral region can be added to the second port in order to increase the range of detection. If a two-dimensional detector is used, this would enable imaging in the chosen spectral range in addition to spectroscopy.

Chapter 5

Concluding Remarks

"But then science is nothing but a series of questions
that lead to more questions."

— Terry Pratchett
The Long Earth

In this thesis, I experimentally investigated the relationship between biochemical patterning and shape deformations in single cellular systems using spatio-temporal RhoA activity in the cell membrane of *Patiria miniata* oocytes as a model system. Utilizing cortex embedded fluorescent granules as point probes, I showed that RhoA generates spatially and temporally patterned surface deformations that co-evolve with the biochemical patterns themselves.

In this system, cortical strain rate is directly (inversely) related to local active RhoA density, acting largely as a viscous material on the pattern length and timescales. The biochemical activity and strain rate fields are so intimately related that they manifest as if they were two sides of the same coin. Since the RhoA patterns are spiral in nature with interacting spiral core dynamics [60], they can also be represented as a phase field by performing the Hilbert transform of each spatial point in time. The locations of the spiral cores correspond to point defects in an otherwise smoothly varying field. The same analysis can be performed on the mechanical field. In fact, we have already observed that the phase defects in the strain rate field closely correspond to those in the Rho field (Figure 5-1).

It is also possible that by various mechanisms, such as membrane curvature, stress induced accumulation/depletion, or variations in the membrane-to-cytosole ratio, mechanical deformations could affect and guide the evolution of individual spiral core motion and core-core interactions, such as those observed in *Tan et al., 2020* [60]. For example, local contraction and expansion or principal strain rate components of the cell cortex, obtained using methods outlined in Chapter 2, could provide a spatially varying and temporally oscillating field on which the topological defects move (Figure 5-1). Such an analysis would not only inform mechanisms of coupling of biochemical patterns to active cellular deformations, but could also allow for precise and local control of spiral core dynamics, and biochemical patterns in general, from purely mechanical manipulations.

In the pursuit of understanding the bi-directional coupling between RhoA activity and the cellular cortex, we have been working to uncover the constitutive relationship between the chemical and mechanical fields of this biological system.[1] Understanding the nature and the strength of the link between these two fields can shed light on how biochemical patterns sense their changing mechanical environments and evolve with them.

Of course, cells do not only affect and control their own physical environment, but are also subject to extrinsic forces arising from the substrate they lie on or nearby cells and tissues. In Chapter 3 of this thesis, I showed how external dynamic geometrical deformations, induced via partial micropipette aspiration of sea star oocytes, could be used to manipulate RhoA pattern dynamics inside the mechanically perturbed region, in a consistent manner with a Rho-GEF gradient being set up inside the micropipette. Another variable to consider in the regulation of RhoA patterns is the distribution of membrane tension inside the micropipette. Numerous biochemicals have been shown to be tension dependent [42], and this property could be a factor

---

[1] This work is performed in collaboration with the Dunkel Group at MIT.

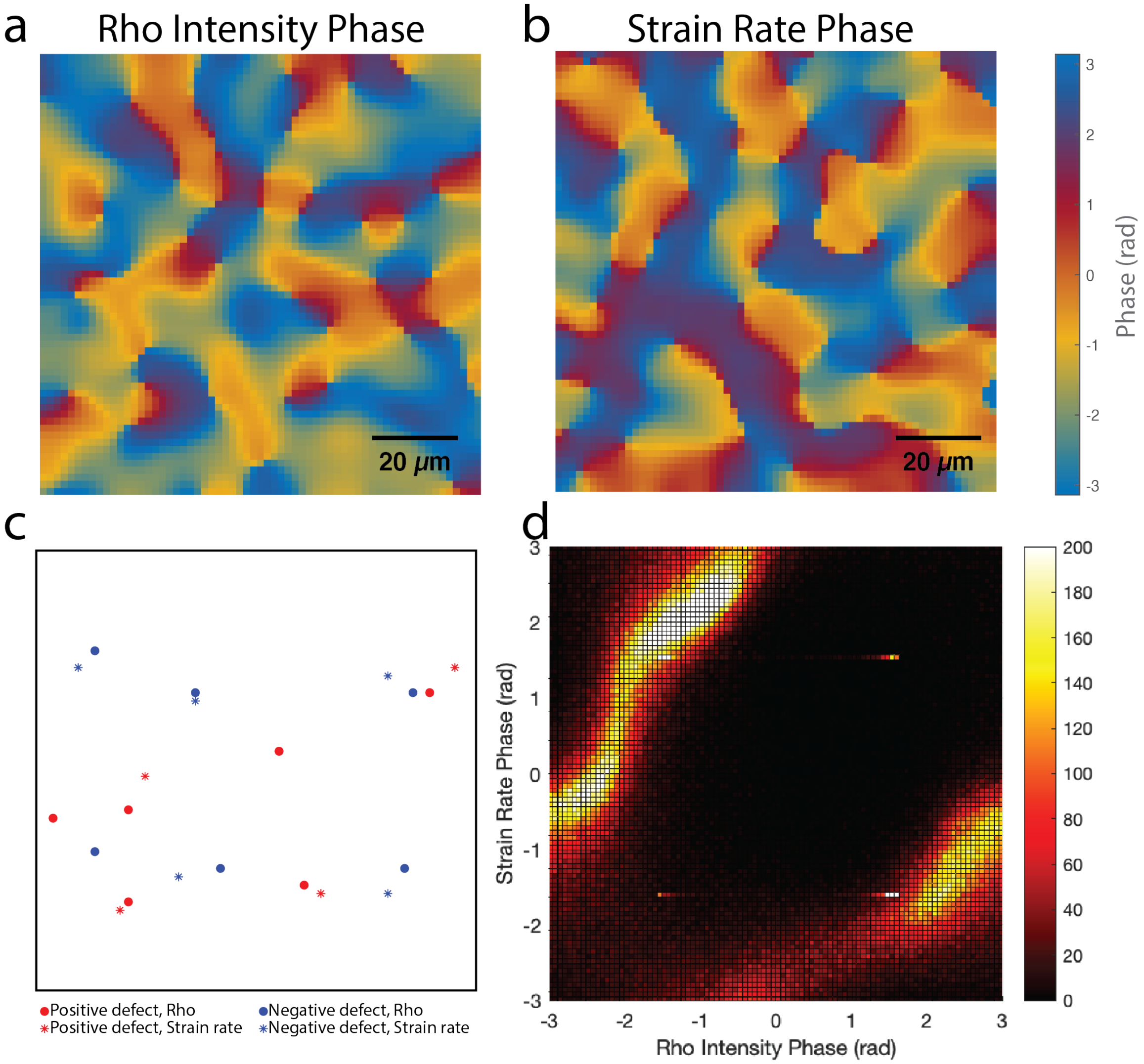

Figure 5-1: Phase representation of Rho intensity and strain rate and their corresponding topological defects. Panels **a** and **b** show the phase representation of Rho intensity and strain rate respectively, at a particular time point. Panel **c** shows the positive (red) and negative (blue) topological defects associated with the two fields at the same time point. Those obtained from the Rho phase field are denoted with a circle ($\circ$), and those from the strain rate phase field are denoted with a star ($*$). The topological defects associated with the two fields exhibit a high level of spatial correspondence, and through the interactions of the two fields, could drive their motion. Panel **d** shows the histogram of the two phase fields. Consistent with the results from Chapter 2, the anti-correlated fields exhibit as a robust phase offset of π in the phase field, with some finer structure underlying this correlation.

in determining the spatial distribution of GEF, and therefore also Rho activity on the membrane. Various membrane tension probes, such as FliptR [15], have been developed, and could be utilized for this purpose.

Furthermore, in this study, only geometries that evolved much more slowly when compared to the Rho pattern dynamics were considered, and the pressure applied to the oocyte stayed roughly constant. Inducing more dynamic geometries would elucidate how membrane associated biochemicals respond to extraneous mechanical perturbations and address questions such as:

- How do patterns evolve in highly non-stationary geometries?
- How, and on what timescales, do Rho activity patterns reach steady state after mechanical perturbations?
- Can Rho patterns be locally altered by temporally driving cytoskeleton-membrane attachment/detachment events? [11]
- Do spiral cores display preferred directionality in their motion and distribution? Do they exhibit anisotropic interaction dynamics, dependent on geometry?

In summary, the work presented in this thesis has outlined a quantitative framework for studying coupling between biochemical patterns and cellular deformations in dynamic geometries. Expanding this work to exploring a variety of mechanical perturbations such as those mentioned above will further our understanding of cellular functions that require Rho GTPase activity, such as the essential processes of cell division and migration. Extending the studies to other model systems will allow for fundamental features of mechanochemical coupling common to all cellular systems to be identified.

Bibliography

[1] Bruno Antonny. Mechanisms of membrane curvature sensing. *Annual Review of Biochemistry*, 80:101–123, 2011.

[2] Claudia Arbore, Laura Perego, Marios Sergides, and Marco Capitanio. Probing force in living cells with optical tweezers: from single-molecule mechanics to cell mechanotransduction.

[3] Angika Basant and Michael Glotzer. Spatiotemporal regulation of rhoa during cytokinesis. *Current Biology*, 28:R570–R580, 2018.

[4] Amy Bejsovec. Wingless/wnt signaling in drosophila: the pattern and the pathway. *Molecular Reproduction and Development*, 80:882–894, 2013.

[5] William M Bement, Marcin Leda, Alison M. Moe, Angela M. Kita, Matthew E. Larson, Adriana E. Goldiing, Courney Pfeuti, Kuan-Chung Su, Ann L. Miller, Andrew B. Goryachev, and George von Dassow. Activator-inhibitor coupling between rho signalling and actin assembly makes the cell cortex an excitable medium. *Nature Cell Biology*, 17:1471–1483, 2015.

[6] Johanna Bischof. *The molecular mechanism of surface contraction waves in the starfish oocyte.* PhD thesis, University of Heidelberg, Germany, 2016.

[7] Johanna Bischof, Christoph A. Brand, Kalman Somogyi, Imre Majer, Sarah Thome, Masashi Mori, Ulrich S. Shwarz, and Peter Lenart. A cdk1 gradient guides surface contraction waves in oocytes. *Nature Communications*, 8:849, 2017.

[8] Justin S. Bois, Frank Julicher, and Stephan W. Grill. Pattern formation in active fluids. *Physical Review Letters*, 106:028103, 2011.

[9] Mike Bonny, Elisabeth Fischer-Friedrich, Martin Loose, Petra Schwille, and Karsten Kruse. Membrane binding of mine allows for a comprehensive description of min-protein pattern formation. *PLOS Computational Biology*, 9:e1003347, 2005.

[10] James Briscoe, Peter A. Lawrence, and Vincent Jean-Paul. *Generation and Interpretation of Morphogen Gradients.* Coldsprings Harbor Press, 2010.

[11] Jan Brugues, Benoit Maugis, Jaume Casademunt, Pierre Nassoy, Francois Amblard, and Pierre Sens. Dynamical organization of the cytoskeletal cortex probed by micropipette aspiration. *PNAS*, 107(35):15415–15420, 2010.

[12] A.C. Callan-Jones and F. Julicher. Hydrodynamics of active permeating gels. *New Journal of Physics*, 13:093027, 2011.

[13] Gary PT Choi and L Mahadevan. Planar morphometrics using teichmüller maps. *Proceedings of the Royal Society A*, 474:20170905, 2018.

[14] Pui Tung Choi, Ka Chun Lam, and Lok Ming Lui. Flash: Fast landmark aligned spherical harmonic parameterization for genus-0 closed brain surfaces. *SIAM Journal on Imaging Sciences*, 8(1):67–94, 2015.

[15] Adai Colom, Emmanuel Derivery, Saeideh Soleimanpour, Caterina Tomba, Marta Dal Molin, Naomi Sakai, Marcos Gonzalez-Gaitan, Stefan Matile, and Aurelien Roux. A fluorescent membrane tension probe. *Nature Chemistry*, 10:1118–1125, 2018.

[16] Danielle R Cook, Patricia A Solski, Scott J Bultman, Gunther Kauselmann, Michael Schoor, Ralf Kuehn, Lori S Friedman, Dale O Cowley, Terry Van Dyke, Jen Jen Yeh, Leisa Johnson, and Channing J Der. The ect2 rho guanine nucleotide exchange factor is essential for early mouse development and normal cell cytokinesis and migration. *Genes Cancer*, 2(10):932–942, 2011.

[17] JM Crawford, N Harden, T Leung, and DP Kiehardt. Cellularization in drosophila melanogaster is disrupted by the inhibition of rho activity and the activation of cdc42 function. *Developmental Biology*, 204:151–64, 1998.

[18] DN Drechsel, AA Hyman, A Hall, and M Glotzer. A requirement for rho and cdc42 during cytokinesis in *Xenopus* embryos. *Current Biology*, 7:12–23, 1997.

[19] AJ Engler, S Sen, HL Sweeney, and DE Discher. Matrix elasticity directs stem cell lineage specification. *Cell*, 126:677–689, 2006.

[20] Douglas J Fishkind and Yu-li Wang. Orientation and three-dimensional organization of actin filaments in dividing cultured cells. *Journal of Cell Biology*, 123(4):837–848, 1993.

[21] Tina Freisinger, Ben Klu, Jared Johnson, Nikola Mu, Garwin Pichler, Gisela Beck, Michael Costanzo, Charles Boone, Richard A Cerione, Erwin Frey, and Roland Wedlich-Soldner. Establishment of a robust single axis of cell polarity by coupling multiple positive feedback loops. *Nature Communications*, 4(1807), 2013.

[22] HNC Frohnhöfer and C Nüsslein-Volhard. Organization of the anterior pattern in the *Drosophila* embryo by the maternal gene *bicoid*. *Nature*, 324:120–125, 1986.

[23] Y Funakoshi, M Minami, and T Tabata. mtv shapes the activity gradient of the dpp morphogen through regulation of thickveins. *Development*, 128:67–74, 2001.

[24] Scott F. Gilbert. *Developmental Biology*. Palgrave Macmillan, 2020.

[25] Ryan S. Gray, Isabelle Roszko, and Lilianna Solnica-Krezel. Planar cell polarity: coordinatin morphogenetic cell behaviors with embryonic polarity. *Developmental Cell*, 21:120–133, 2011.

[26] Kristina Haase and Andrew E Pelling. Investigating cell mechanics with atomic force microscopy. *Interface*, 12:20140970, 2015.

[27] J Halatek, F Brauns, and E Frey. Self-organization principles of intracellular pattern formation. *Philosophical Transactions B*, 373(20170107), 2018.

[28] M. S. Hamaguchi and Y. Hiramoto. Protoplasmic movement during polar-body formation in starfish oocytes. *Experimental Cell Research*, 112:55–62, 1978.

[29] Koki Hara, Peter Tydeman, and Marc Kirschner. A cytoplasmic clock with the same period as the division cycle in *Xenopus* eggs. *Proceedings of the National Academy of Sciences, USA*, 77(1):462–466, 1980.

[30] Carl-Philipp Heisenberg and Yohanns Bellaiche. Forces in tissue morphogenesis and patterning. *Cell*, 153:948–962, 2013.

[31] John H Henson, Casey E Ditzler, Aphnie Germain, Patrick M Irwin, Eric T Vogt, hucheng Yang, Xufeng Wu, and Charles B Shuster. The ultrastructural organization of actin and myosin ii filaments in the contractile ring: new support for an old model of cytokinesis. *Molecular Biology of the Cell*, 28(5):613–623, 2017.

[32] Robert M Hochmuth. Micropipette aspiration of living cells. *Journal of Biomechanics*, 33:15–22, 2000.

[33] Kerwyn Casey Huang, Yigal Meir, and Ned S Wingreen. Dynamic structures in Escherichia coli : Spontaneous formation of MinE rings and MinD polar zones. *Proceedings of the National Academy of Sciences*, 100(22):12724–12728, 2003.

[34] Philip W. Ingham. Localized *hedgehog* activity controls spatial limits of *wingless* transcription in the *Drosophila* embryo. *Nature*, 366:560–562, 1993.

[35] Philip W. Ingham, Yoshiro Nakano, and Claudia Seger. Mechanisms and functions of hedgehog signalling across the metazoa. *Nature Reviews Genetics*, 12:393–406, 2011.

[36] Shawn N. Jordan and Julie C. Canman. Rho gtpases in animal cell cytokinesis: An occupation by the one percent. *Cytoskeleton*, 69:919–930, 2012.

[37] Dominic Kamps, Johannes Koch, Victor O. Juma, Eduard Campillo-Funollet, Melanie Graessl, Soumya Banerjee, Tomas Mazel, Xi Chen, Yao-Wen Wu, Stephanie Portet, Anotida Madzvamuse, Perihan Nalbant, and Leif Dehmelt. Optogenetic tuning reveals rho amplification-dependent dynamics of a cell contraction signal network.

[38] Eugene A Katrukha, Marina Mikhaylova, Hugo X vanBrakel, Paul M van Bergen en Henegouwen, Aanna Akhmanova, Casper C Hoogenraad, and Lukas C Kapitein. Probing cytoskeletal modulation of passive and active intracellular dynamics using nanobody-functionalized quantum dots. *Nature Communications*, 8:14772, 2017.

[39] Manabu Kuno Kojima. Cyclic changes of the cortex and the cytoplasm of the fertilized and the activated sea urchin egg. *Embryologia*, 7:81–94, 1962.

[40] Shih-Lei Lai, Ching-Nung Chang, Pei-Jen Wang, and Shyh-Jye Lee. Rho mediates cytokinesis and epiboly via rock in zebrafish. *Molecular Reproductive Development*, 71:186–96, 2005.

[41] Maria Leptin. *twist* and *snail* as positive and negative regulators during *Drosophila* mesoderm development. *Genes and Development*, 5:1568–1576, 1991.

[42] Tianzhi Luo, Krithika Mohan, Pablo A Iglesias, and Douglas N Robinson. Molecular mechanisms of cellular mechanosensing. *Nature Materials*, 12:1064–1071, 2013.

[43] Silvia Maretto, Michelangelo Cordenonsi, Sirio Dupont, Paola Braghetta, Vania Broccoli, A. Bassim Hassan, Dino Volpin, Giorgio M. Bressan, and Stefano Piccolo. Mapping wnt/β-catening signaling during mouse development and in colorectal tumors. *PNAS*, 100:3299–3304, 2003.

[44] Adam C. Martin and B Goldstein. Apical constriction: Themes and variations on a cellular mechanism driving morphogenesis. *Development*, 141:1987–1998, 2014.

[45] D.Q. Matus, C. R. Magie, K. Pang, M.Q. Martindale, and G.H. Thomsen. The hedgehog gene family of the cnidarian, *Nematostella vectensis*, and implications for understanding metazoan hedgehog pathway evolution. *Developmental Biology*, 313:501–518, 2008.

[46] Hans Meinhardt and Piet A.J. de Boer. Pattern formation in *Escherichia coli*: A model for the pole-to-pole oscillations of min proteins and the localization of the division site. *Developmental Cell*, 21:120–133, 2011.

[47] Melissa Moser and Gerard Campbell. Generating and interpreting the brinker gradient in the drosophila wing. *Developmental Biology*, 286:647–58, 2005.

[48] Celeste M. Nelson. Geometric control of tissue morphogenesis. *Biochimia et Biophysica Acta*, 1793:903–910, 2009.

[49] Masatoshi Nishikawa, Sundar Ram Naganathan, Frank Julicher, and Stephan W. Grill. Controlling contractile instabilities in the actomyosin cortex. *eLife*, 2017.

[50] Alisa Piekny, Michael Werner, and Michael Glotzer. Cytokinesis: welcome to the rho zone. *Trends in Cell Biology*, 15:651–658, 2005.

[51] Josh Quaas and Christopher Wylie. Surface contraction waves in the xenopus egg are required for the localization of the germ plasm and are dependent upon maternal stores of the kinesin-like protein xklp1. *Developmental Biology*, 243:272–280, 2002.

[52] David M. Raskin and Piet A.J. de Boer. Rapid pole-to-pole oscillation of a protein required for directing division to the middle of *Escherichia coli*. *PNAS*, 96:4971–4976, 1999.

[53] Julia Riedl, Alvaro H Crevenna, Kai Kessenbrock, Jerry Haochen Yu, Dorothee Neukirchen, Michal Bista, Frank Bradke, Dieter Jenne, Tad A Holak, Zena Werb, Michael Sixt, and Roland Wedlich-Soldner. Lifeact: a versatile marker to visualize f-actin. *Nature Methods*, 5:605, 2008.

[54] Mara D. Rueda-Contreras, Jose R. Romero-Airas, Jose L. Aragon, and Rafael A. Barrio. Curvature driven spatial patterns in growing 3d domains: A mechanochemical model for phyllotaxis. *PLOS One*, 13(8):e0201746, 2018.

[55] SA Ruiz and CS Chen. Emergence of patterned stem cell differentiation within multicellular structures. *Stem cells*, Dayton, Ohio, 2008.

[56] Arnab Saha, Masatoshi Nishikawa, Martin Behrndt, Carl-Philipp Heisenberg, Frank Julicher, and Stephan W. Grill. Determining physical properties of the cell cortex. *Biophysical Journal*, 110:1421–1429, 2016.

[57] Guillaume Salbreux, Guillaume Charras, and Ewa Paluch. Actin cortex mechanics and cellular morphogenesis. *Trends in Cell Biology*, 22:536–545, 2012.

[58] Soon-Tuck Sit and Ed Manser. Rho gtpases and their role in organizing the actin cytoskeleton. *Journal of Cell Science*, 124(5):679–683, 2011.

[59] Tetsuya Tabata and Yuki Takei. Morphogens, their identification and regulation. *Development*, 131:703–712, 2004.

[60] Tzer Han Tan, Jinghui Liu, Pearson W. Miller, Melis Tekant, Jorn Dunkel, and Nikta Fakhri. Topological turbulence in the membrane of a living cell. *Nature Physics*, 16:657–662, 2020.

[61] Tzer Han Tan, Maya Malik-Garbi, Enas Abu-Shah, Junang Li, Abhinav Sharma, Fred C MacKintosh, Kinneret Keren, Christoph F Schmidt, and Nikta Fakhri. Self-organized stress patterns drive state transitions in actin cortices. *Science Advances*, 4:2847, 2018.

[62] Manuel Thery and Michel Bornens. Cell shape and cell division. *Current Opinions in Cell Biology*, 18:648–657, 2006.

[63] Cheryll Tickle and Matthew Towers. Sonic hedgehog signaling in limb development. *Frontiers in Cell and Developmental Biology*, 5(14), 2017.

[64] Alan Turing. The chemical basis of morphogenesis. *Philosophical Transaction of the Royal Society of London B*, 237(641):37–72, 1952.

[65] Roland Wedlich-Soldner, Steve Altschuler, Lani Wu, and Rong Li. Spontaneous Cell Polarization Through Actomyosin-Based Delivery of the Cdc42 GTPase. *Science*, 299(5610):1231 – 1235, feb 2003.

[66] Lukas Wettmann and Karsten Kruse. The min-protein oscillations in *Escherichia coli*: an example of self-organized cellular protein patterns. *Philosophical Transaction of the Royal Society B*, 373:20170111, 2018.

[67] Manon C. Wigbers, Tzer Han Tan, Fridtjof Brauns, Jinghui Liu, S. Zachary Swartz, Erwin Frey, and Nikta Fakhri. A hierarchy of protein patterns robustly decodes cell shape information. *Nature Physics*, 2021.

[68] Zhanghan Wu, Maohan Su, Cheesan Tong, Min Wu, and Jian Liu. Membrane shape-mediated wave propagation of cortical protein dynamics. *Nature Communications*, 9:136, 2018.